PROCEEDINGS

OF 11TH INTERNATIONAL CONFERENCE ON COMMUNICATIONS, ELECTROMAGNETICS AND MEDICAL APPLICATIONS (CEMA'16)

Organized by:

FACULTY OF TELECOMMUNICATIONS
TECHNICAL UNIVERSITY OF SOFIA, BULGARIA

NATIONAL TECHNICAL UNIVERSITY OF ATHENS, GREECE,
SCHOOL OF ELECTRICAL AND COMPUTER ENGINEERING

NATIONAL TECHNICAL UNIVERSITY OF ATHENS, GREECE

SCHOOL OF ELECTRICAL AND COMPUTER ENGINEERING

Athens, Greece
13th – 15th October, 2016

KING 2001, Sofia

Edited by Prof. Dr. Eng. **Dimiter Tz. Dimitrov**

ISSN: 1314-2100

Printed in Bulgaria
KING 2001, Sofia

P. Frangos

D. Dimitrov

K. Dimitrov

Dear Colleagues,

It is our privilege to thank all of you for your contributions submitted at 11th regular International Conference on 'Communication, Electromagnetic and Medical Applications' CEMA'16. This is a conference which should help future collaboration in the area of engineering, especially in the area of communication technologies and medical applications. This is an important scientific event not only in Balkan region, but in Europe, also. The International Conference on Communication, Electromagnetism and Medical Applications CEMA'16 is dedicated to all essential aspects of the development of global information and communication technologies, and their impact in medicine, as well. The objective of Conference is to bring together lecturers, researchers and practitioners from different countries, working on the field of communication, electromagnetism, medical applications and computer simulation of electromagnetic field, in order to exchange information and bring new contribution to this important field of engineering design and application in medicine. The Conference will bring you the latest ideas and development of the tools for the above mentioned scientific areas directly from their inventors. The objective of the Conference is also to bring together the academic community, researchers and practitioners working in the field of Communication, Electromagnetic and Medical Applications, not only from all over Europe, but also from America and Asia, in order to exchange information and present new scientific and technical contributions.

Many well known scientists took part in conference preparation as members of International Scientific Committee or/and as reviewers of submitted papers. We would like to thank all of them for their efforts, for their suggestions and advices.

We are extremely grateful to the company INTRACOM Bulgaria for its regular support of our conference.

On behalf of the International Scientific Committee, we would like to wish you successful presentations of your papers, successful discussions and new collaborations for your future scientific investigations.

Engineering and medicine should provide high level of living for all people.

P. Frangos
Conference Chairman

D. Dimitrov
Conference Vice Chairman

K. Dimitrov
Conference Vice Chairman

INTERNATIONAL SCIENTIFIC COMMITTEE

Chairman:

P. FRANGOS, National Technical University of Athens, Greece

Vice Chairmen:

D. TZ. DIMITROV, Technical University of Sofia, Bulgaria
K. L. DIMITROV, Technical University of Sofia, Bulgaria

Members:

N. AMPILOVA,	University of Perersburg, Russia
D. ANDRIUKAITIS,	Kaunas University of Technology, Lithuania
T. AOYAGI,	Tokyo Institute of Technology, Japan
A. BEKJARSKY,	Technical University of Sofia, Bulgaria
R. BRUZGIENE,	Kaunas University of Technology, Lithuania
M. DONTSCHEWA,	University of Applied Sciences, Dorbirn, Austria
N. ESCUDEIRO,	Inst. Sup. de Engenharia do Porto, Portugal
E. GAGO-RIBAS,	University of Oviedo, Spain
S. Ver HOEYE,	University of Oviedo, Spain
M. HOFMANN,	University of Ulm, Germany
I. ILIEV,	Technical University of Sofia, Bulgaria
L. JORDANOVA,	Technical University of Sofia, Bulgaria
G. S. KLIROS,	Hellenic Air-Force Academy, Greece
R. KRIVICKAS,	Kaunas University of Technology, Lithuania
V. KUKENSKA,	Technical University of Gabrovo, Bulgaria
G. MALLET,	University "Sophia Antipolis", Nice, France
G. MATSOPOULOS,	National Technical University of Athens, Greece
M. MARTINS,	Instituto Superior Técnico, Lisboa, Portugal
M. GONZALEZ-MORALES,	University of Valladolid, Spain
L. NARBUTAITE,	Kaunas University of Technology, Lithuania
K. NIKITA,	National Technical University of Athens, Greece
M. NIKOLOVA,	High Naval School, Varna, Bulgaria
J. PETROVSKA,	Medical University of Sofia, Bulgaria
F. PRATO,	University of Western Ontario, Canada
H. ROTH,	University of Siegen, Germany
S. SAUTBEKOV,	Euroasian University, Astana, Kazakhstan
A. SAVOV,	Medical University of Sofia, Bulgaria
S. SAVOV,	Technical University of Varna, Bulgaria
H-P. SCHADE,	Technical University of Ilmenau, Germany
J. SEBASTIAN,	Universidad Complutense de Madrid, Spain
L. SONG,	Technical University of Harbin, China
A. USHEVA,	University of Boston, USA

REVIEWERS

BALZANO, Q.	University of Maryland, USA
BEHARI, J.	Jawaharlal Nehru University ,New Delhi, India
BERG, H.	Technical University of Jena, Germany
BOEMO, E.	Technical University of Madrid, Spain
DIMITROV, D.	Technical University of Sofia, Bulgaria
DONTSCHEWA, M.	University of Applied Sciences, Dorbirn, Austria
GOUSSETIS, G.	Heriot - Watt University, United Kingdom
MALLET, G.	University "Sophia Antipolis", Nice, France
MARINKEV, V.	Medical University of Plovdiv, Bulgaria
PETROVSKA, J.	Medical University of Sofia, Bulgaria
PRATO, F.	University of Western Ontario, Canada
ROTH, H.	University of Siegen, Germany
SAVOV, A.	Medical University of Sofia, Bulgaria
SCHADE, H-P.	Technical University of Ilmenau, Germany
SONG, L.	Technical University of Harbin, China
USHEVA, A.	University of Boston, USA

REGISTRATION

October, 13th, 09h 30min – 16h

The conference registration desk will be at:

University Administration Building
Ceremonies Room (zero level of building)
National Technical University of Athens, Greece

CONFERENCE PROGRAM

13th October

Opening ceremony

10h – 10h 30min
University Administration Building
Ceremonies Room (zero level of building)
National Technical University of Athens, Greece

SCIENTIFIC PROGRAM

13th October

FIRST SESSION

10h 30min – 12h
University Administration Building
Ceremonies Room (zero level of building)
National Technical University of Athens, Greece

Chairman: Prof. P. Frangos, National Technical University of Athens, Greece

1. **DESIGN AND ANALYSIS OF GRAPHENE-BASED MULTILAYER STRUCTURES FOR ELECTROMAGNETIC COMPATIBILITY (EMC) APPLICATIONS,**
   G. S. Kliros, M. I. Skontranis, Hellenic Air-Force Academy, Department of Aeronautical Sciences

2. **ENERRGY EFFICIENT BROADBAND SATELLITE COMMUNICATION SYSTEMS DESIGN IN FREQUENCIES ABOVE 10GHZ,**
   Nikolaos K. Lyras, Charilaos I. Kourogiorgas, Athanasios D. Panagopoulos, National Technical University of Athens, Greece

3. **QOS-DRIVEN ALLOCATION SCHEMES IN SPECTRUM LEASING COGNITIVE RADIO NETWORKS**,
   Anargyros J. Roumeliotis, Athanasios D. Panagopoulos, National Technical University of Athens, Greece

4. **SIMULTANTING CHROMATIC DISPERSION IN OPTICAL FIBER CHANNELS USING SPLIT STEP FOURIER METHOD,**
   Mihail Mihailov, Georgi Iliev, Technical University of Sofia, Bulgaria

5. **ON SOME QUESTIONS CONCERNING TO THE MULTIFRACTAL SPECTRAL CALCULATION,**
   N. Ampilova, V.D.Sergeev, I. Soloviev, St. Petersburg State University, St. Petersburg, Russia

6. **HUMAN EXPOSURE STUDY FOR SOME SCENARIOS,**
   Tamar Nozadze, Revaz Zaridze, Veriko Jeladze, Vasil Tabatadze, Ivan Petoev, Mikheil Prishvin, Tbilisi State University, Tbilisi, Georgia

Lunch
12h – 13h

SECOND SESSION
13h – 14h 30min
University Administration Building
Ceremonies Room (zero level of building)
National Technical University of Athens, Greece

Chairman: Prof. G. Kliros, Hellenic Air-Force Academy, Athens, Greece

1. **CHARACTERIZATION OF ROUGH FRACTAL SURFACES FROM BACK-SCATTERED RADAR DATA,**
   A. Kotopoulis, G. Pouraimis, A. Malamou, E. Kallitsis, P. Frangos, National Technical University of Athens, Greece

2. **THE RADIATION PROBLEM FROM A VERTICAL SHORT DIPOLE ANTENNA ABOVE FLAT AND LOSSY GROUND: VALIDATION OF NOVEL SPECTRAL DOMAIN ANALYTIC SOLUTION IN THE HIGH FREQUENCY REGIME AND COMPARISON TO EMPIRICAL TERRAIN PROPAGATION MODELS,**
   G. Bebrov, S. Bourgiotis, A. Chrysostomou, S. Sautbekov, P. Frangos, National Technical University of Athens, Greece, Eurasian National University, Astana, Kazakshtan

3. **IN SILICO SIMULATION OF GLIOBLASTOMA GROWTH AND INVASION INTO THE HUMAN BRAIN INCLUDING AN EXPLICIT MODELLING OF THE ADIABATIC BOUNDARY CONDUCTION IMPOSED BY THE SKULL**,
   Stavroula G. Giatili and Georgios S. Stamatakos, Institute of Communication and Computer Systems, In Silico Oncology and In Silico Medicine Group, National Technical University of Athens, Greece.

4. **LASER-DIODE BASED PHOTOACOUSTIC SIGNAL EXCITATION FOR BIOMEDICAL APPLICATIONS,**
   Viktor Stoev, Mityo Mitev, Ivo Iliev, Technical University of Sofia, Bulgaria

5. **KIDNEY SEGMENATTION IN ULT RASOUND IMAGES VIA ACTIVE CONTOURS**, V. M. Georgieva, S. G. Vassilev, *Technical University of Sofia, Bulgaria*

6. **SIMPLIFIED METHOD OF LED LAMP USEFUL LIFE PROTECTION,**
   Vytautas Dumbrava, Irmantas Kupčiūnas, Darijus Pagodinas, Vytautas Knyva, Gedeiminas Činčikas, Kaunas University of Technology, Kaunas, Lithuania

Break
14h 30min – 15h

THIRD SESSION

15h – 16h 30min

University Administration Building
Ceremonies Room (zero level of building)
National Technical University of Athens, Greece

Chairman: Prof. N. Ampilova, St. Petersburg State University, St. Petersburg, Russia

1. **DIFFERENT SIGNALS' PARAMETERS INFLUENCE ON IMAGE QUALITY ASSESSMENT**,
   Tomas Adomkus, Lina Narbutaitė, Rasa Brūzgienė, Kaunas University of Technology, Kaunas, Lithuania
2. **CAVITY RESONATOR FOR STUDING THERMAL AND NON-TERMAL EFFECTS OF RADIO WAVES ON BIOLOGICAL TISSUES**,
   Hristo Gochev, Boncho Bonev, Peter Petkov, Technical University of Sofia, Bulgaria
3. **OPTIMIZATION OF THE MECHANICAL UNITS IN MEDICAL CENTRIFUGE, (CHAIR OF BARANY) WITH VARIABLE MECHANICAL TIME CONSTANT,**
   T. Kachamachkov, D. Bakardzhiev, H. Bakardzhiev, V. Manoev,Technical University of Sofia, Bulgaria
4. **OPTIMIZATION OF THE PARAMETERS OF THE MECHANICAL GEAR IN MEDICAL CENTRIFUGE (CHAIR OF BARANY),** T. Kachamachkov, D. Bakardzhiev, H. Bakardzhiev, V. Manoev,*Technical University of Sofia, Bulgaria*
5. **ANALYSIS OF IMPULSE RESPONSE MEASUREMENT SIGNALS USED IN ROOM ACOUSTIC,**
   S. Pleshkova-Bekiarska, S. Philipov, Technical University of Sofia, Bulgaria
6. **METHOD FOR SECURITY ENHANCEMENT OF AUDIO INFORMATION IN COMMUNICATION MULTIMEDIA SYSTEMS AND NETWORKS APPLYING ENCRYPTION ALGORITHM WITH PUBLIC KEY**,
   S. Pleshkova-Bekiarska, D. Kinanev, Technical University of Sofia, Bulgaria

CLOSING CONFERENCE SESSIONS

16h 30min– 17h

University Administration Building
Ceremonies Room (zero level of building)
National Technical University of Athens, Greece

SOCIAL PROGRAM

Social Program SCHEDULE

- **Conference Dinner** in the heart of old city , October 13, in the evening. More information regarding Conference dinner will be provided during the first day of the Conference (October 13).

- Furthermore, a **tour** to the famous **'Acropolis of Athens'**, and its corresponding **'New Acropolis Museum',** will take place on October 14th.

- In addition, more touristic information about Athens and Greece can be provided by the Conference Organizers.

CONTACT US:

http://oldweb.tu-sofia.bg/eng_new/fktt/cema16

Submission of contributions

Prof. Dr. Dimiter Dimitrov

Faculty of Telecommunication
Technical University of Sofia
8, Kliment Ohridsky str.
1756 Sofia, Bulgaria
Phone:++359 2 9652278
Fax: ++359 2 9652278
E-mail: dcd@tu-sofia.bg

Cultural programme and hotel reservation

Prof. P. Frangos

National Technical University of Athens
School of Electrical and Computer Engineering
9, Iroon Polytechniou Str. ,
157 73 Zografou, Athens, Greece
Phone : 00 30 210 772 3694
Fax : 00 30 210 772 2281
E-mail : pfrangos@central.ntua.gr

TABLE OF CONTENTS

DESIGN AND ANALYSIS OF GRAPHENE-BASED MULTILAYER STRUCTURES FOR ELECTROMAGNETIC COMPATIBILITY (EMC) APPLICATIONS

G. S. Kliros and M. I. Skontranis

Hellenic Air-Force Academy, Department of Aeronautical Sciences Division of Electronics,
Electric Power & Telecommunications
Dekeleia Air-Force Base, Attica GR-1010, Greece

georgios.kliros@hafa.haf.gr; gskliros@ieee.org

Abstract

We calculate the electromagnetic absorption in a thin dielectric/graphene multilayer structure on a quartz substrate and investigate its performance as absorber for electromagnetic compatibility (EMC) applications up to 250 GHz, employing a modified transfer matrix method (TMM). Our results indicate that, high broadband absorbance greater than 80% can be achieved for both TE and TM-wave polarizations of the impinging plane wave when the number of stacked layers is increased up to 5-layers with spacer thickness equal to a quarter wavelength. The absorbance magnitude can be strongly modulated by changing the Fermi level of the graphene sheets via dc-voltages. The sensitivity of the absorbing structure to oblique incidence for both TE and TM-wave polarizations are studied. Moreover, by increasing the permittivity of the dielectric spacers, both the absorption magnitude and bandwidth are reduced.

1. INTRODUCTION

The increasing density of radiation emitters in the environment has made the electromagnetic compatibility (EMC) an important issue in avionics, nanoelectronics and medical electronic equipment design. Thus, there is a real demand for high performance, thin and flexible structures as electromagnetic shields. Graphene offers a potential unique material for designing such structures especially because of its high electrical conductivity that can be controlled electrically via a gate voltage that tunes the Fermi energy of the material. Recently, graphene based multilayer structures have been proposed for efficient absorption of electromagnetic radiation in the GHz and low THz range. Wu et al. [1] have proposed a multilayer absorber with 28% bandwidth at 140 GHz which is based on graphene/quartz stacks backed by a metal ground plate. Batrakov et al. [2] have demonstrated that there is an optimum number of graphene/polymer layers for maximum absorption of millimeter waves. It has been also demonstrated that localized or extended defects in the graphene sheet have no effect on the optimum absorbance [3].

In this work, we study theoretically a dielectric/graphene multilayer structure deposited over a quartz substrate, avoiding the use of a metal ground plate as shown in Figure 1. Such a structure is of particular relevance for EMC applications [4]. A transfer matrix method (TMM) is employed in order to investigate the performance of the structure as absorber in a broadband frequency range up to 250 GHz.

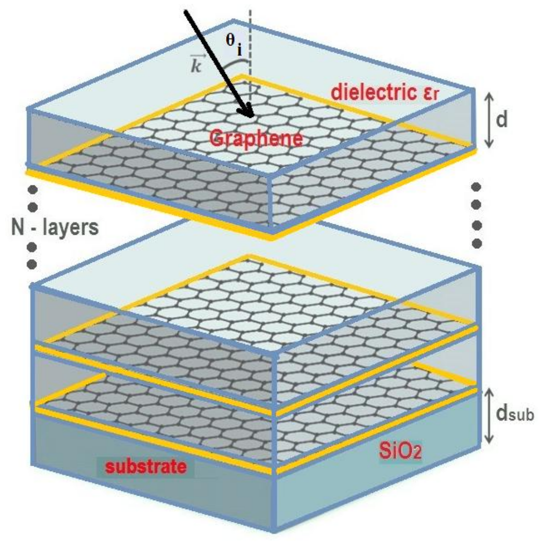

Figure 1. Schematic of N-layer graphene/dielectric multilayer structure backed by a quartz substrate and illuminated by a plane wave at oblique incidence.

2. DESIGN AND MODELING

2.1. Absorber Configuration

The basic configuration of the multilayer absorber under study is illustrated in Figure 1. It consists of N dielectric/graphene units deposited on a SiO_2 substrate of relative permittivity $\varepsilon_{r,sub}$ = 3.7 and thickness d_{sub}=0.5 mm. The dielectric spacers are flexible polymers with permittivity ε_r=2.6 and thickness d. Following the well-known configuration of the Jaumann absorber [5], the dielectric thickness d has been set equal to a quarter effective wavelength d=λ/(4 $\sqrt{\varepsilon_r}$). The graphene layers can be assumed electronically decoupled from each other due to the significant thickness of the dielectric spacers. The frequency-dependent conductivity of graphene is controlled by applying dc biasing voltages between the graphene layers. In contrast to common absorbers, the absorber proposed in this work does not involves a metallic backing plate which can be an advantage for some EMC applications.

2.2. Transfer Matrix Method (TMM)

The absorbance of the structure can be simulated by a variety of methods. The technique used in this work is the TMM for oblique incidence of a plane wave impinging on a planar multilayer structure composed of M layers with complex refractive indices $\tilde{n}_j$ and (M+1) interfaces [6] as shown in Fig. 2.

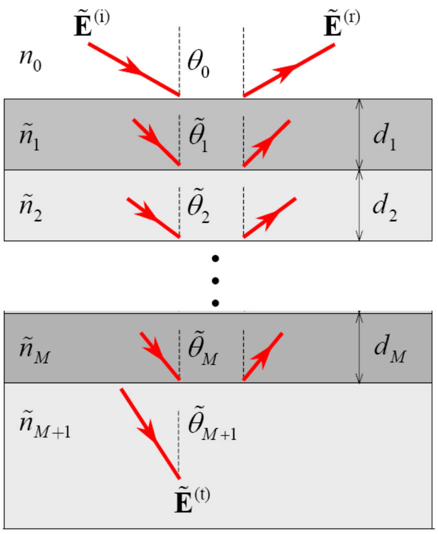

Figure 2. Propagation in a multilayer structure of M layers with complex refractive indices $\tilde{n}_j$ and (M+1) interfaces.

The total transfer matrix T of the system can be obtained by means of the transmission matrices D_{ij} across different interfaces i and j and the propagation matrices P_j through layer j.

$$T=\begin{bmatrix} T_{11} & T_{12} \\ T_{21} & T_{22} \end{bmatrix} = \left(\prod_{j=1}^{M} D_{(j-1)j} P_j \right) D_{M(M+1)} \qquad (1)$$

where

$$D_{ij}=\frac{1}{t_{ij}}\begin{bmatrix} 1 & r_{ij} \\ r_{ij} & 1 \end{bmatrix},\; P_j=\begin{bmatrix} e^{-i\delta_j} & 0 \\ 0 & e^{i\delta_j} \end{bmatrix} \qquad (2)$$

with t_{ij} and r_{ij} are the complex transmission and reflection Fresnel coefficients, $\delta_j=(2\pi/\lambda)\tilde{n}_j d_j \cos\tilde{\theta}_j$ is the phase shift acquired by the wave passing through the layer j and $\tilde{\theta}_j$ is the complex propagation angles that follow the Snell's law. The reflection and transmission coefficients are then r=T_{21}/ T_{11} and t=1/T_{11} respectively. The absorption of the multilayer structure is a function of angular frequency ω and can be calculated as

$$A(\omega)=1-|t(\omega)|^2\,\tilde{n}_{M+1}/\tilde{n}_0-|r(\omega)|^2 \qquad (3)$$

As a result, maximum absorption can be achieved by minimizing both transmission and reflection.

2.3. Graphene Permittivity Model

Under the assumption that the electronic band structure of a graphene layer is not affected by neighbouring graphene layers, the complex relative permittivity of graphene ε_g is given by

$$\varepsilon_g=1-j\frac{\sigma_g}{\omega\varepsilon_0 t_g} \qquad (4)$$

where σ_g is its surface conductivity and t_g=0.35 nm, its thickness. The isotropic surface conductivity σ_g of graphene can be written as a sum of the intraband and inter-band terms resulting from Kubo's formula [7].

$$\sigma_g(\omega)=\sigma_{intra}(\omega)+\sigma_{inter}(\omega) \qquad (5)$$

with

$$\sigma_{g,intra}=\frac{je^2}{\pi\hbar^2(\omega-j2G)}\int_0^\infty \varepsilon\left(\frac{\partial f_d(\varepsilon)}{\partial\varepsilon}-\frac{\partial f_d(-\varepsilon)}{\partial\varepsilon}\right)d\varepsilon$$

$$\sigma_{g,inter}=-\frac{je^2(\omega-j2G)}{\pi\hbar^2}\int_0^\infty \frac{f_d(-\varepsilon)-f_d(\varepsilon)}{(\omega-j2G)^2-4(\varepsilon/\hbar)^2}d\varepsilon$$

where $f_d(\varepsilon)$ is the Fermi-Dirac distribution and G is the scattering rate given by $G=\hbar e u_f^2/\mu E_f$ where u_f=10^6 m/sec is the Fermi velocity in graphene and μ=2x10^4 cm^2/(Vs) is the electron mobility at room temperature T=300 K.

3. RESULTS AND DISCUSSION

The absorption of the multilayer structure as function of the number of layers N has been simulated for both TE and TM-wave polarizations for a frequency range up to 250 GHz. High broadband absorbance is observed for both wave polarizations of impinging wave when the number of layers N is increased up to 5-layers. As shown in Figure 3, assuming a Fermi energy E_f =0.15 eV, the TE-wave absorption decreases as the angle of incidence increases, whereas the TM-polarized absorption has the opposite trend. However, the absorption is greater than 50% for a wide angle range up to 60° for both polarizations.

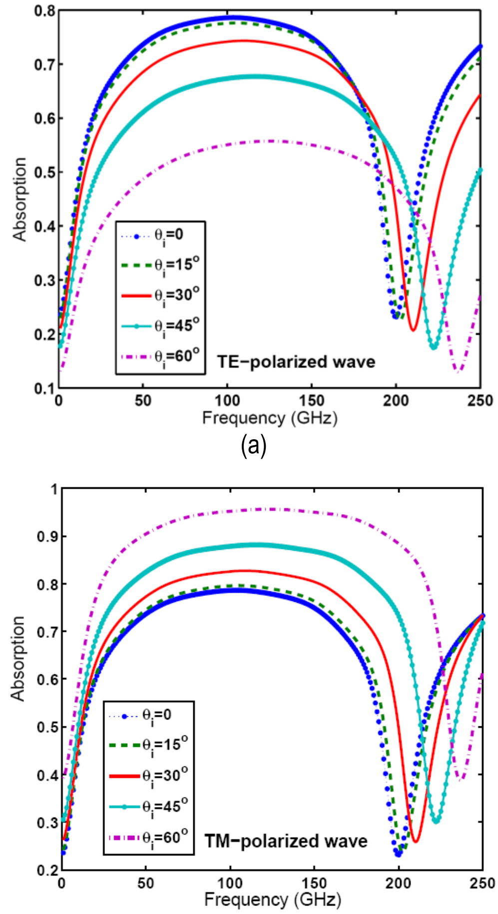

(a)

(b)

Figure 3. Absorption of 5-layer structure illuminated by (a) TE and (b) TM polarized wave at oblique incidence. The Fermi energy is set equal to 0.15 eV.

Figure 4 displays the sensitivity of absorption to the Fermi level changes. As is shown, strong modulation of the absorption, in all frequency range, can be achieved by increasing the Fermi energy. Moreover, as revealed by Fig.5, increasing the permittivity of the dielectric spacer, both the absorption magnitude and bandwidth are reduced.

To get insight into the dependence of absorption on the number of layers N, an example for TM-waves is given in Fig. 6. As shown, an almost perfect absorbance is obtained for N=5, at angle ~72° ('Brewster's angle') due to a minimum in the reflectance. However, such 'Brewster's angle' doesn't exists for TE-polarized waves.

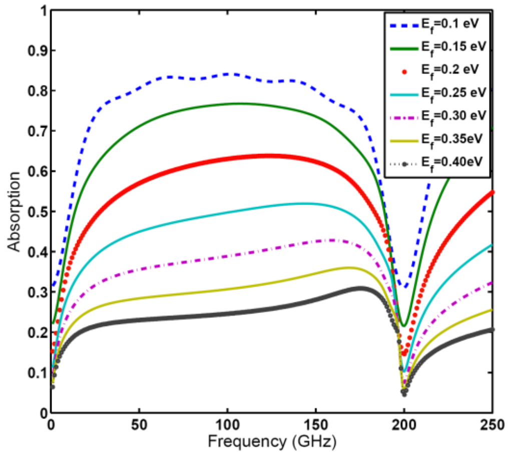

Figure 4. Absorption of 5-layer graphene/dielectric structure illuminated by a plane wave at normal incidence.

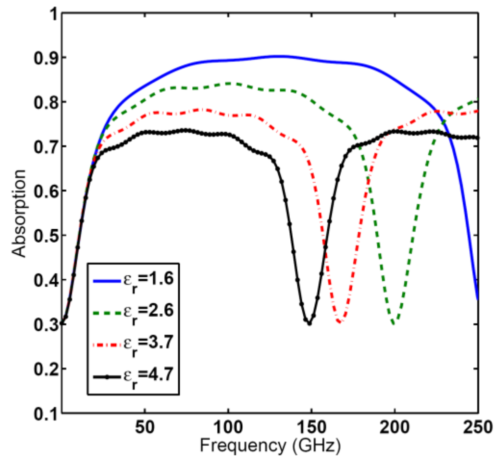

Figure 5. Absorption of 5-layer grapheme dielectric structure excited by a plane wave at normal incidence. The Fermi energy is set equal to 0.15 eV.

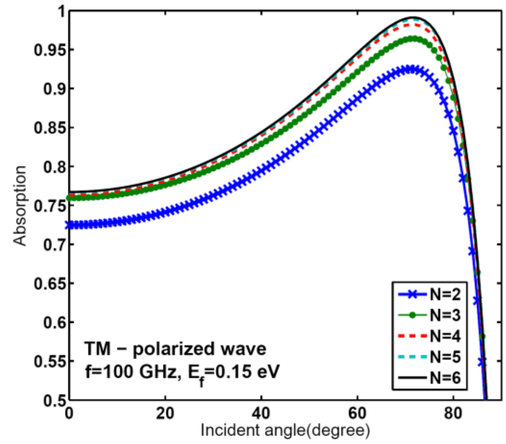

(a)

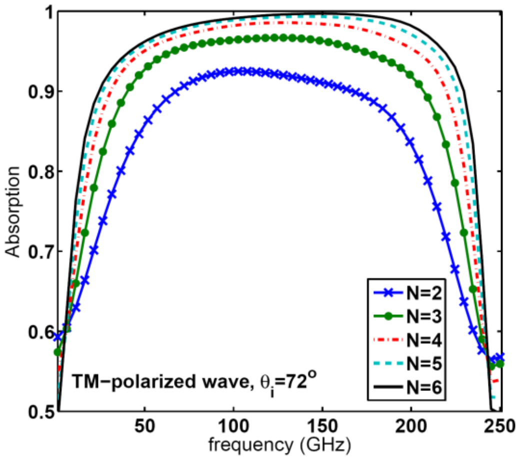

(b)

Figure 6. Absorption as function of (a) angle of incidence and (b) frequency when the structure is illuminated by TM-polarized waves for different number N of layers.

4. CONCLUSION

We have designed and simulated a broadband absorber composed of graphene sheets spaced by dielectric layers with thickness equal to a quarter wavelength at the central frequency.

Broadband and wide-angle high absorbance can be achieved for both polarizations when the number of stacked layers is increased up to 5-layers. The total thickness of the structure does not exceed 3 mm. The absorbance is strongly modulated by changing the Fermi energy of the graphene via a dc-voltage. We also found out that, increasing the spacer's relative permittivity, both absorption magnitude and bandwidth are reduced.

Interestingly, when the structure is illuminated by a TM-polarized wave, an almost perfect absorbance is obtained at angle of incidence around θ=72°.

References

[1] B. Wu *et al.,* "Experimental demonstration of a transparent graphene millimetre wave absorber with 28% fractional bandwidth at 140 GHz," Sci. Rep., vol. 4, 2014, p.4130.

[2] K. Batrakov *et al.*, "Flexible transparent graphene/polymer multilayers for efficient electromagnetic field absorption," Sci. Rep., vol. 4, 2014, p.7191.

[3] M. Lobet *et al.*, "Robust electromagnetic absorption by graphene heterostructures," Nanotechnology, vol. 26, 2015, p. 285702.

[4] A. G. D'Aloia *et al.*, "Optimal THz Shielding Electromagnetic absorbing properties of graphene/polymer composite shields," Carbon, vol. 73, 2014, pp. 175–184.

[5] L. Ke *et al.*, "Analysis and design of multilayer Jaumann absorbers", IEEE Int. Conf. ICMTCE, 2011, pp. 81-85.

[6] M. C. Troparevsky *et al.*, "Transfer-matrix formalism for the calculation of optical response in multilayer systems", Optics Express, vol.18, 2010, pp. 24715-24721.

[7] G. Hanson, "Dyadic Green's functions for anisotropic non-local model of biased graphene," IEEE Trans. Ant. Propag., vol. 56, no. 3, 2008, pp. 747–757

ENERGY EFFICIENT BROADBAND SATELLITE COMMUNICATION SYSTEMS DESIGN AT FREQUENCIES ABOVE 10 GHZ

Nikolaos K. Lyras, Charilaos I. Kourogiorgas, Athanasios D. Panagopoulos

School of Electrical and Computer Engineering
Iroon Polyrechniou 9, Zografou-Athens GR-15780, Greece

Emails: lyrasnikos@central.ntua.gr, harkour@mail.ntua.gr, thpanag@ece.ntua.gr

Abstract

Tropospheric attenuation is the dominant fading mechanism for modern broadband satellite communication systems operating at high frequency bands (above 10GHz). A very significant aspect of the effective design of such systems is the minimization of the consumed energy leading to Green Satellite Communications. In this contribution we discuss how Fade Mitigation Techniques (FMTs) can be used both to counteract the tropospheric attenuation and to minimize the consumed power, satisfying the required Quality of Service (QoS). 3year rainfall rate experimental data, used for the generation of channel dynamics are derived from two raingauges placed at Athens. FMTs design is based on the aforementioned statistics. Furthermore we examine a simulated pico-scale diversity scheme and we present statistics of the dynamic diversity gain for various satellite link characteristics.

1. INTRODUCTION

In modern satellite communication systems, the reliable design is constrained by the radio propagation effects, the interference and the noise that are inherently present in all radio systems [1], [2]. New and rate demanding broadband satellite application have been evolved and have led to the employment of higher frequency bands. The current satellite communications use GEO satellites for fixed satellite services and usually employ Ku (12/14GHz) and Ka (20/30GHz) bands. These frequency bands are used either for direct-to-user (DTU) applications, for broadcasting satellite applications, or for feeder links and satellite backhaul networks. Next-generation low Earth orbit (LEO) satellite systems will also operate at higher frequencies, i.e., Ka-band due to high available bandwidth and the congestion of conventional frequency bands, such as X-band and Ku-band. These frequency bands for NGEO satellites may be used either for Earth-observation links or telecommunication links. However, there are numerous activities mostly from European Space Agency for the exploitation of Q/V (33-50GHz) and W (75-110GHz) bands. Q/V band is proposed either for feeder links or for direct-to-user applications, while W band is studied for feeder links and backhauling applications. Satellite communication systems in these high frequency bands are severely affected by atmospheric phenomena and especially rain. A very significant aspect of the design of broadband satellite systems is the compensation of atmospheric phenomena minimizing at the same time the power consumption leading to "Green Satellite Communications".

The fade margin namely the system gain that ensures the specified Quality of Service (QoS) of the satellite link must be much greater in order to compensate the transmission and propagation impairments for satellite communications operating at frequencies much more 10GHz. The larger fade margins are not feasible of technical and economic reasons. The cost of the ground station would increase dramatically and significantly also increase the power consumption.

In order to satisfy the QoS requirements and with a view to exploit higher millimetre wave frequencies, a small fraction of time is significant for system design. Due to the fact that total attenuation induced into the system can take high values for this small fraction of time, the application of a high fixed power margin to deal with total attenuation (especially rain attenuation) does not give the optimum and efficient engineering solution as this extra power will remain unexploited for the greatest time percentage of the year. Consequently, Fade Mitigation Techniques (FMTs) are proposed in order to protect the system from atmospheric attenuation and to operate at smaller fade margins (higher energy efficiency). The FMTs used are categorized into the following three major classifications: i) Power Control Techniques, ii) Link adaptation techniques (Adaptive Coding and Modulation-ACM and Data Rate Reduction) and iii) Diversity techniques (Site, orbital, time and frequency).

In this contribution, we present how to design energy efficient FMTs. Then in Section III rainfall data for 3 years as measured by two tipping buckets placed at the National Technical University of Athens, NTUA Zografou campus (37.98°N, 23.79°E) with separation distance 387m are used for the generation of channel dynamics. More specifically the data are transformed into rainfall rate time series and then used as inputs in the synthetic storm technique (SST) [3] and they transformed into rain attenuation time series. In this paper the results for two hypothetical links at Ka (20GHz) and Q (40 GHz) bands located in Athens (GR) are exhibited.

Furthermore, we investigate the dynamic properties in pico-scale site diversity, for different frequencies and elevation angles and we present statistics of the dynamic diversity gain.

2. ENERGY EFFICIENT FMTS

Satellite channel dynamics are of prominent importance for the efficient design of high frequency satellite links. In this section the exploitation of channel dynamics and the dynamic fade margin for advanced FMTs are used with a view to achieving green satellite communication systems will be pinpointed. Satellite channel dynamics is the considered the value of the induced tropospheric attenuation.

Power Control Techniques: In a power control system the transmitted power is defined according to the current state of propagation impairments and especially the rain attenuation value. For example, while the attenuation induced by rain increases above a certain threshold (margin) then the transmitted power will also increase to compensate the rain attenuation impairments. In Figure 1 a snapshot of rain attenuation with various threshold values are presented. Therefore, in order to design energy efficient systems and to minimize the outage probability, these power thresholds must be accurately selected for the high frequency links. Moreover for the time that rain attenuation is above the various power thresholds the channel dynamics are real crucial. These statistics among others, give information in order to define the time needed to use a certain power to compensate rain attenuation or the time needed to change to a higher or lower transmitted power in order to keep the system available.

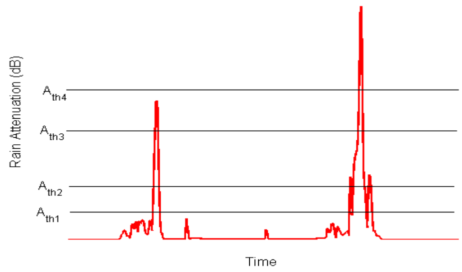

Figure 1. Rain attenuation events

Link adaptation techniques: The design of these techniques is very similar with the one is followed for the power control systems. The optimum rain attenuation thresholds for changing the various ACM and DRR schemes must be accurately defined. Moreover, channel dynamics must be exploited so as the time that the satellite link will remain in each ACM and DRR scheme and the time required to move from one scheme to the other is estimated. Consequently the maximization of the spectral efficiency and the minimization of the outage is achieved which turns on the reduction of consumed power.

Diversity techniques: First of all there is the time diversity technique which can be applied for delay tolerant services. In these technique data are transmitted when the fading is not strong. Therefor channel dynamics are needed to define among others the retransmit time, i.e. the time interval between the first try to transmit the data where there was high rain attenuation until the time that the data will finally transmitted, the attenuation threshold etc. The optimum estimation of such metrics can be proved really important for the energy efficiency.

Secondly, site diversity technique even in small distances can be applied. In this scheme more than one ground stations used to compensate the rain attenuation. The signal is received via different stations where it is likely each station faces different impairments. Channel dynamics are used for the diversity system so as the dynamic diversity gain is accurately estimated. As bigger as the diversity gain is so less power will be consumed.

Moreover, frequency diversity can be used. During the normal conditions high frequencies will be used while lower frequencies are preferred when rain attenuation exceeds certain thresholds.

Furthermore Orbital diversity is used to compensate the induced rain attenuation in accordance with the reduction of consumed power. Different satellites with different elevation angles are used for the same station. For the effective and reliable design of these systems channel dynamics must be computed so as the diversity gain is estimated.

3. NUMERICAL RESULTS

In this section the numerical results for hypothetical links at 20 GHz and 40 GHz are presented. The data used are derived from two rainfall rate measuring devices.

These devices are placed inside NTUA Zografou campus with 387 m separation distance. The resolution of rain gauges (tipping buckets) is 0.2 mm per tip. From rain gauge the rain fall amount per tip is measured and according to the methodology presented in [3] the rainfall rate series in mm/h with integration time of 1 min are calculated. Then Synthetic Storm Technique is used for the estimation of attenuation time series. This method takes into account the elevation angle of the link the frequency and the storm speed among others. Regarding the coefficients of specific rain attenuation and the rain height we have used the ITU-R P.838-3 and ITU-R P. 839-4 respectively. The average storm speed is assumed 14.25 m/s as derived from meteorological data in Athens, Greece. The availability of the rainfall rate data in both rain gauges is 100%.

In the following figures the Complementary Cumulative Distribution Function (CCDF) of rain attenuation, derived from the simulated rain attenuation time series from the first device at the operating frequencies are presented. The height of ground station is 0.21 km while the elevation angle is 46 deg. These statistics are proved extremely important for the calculation of the dynamic fade margin of a station. Moreover it can be easily observed the rain attenuation is extremely dependent of the operation frequency.

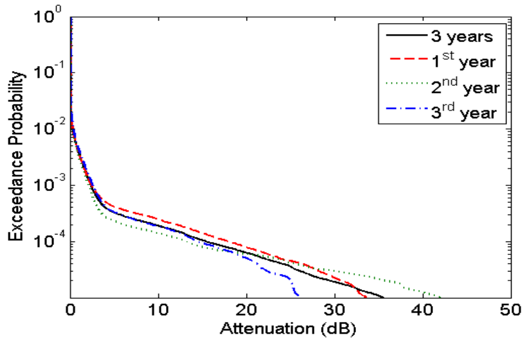

(a)

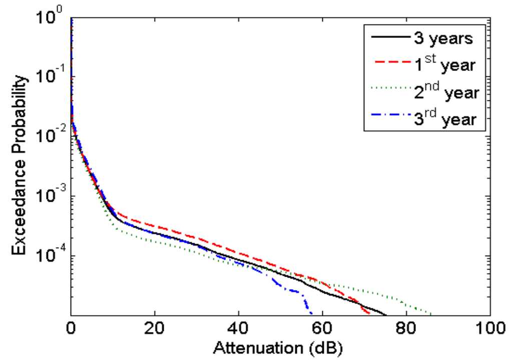

(b)

Figure 2. CCDF rain attenuation: (a) 20 GHz, (b) 40 GHz

Now using the data for both rain gauges which have 387 m separation distance the CCDF of dynamic diversity gain will be computed. Dynamic diversity gain is given [4]:

$$G_D(t) = A_{ref}(t) - A_{joint}(t) \tag{1}$$

This expression defines diversity gain on temporal domain where A_{ref} is the rain attenuation induced in a single satellite slant path used as reference while A_{joint} is:

$$A_{joint}(t) = \min(A_1(t), \ldots A_N(t)) \tag{2}$$

where A_i with i=1,…N is the induced rain attenuation in each link used in the diversity scenario. The reception scheme is considered as a selection combining scheme [1]. In Figure 3 the CCDF of dynamic diversity gain for the two operating frequencies is presented. It can be pinpointed that even in such small separation distance there is significant diversity gain. Moreover the dynamic diversity gain dependency on frequency is made explicit

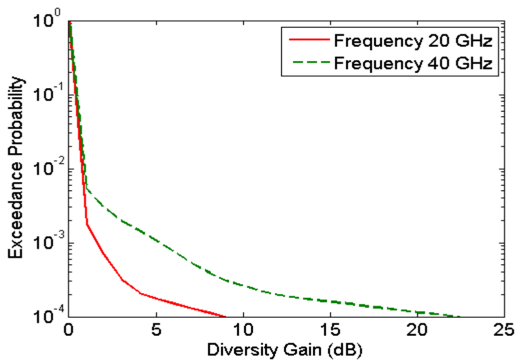

Figure 3. CCDF of dynamic diversity gain for two operating frequencies at 20 and 40 respectively

In Figure 4 the CCDF of dynamic diversity gain for two elevation angles 46deg and 35deg is presented. Frequency is assumed to be 20 GHz. It can be pinpointed that dynamic diversity gain is higher for lower elevation angles.

From Figures 3 and 4 it can be easily observed that the reduction of consumed power can be achieved using effective diversity techniques.

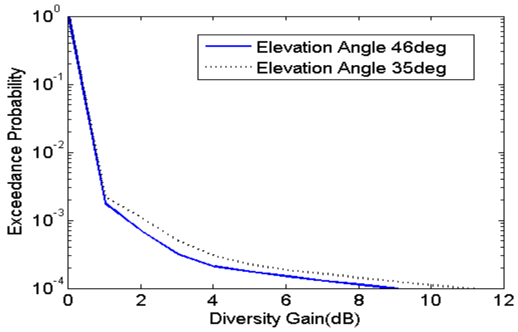

Figure 4. CCDF of dynamic diversity gain for two elevation angles 46deg and 35deg and operating frequency at 20 GHz

7. CONCLUSION

In this contribution we exploit statistical propagation models and simulated total attenuation data for the design of energy efficient FMTs in modern broadband satellite communication systems. FMTs are proposed in order to protect the system from atmospheric attenuation and reduce the power consumption

References

[1] D. Panagopoulos, et al, "Satellite Communications at Ku, Ka and V bands, Propagation Impairments and Mitigation Techniques", IEEE Communication Surveys and Tutorials, 3rd Quarter, pp.1-13, October2004.

[2] D. Panagopoulos, "Propagation Phenomena and Fade Mitigation Techniques for Fixed Satellite Systems", Book Chapter in the Book "Radio Wave Propagation and Channel Modeling for Earth-Space Systems", Taylor and Francis CRC Press, May 2016.

[3] E. Matricciani, "Physical-mathematical model of the dynamics of rain attenuation based on rain rate time series and two-layer vertical structure of precipitation," Radio Sci., vol. 31, no. 2, pp. 281–295, 1996.

[4] I. Kourogiorgas, A. D. Panagopoulos, S. N. Livieratos, and G. E. Chatzarakis, "Dynamic properties of rain attenuation in athens, greece: slant path rain attenuation synthesizer and dynamic diversity gain," Progress In Electromagnetics Research M, Vol. 41, 43-50, 2015.

QOS-DRIVEN ALLOCATION SCHEMES IN SPECTRUM LEASING COGNITIVE RADIO NETWORKS

Anargyros J. Roumeliotis, Athanasios D. Panagopoulos

School of Electrical and Computer Engineering
Iroon Polyrechniou 9, Zografou-Athens GR-15780, Greece

Emails: aroumeliot@mail.ntua.gr, thpanag@ece.ntua.gr

Abstract

In this paper, the cooperative spectrum leasing process between the primary user (PU) and the secondary user (SU) in an overlay cognitive radio network under the Decode and Forward (DF) cooperative protocol is studied. Assuming that both users have specific Quality of Service (QoS) requirements and participate in a three-phase leasing process, a heuristic joint power and time allocation scheme for maximizing the effective capacity of the PU while guaranteeing a minimum effective capacity for the SU is introduced based on convex optimization theory. The numerical results prove the superiority of the proposed mechanism compared to other less sophisticated allocation schemes and noticeable observations for its performance are made under various network parameters.

1. INTRODUCTION

As the diversification of the wireless users' demands grows fast due to the vast amount of handheld devices and the complex wireless environment, the more challenging users' QoS requirements must be satisfied considering in parallel the increasing bandwidth requirements. The spectrum's scarcity in modern wireless communication systems is a great challenge that can be alleviated with the employment of Cognitive Radio (CR) technique [1]. In a CR Network (CRN) the licensed PUs (non-cognitive users) coexist with the unlicensed SUs (cognitive users) in the same spectrum band. The CRN operation is based either on the commons model, where the PUs are oblivious to the presence of SUs or the property rights model (known as spectrum leasing), similar to our scenario, where the PUs cooperate with the SUs so as to ameliorate their performance and the cooperative protocols that are mostly employed are the amplify-and-forward (AF) protocol, the decode-and-forward (DF) protocol and the compress-and-forward (CF) protocol. Additionally, both types of users apply one of the three basic dynamic spectrum access (DSA) techniques: overlay, interweave or underlay. Generally, the employment of the overlay approach, similar to our scenario, leads the SU to act as relay for the PU by devoting a part of its own transmission power to eliminate the impact of the interference caused to the primary transmission and simultaneously the SU acquires time for its own (secondary) transmission.

A significant challenge for modern communications is provision of higher QoS level for the wireless applications. Towards this direction, the effective capacity concept, which is defined as the maximum constant arrival rate, supported by the channel to guarantee a QoS requirement [2], is particularly convenient for analysing the statistical QoS performance of wireless transmissions where the service process is driven by the time-varying wireless channel.

Furthermore, a recent significant work in resource allocation mechanisms for CRNs related with our paper is [3]. More specifically, the presented work investigates a heuristic joint power and time allocation mechanism for the maximization of the highest priority user's, the PU's, effective capacity under an overlay approach using the DF cooperative protocol, taking also into account the SU's effective capacity requirement and the maximum SU's instantaneous power transmission to treat with a more realistic scenario.

2. SYSTEM MODEL AND GENERAL CONSIDERATIONS

We consider a three-phase transmission scenario of one PU and one SU in an overlay CRN configuration. Specifically, Figure 1 depicts that the transmission frame has duration of T_f and is divided in three phases: the "primary communication" and the "cooperative" phases, lasting $0.5*t_{PT}$ unit times respectively and the "leasing" phase which lasts

$\left(T_f - t_{PT}\right)$ unit times where $t_{PT} = k_{PT}T_f$ $\left(0 \le k_{PT} \le 1\right.$ and the parameter k_{PT} expresses the PU's normalized transmission duration. In particular, first phase is used by the primary transmitter (PT) sending its data to the corresponding primary receiver (PR) and to the secondary transmitter (ST), while in the second phase the ST relays the primary signal and in the third phase the latter transmits its own data to the corresponding secondary receiver (SR).

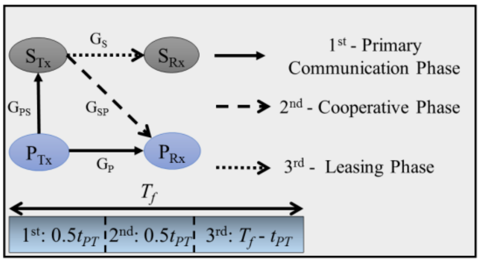

Figure 1. System Model

The wireless links of our model suffer from fading phenomena which are modelled according to Rayleigh distribution, Additive White Gaussian Noise (AWGN) which is modelled as zero-mean independent Gaussian random variable with noise power σ^2 and path loss attenuation according to a loss factor n. Moreover, as it can be seen in Figure 1, the total power gains of PT-PR, PT-ST, ST-PR and ST-SR links are denoted as G_P, G_{PS}, G_{SP} and G_S, respectively. Finally, we must depict that the channels are modelled as independent random variables that remain invariant during a frame, but vary over successive frames.

The time-varying nature of wireless channels which, also, is considered in our scenario and the large variation in the services which are provided by synchronous wireless networks make critical the users' QoS satisfaction which is investigated by the employment of the effective capacity metric, i.e. $E_c(\theta)$ This metric is specified by the QoS exponent θ which is interpreted as the delay QoS exponent [2]. A smaller θ leads to a slower decay rate which implies a looser QoS requirement, while larger θ expresses a more stringent QoS constraint. In the following paper, the normalized effective capacity $E_{c,n}(\theta)$ (bits/sec/Hz), which is defined as the $E_c(\theta)$ divided by the term WT_f, is used and W refers to the system's spectral bandwidth.

3. QOS-DRIVEN JOINT TIME AND POWER ALLOCATION MECHANISM (JTPA)

Due to the lack of space the function $f(G_1,P_1,G_2,P_2) = \left(1+\left(G_1P_1+G_2P_2\right)/\sigma^2\right)$ is defined for a more compact mathematical analysis. Based on the f function, the system's model notations and considering the fixed DF relaying scheme the PU's rate due to the cooperation with the SU is expressed by

$$R_{PU}^{coop} = \frac{Wt_{PT}}{2}\min\left\{\log_2\left(f(G_{PS},P_P,0,0)\right),\log_2\left(f(G_P,P_P,G_{SP},P_S)\right)\right\}$$

where P_P describes the PT's constant transmission power level and P_S depicts the ST's transmission power level, the same for both "cooperative" and "leasing" phases", that is below the ST's maximum power level P_{Smax}. Similarly, the PU's rate without the SU's cooperation, R_{PU}^{dir}, is expressed as $R_{PU}^{dir} = WT_f\log_2\left(f\left(G_P,P_P,0,0\right)\right)$ and the SU's rate, R_{SU}, is defined as

$$R_{SU} = W(T_f - t_{PT})\log_2\left(f\left(G_S,P_S,0,0\right)\right).$$

Based on the aforementioned rate expressions which are measured in *bits per frame* and defining the PU's and SU's normalized QoS exponents for simplicity as $a_j = a_j(\theta_j) = \theta_j WT_f/\ln(2)$ where $j \in \{PU, SU\}$, the final expressions of the corresponding normalized effective capacities, where $\mathrm{E}\left[\cdot\right]$ represents the expected value function, are described similarly with the $E_{c_{PU},n}^{coop}$ which is defined as $E_{c_{PU},n}^{coop}(P_S,k_{PT},\alpha_{PU}) = -\frac{1}{\alpha_{PU}\ln(2)}\ln\left(\mathrm{E}\left[\max\left\{f_1, f_2\right\}\right]\right)$

where $f_1 = f_1(k_{PT},a_{PU}) = \left(1+G_{PS}P_P/\sigma^2\right)^{-\frac{\alpha_{PU}k_{PT}}{2}}$,

$$f_2 = f_2(P_S,k_{PT},a_{PU}) = \left(1+(G_PP_P+G_{SP}P_S)/\sigma^2\right)^{-\frac{\alpha_{PU}k_{PT}}{2}}$$

The proposed **J**oint **T**ime and **P**ower **A**llocation algorithm (**JTPA**) refers to the optimization of the PU's effective capacity ($E_{c_{PU},n}^{coop}$) given a minimum value (E_{SU}) for the SU's normalized effective capacity ($Ec_{SU,n}$) satisfying the constraint $Ec_{SU,n}(\alpha_{SU}) \ge E_{SU}$ and the PU computes both the SU's transmission power level (P_S) and the optimal normalized duration of its own transmission (k_{PT}). Formally, considering that for each timeslot

$0 \le P_S \le P_{S\max}$ and $0 \le k_{PT} \le 1$ due to the system scenario and defining $F(E_{SU}) = e^{-\alpha_{SU}\ln(2)E_{SU}}$, the optimization problem is expressed as:

$$\begin{aligned} &\max_{P_S, k_{PT}} E^{coop}_{c_{PU},n}(P_S, k_{PT}, a_{PU}) \triangleq \min_{P_S, k_{PT}} \mathrm{E}\left[\max\{f_1, f_2\}\right] \\ &\text{s.t. } \mathrm{E}\left[\left(1+(G_S P_S)/\sigma^2\right)^{-a_{SU}(1-k_{PT})}\right] \le F(E_{SU}) \end{aligned} \quad (1)$$

The **JTPA** problem is not convex, so we treat it heuristically in two steps: first over the SU's cooperative transmission power P_S and then over the duration of the primary transmission k_{PT}. So the equation $f_1=f_2$ results in the closed form expression $P_S^* = \left(\left(G_{PS} - G_P\right)P_P\right)/G_{SP}$ which must satisfy the constraint $0 \le P_S^* \le P_{S\max}$. Hence, the substitution of the P_S^* in the objective function of (1) simplifies the optimization problem as $\mathrm{E}\left[\max\{f_1, f_2\}\right] \triangleq \mathrm{E}\left[f_1\right]$ and is easily concluded that the modified objective function of (1) is convex versus k_{PT} and has a global optimal solution k_{PT}^* which is obtained using the Lagrangian approach

$$L = \mathrm{E}\left[f_1\right] + \lambda\left(\mathrm{E}\left[\left(1+(G_S P_S)/\sigma^2\right)^{-a_{SU}(1-k_{PT})}\right] - F(E_{SU})\right),$$

where λ is determined from the SU's minimum effective capacity requirement of (1). The optimal solution k_{PT}^* is defined as:

$$k_{PT}^* = -\frac{\ln\left[\dfrac{2\lambda a_{SU}\ln(f(G_S, P_S, 0, 0))}{\alpha_{PU} f^{a_{SU}}(G_S, P_S, 0, 0)\ln(f(G_{PS}, P_P, 0, 0))}\right]}{\ln\left[f^{\frac{\alpha_{PU}}{2}}(G_{PS}, P_P, 0, 0) f^{a_{SU}}(G_S, P_S, 0, 0)\right]} \quad (2)$$

Finally, for comparison reasons, we examine two other allocation schemes that both treat with a Constant PU's **T**ime duration satisfying the SU's minimum effective capacity constraint and the SU's **P**ower **A**llocation strategy is based either on the expression of P_S^*, called as **PA/CT** mechanism**,** or on a **C**onstant SU's power level P_S, called as **CP/CT** mechanism.

4. SIMULATION RESULTS

In this Section, we investigate the performance of the proposed mechanism in MATLAB. The wireless channels are modelled as unit mean Rayleigh channels with path loss attenuation n=4. For the rest of the system parameters, without loss of generality, we assume T_f=1sec, σ^2=1, W=1Hz, α_{PU}=10 bit^{-1}, α_{SU}=0.01 bit^{-1}, P_P=P_{Smax}=1 W, d_{PTPR} =1 m and d_{STSR}=d_S= $d_{PTPR}/10$ to model the smaller SU's geographical deployment. Furthermore, any variations in the above mentioned values are been noticed in the corresponding figures. For the following analysis, we also consider the factor $\rho = d_{PTST}/d_{STPR}$ which describes the accurate position of the ST and three, indicatively, different ST's positions as the latter approaches the PR are examined, i.e. ρ=1, ρ=1.5 and ρ=2.33 respectively. Moreover, the values of the metrics have been computed through 10^4 Monte-Carlo simulations of the fading channel conditions that have been enough in order to have converged results.

Figure 2 presents the increase of the Ec_{PU} as the k_{PT} increases for both cooperative schemes, i.e. PA/CT and CP/CT and the better performance of the former scheme, based on the relation of P_S^*, in comparison with the SU's constant power cooperative scheme. Moreover, the aforementioned cooperative mechanisms outperform the corresponding metric of PU's direct transmission after smaller values of k_{PT} as the ST comes closer to PT showing that the PT is more benefited when the relay is closer. In parallel, in Figure 3 is apparent the decrease of the Ec_{PU} either as the α_{PU} or the E_{SU} becomes stricter explained by the corresponding results of Figure 4 (a). Additionally, in PU's terms the superiority of the proposed JTPA scheme is obvious compared with the PA/CT and CP/CT schemes. Finally, the PU is more benefited as the ST's cooperative power level increases.

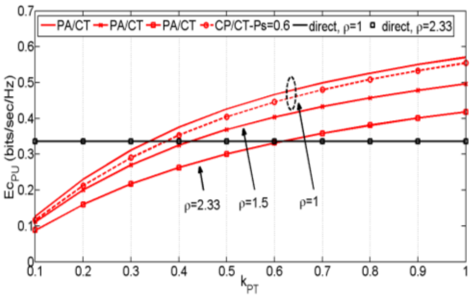

Figure 2. PU's Normalized Effective Capacity vs the k_{PT}

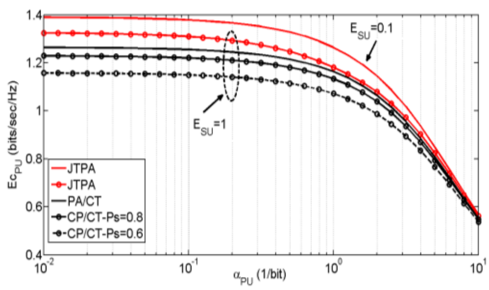

Figure 3. PU's Normalized Effective Capacity vs the a_{PU} for ρ=1

Considering the JTPA scheme in Figure 4 (a), (b) and assuming the proportionality of the Ec_{PU} with the k_{PT} by Figure 2, it is easily explained the amelioration of the Ec_{PU} as d_{STSR} or α_{PU} decreases in Figure 4 (b) due to the corresponding increase in the $\mathrm{E}\left[k_{PT}^{*}\right]$ as depicted in Figure 4 (a).

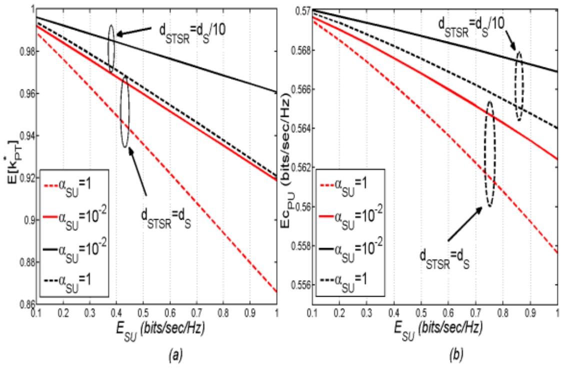

Figure 4. (a) Mean value of k_{PT} and (b) PU's Normalized Effective Capacity vs the E_{SU} for ρ=1

5. CONCLUSION

An overlay CRN has been studied and the cooperative JTPA allocation mechanism is proposed from the PU's side to determine the duration of the cooperation and the SU's transmission power. Besides the benefits of cooperation among PU and SU compared to PU's direct transmission, the application of the JTPA scheme leads to further PU's benefits compared to less sophisticated schemes as the simulation results reveal.

References

[1] J. Mitola et al., "Cognitive radio: making software radios more personal", IEEE Pers. Commun., vol.6, no.4, Aug. 1999, pp.13-18.

[2] D. Wu et al., "Effective capacity: a wireless link model for support of quality of service", IEEE Trans. Wireless Commun., vol. 2, no. 4, July 2003, pp. 630-643.

[3] Y. Wang et al., "Statistical delay QoS protection for primary users in cooperative cognitive radio networks", IEEE Commun. Letters, vol. 19, no. 5, May 2015.

SIMULATING CHROMATIC DISPERSION IN OPTICAL FIBER CHANNELS USING SPLIT STEP FOURIER METHOD

Mihail Mihailov, Georgi Iliev

Technical University of Sofia, Department of Communication Networks
Sofia 1000, Bulgaria

E-mail: mihailmetmihailov@gmail.com; gli@tu-sofia.bg

Abstract

The paper describes a method for simulating the chromatic dispersion in the optical fiber caused by nonlinear effects. This effects are dependent by optical wavelength of the propagated light in the fiber. The method proposed is a numerical solution of the Non Linear Schrodinger equation. Chromatic dispersion is one of the main contributors for degrading of performance in optical transmission systems and shortening the maximum transmission span in the optical line. The method proposed in this paper enables the researchers to evaluate and dimension high capacity optical systems in near future. SSFM enables the possibility to evaluate chromatic dispersion and attenuation in optical fiber versus the optical transmission distance. For simulating beta coefficients to 3rd order are taken into account. The proposed algorithm is written on Matlab simulation platform.

1. INTRODUCTION

Optical fiber properties and their impact to optical transmission systems are essential for developing next generation telecommunication systems [1]. Data volume traffic in the world is rising in exponential rate which increases the demand for creating optical transmission lines with increased capacity and higher throughputs while reducing the operational and maintenance cost of the existing optical transmission lines.

Legacy optical transmission lines are based on an On-Off keying optical modulation schemes [2]. With this modulation increasing the capacity and throughputs is based on shortening the pulses propagated in the optical fiber. The current optical telecommunication systems are at point where the period of the pulse Ts ~ 10ns which increases the impact of nonlinear effects of the silica of the optical fibers and distorting the performance of the telecommunication system [3]. The nonlinear effects in the fiber are shrinking the maximum length of the transmission system which must be evaluated carefully when developing long-haul optical transmission systems.

One of the main factors for limitation of the maximum reach of the transmission line is the chromatic dispersion. The chromatic dispersion is related to the material properties of the optical fiber.

This paper is focused on a simulation model for simulating nonlinear effects in the optical fiber.

2. FIBER TRANSMISSION DYNAMIC

With increasing the baud rate in the optical fiber the nonlinear effects are contributing significantly for the overall performance of the transmission system. Chromatic and polarization dispersion are the main contributors for degrading the BER and SNR at the receiver side.

2.1. Chromatic dispersion

The initial point when mentioning to the chromatic dispersion is the expansion of the mode propagation constant or "wave number" parameter, β, using the Taylor series:

$$\beta(w) = \frac{wn(w)}{c} = \beta_0 + \beta_1 \Delta w + \frac{1}{2}\beta_2 \Delta w^2 + + \frac{1}{3}\beta_3 \Delta w^3 \quad (1)$$

where ω is the angular optical frequency, n(ω) is the frequency-dependent refractive index of the fiber. The parameters

$$\beta_n = \left(\frac{\partial^n \beta}{\partial \omega^n}\right) \Big|_{\omega=\omega 0} \quad (2)$$

have different physical meaning as:

β_0 is involved in the phase velocity of the optical carrier which is defined as

$$v_p = \frac{\omega_0}{\beta_0} = \frac{C_0}{n(w_{0)}} \quad (3)$$

β_1 determines the group velocity of v_g which is related to the mode propagation constant β of the guided mode

$$v_g = \frac{1}{\beta} = (\frac{\partial \ \beta}{\partial \omega})^{-1} \Big|_{\omega=\omega 0} \quad (4)$$

and β_2 is the derivative of group velocity with respect to frequency. Hence, it clearly shows the frequency dependence of the group velocity. This means that different frequency components of an optical pulse travel at different velocities, hence leading to the spreading of the pulse or known as the dispersion [1].

The parameter β_2 is know as GVD (Group Velocity Dispersion). The fiber is said to exhibit normal dispersion for $\beta_2 > 0$ or anomalous dispersion if $\beta_2 < 0$.

A pulse having the spectral width of $\Delta\omega$ is broadened by $\Delta T = \beta_2 L \, \Delta\omega$. In practice, a more commonly used factor to represent the chromatic dispersion of a single mode optical fiber is known as D (ps/nm.km). The dispersion factor is closely related to the GVD $\beta 2$ and given by:

$$D = -2\pi c \beta_2 / \lambda^2 \quad (5)$$

At the operating wavelength λ where $\beta_3 = d\beta_2/dw$ contributes to the calculation of the dispersion slope S(λ) .

This parameter can be obtained by higher order derivatives of the propagation constant.

$$S = \frac{dD}{d\lambda} = \left(\frac{2\pi c}{\lambda^2}\right)\beta_2 + \left(\frac{4\pi c}{\lambda^3}\right)\beta_3 \quad (6)$$

$$L_d = \frac{10^5}{D.B^2} \quad (7)$$

where B is the bit rate (Gb/s), D is the dispersion factor (ps/nm km) and *LD* is in km [2].

This provides a reasonable approximation even though the accurate computation of this limit that depends the modulation format, the pulse shaping and the optical receiver design. Thus, for 10 Gb/s OC-192 optical transmission on a standard single mode fiber (SSMF) medium which has a dispersion of about ±17 ps/nm.km, the dispersion length *LD* has a value of approximately 60 km i.e corresponding to a residual dispersion of about ±1000 ps/nm and less than 4 km or equivalently to about ± 60 ps/nm in the case of 40Gb/s OC-768 optical systems. These lengths are a great deal smaller than the length limited by ASE noise accumulation. The chromatic dispersion therefore, be-comes the one of the most critical constraints for the modern high capacity and long haul transmission optical systems.

$$\delta\omega = -\frac{\delta\varphi_{NL}}{\delta T} = -\gamma \frac{\delta P}{\delta T} L_{eff} \quad (8)$$

From (8), the amount of $\delta\omega$ is proportional to the time derivative of the signal power P. Correspondingly, the generation of new spectral components may mainly occur the rising and falling edges of the optical pulse shapes, i.e. the amount of generated chirp is larger for an increased steepness of the pulse edges.

3. MODELING OF PROPAGATION

Modeling of the optical complex envelope of optical pulses can be described by the well known Nonlinear Schroedinger Equetion (NLSE).

$$\frac{\partial \ A(z,t)}{\partial z} + \frac{\alpha}{2} A(z,t) + \beta_1 \frac{\partial \ A(z,t)}{\partial t} + \frac{j}{2}\beta_2 \frac{\partial^2 A(z,t)}{\partial t^2} - \frac{1}{6}\beta_3 \frac{\partial^3 A(z,t)}{\partial t^3} = -j\gamma |A(z,t)|^2 A(z,t) \quad (9)$$

where z is the spatial longitudinal coordinate, α accounts for fiber attenuation, β_1 indicates the differential group delay (DGD), β_2 and β_3 represent the second and third order factors of GVD and γ is the nonlinear coefficient. Equation (11) involves the following effects in a single-channel transmission fiber:

1) the attenuation, 2) chromatic dispersion, 3) 3rd order dispersion factor i.e the dispersion slope, and 4) self phase modulation nonlinearity.

Other critical degradation factors such as the nonlinear phase noise due to the fluctuation of the optical intensity caused by ASE noise via Gordon-Mollenauer effect is mutually included in the equation.

Thus, in SSFM, the linear operator representing the effects of fiber dispersion and attenuation and the nonlinearity operator taking into account fiber nonlinearities are defined separately as

$$D = \frac{i\beta_2 \partial^2}{2\partial \ \ T^2} + \frac{\beta_3 \partial^3}{6\partial T^3} - \frac{\alpha}{2} \quad (10)$$

$$N = i\gamma |A|^2 \quad (11)$$

where *A* replaces A(z,T) for simpler notation and *T=t-z/vg* is the reference time frame moving at the group velocity. The NLSE equation can be rewritten as:

$$\frac{\partial\ A}{\partial z} = (D + N)A \qquad (12)$$

and the complex amplitudes of optical pulses propagating from z to z+ is calculated using the approximation is given:

$$A(z + h, T) \approx e^{(hD)}\, e^{(hD)}\, A(z, T) \qquad (13)$$

Equation (13) is accurate to second order in the step size *z*. The accuracy of SSFM can be improved by including the effect of the nonlinearity in the middle of the segment rather than at the segment boundary as illustrated in Equation (14) can now modified as:

$$A(z + \delta z) \approx \exp\left(\frac{\delta z D}{2}\right) \exp\left(\int_{z}^{z+\delta z} N(z) dz\right) \exp\left(\frac{\delta z D}{2}\right) A(z, T) \qquad (14)$$

This method is accurate to third order in the step size *z*. The optical pulse is propagated down segment from segment in two stages at each step. First, the optical pulse propagates through the first linear operator (step of *z*/2) with dispersion effects taken into account only. The nonlinearity is calculated in the middle of the segment. It is noted that the nonlinearity effects is considered as over the whole segment. Then at z+*z*/2, the pulse propagates through the remaining *z*/2 distance of the linear operator. The process continues repetitively in executive segments *z* until the end of the fiber. This method requires the careful selection of step sizes *z* to reserve the required accuracy.

The Simulink model of the lightwave signals propagation through optical fiber is shown in Figure 1.

4. RESULTS

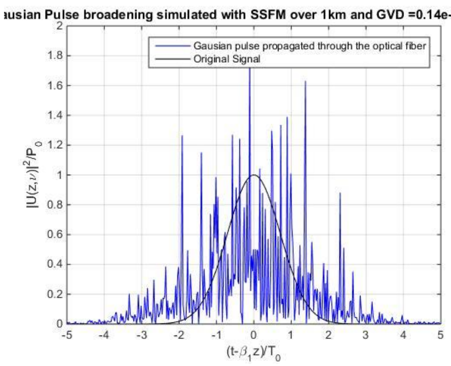

Figure 1. Gausian pulse propagated over fiber with GVD = 0.014 [ps^2/nm].

In figure 2 is showed the broadening of the gausian impulse propagated through optical fiber. On Y axis is showed the nominal Amplitude of the signal. On X axis is showed the broadening of the signal related to time.

After certain distance the broadening of the optical impulse increases the initial period of the signal. This effects are caused by the chromatic dispersion of the optical fiber. This broadening of the optical impulse can cause ISI in high speed transmission links which can degrade the overall performance of the system which reduces the throughput of the optical link.

Figure 3 shows the broadening of the signal related to the nominal distance of the link which spans in the range of Z/L=[0,1];

From this figure it is shown that after certain distance the chromatic dispersion cannot be compensated. This defines and active length of the link beyond that chromatic dispersion must be compensated with other active or passive systems.

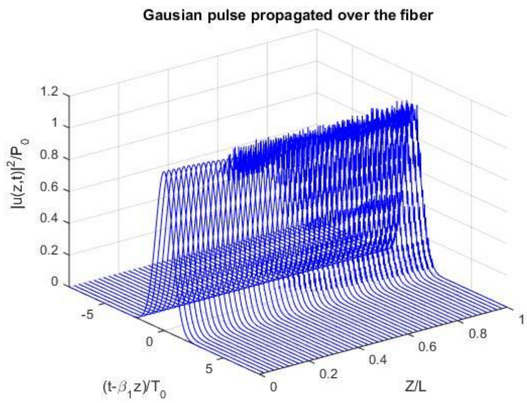

Figure 2. 3D presentation of the optical signal, correlated with distance, broadening and nominal amplitude of the signal.

5. CONCLUSIONS

We have demonstrated a way for simulating a chromatic dispersion in optical fiber using Matlab simulation. The Split Step Fourier Method is a good approximation of the Nonlinear effects in the optical fiber. The mathematical solution gives the possibility to simulate and evaluate the pulse broadening caused by chromatic dispersion in the optical fiber. Also the current mathematical solution gives the possibility to simulate high speed optical links and the performance in the optical fiber. This solution unlocks the possibility to simulate higher order modulation schemes and the impact to overall performance.

References

[1] Peter J. Wizner, Information Theory and Digital Signal Processing in Optical Communications, 2011.

[2] Ezra Ip, Alan Pak Tao Lau, Daniel J. F. Barros, Joseph M. Kahn, Coherent Detection in Optical Fiber Systems, 2006.

[3] M. Lima, J. L. Pinto, Nonlinear Refractive Index and Chromatic Dispersion Simultaneous Measurement in Non Zero Dispersion Shift Optical Fibers, 2007.

ON SOME QUESTIONS CONCERNING TO THE MULTIFRACTAL SPECTRA CALCULATION

N. Ampilova, V. D. Sergeev, I. Soloviev

St. Petersburg State University, Math. & Mech. Faculty,

E-mail: n.ampilova@spbu.ru; vlad.sergeev.spbgu@gmail.com; i.soloviev@spbu.ru

Abstract

The methods of multifractal analyses are now widely used because they allow us to describe digital images with complex structure. For an image one may a set of fractal dimensions of its subsets – multifractal spectrum. There are two kinds of spectra – multifractal and Renyi spectra. Theoretically they are connected by the Legendre transform, but when working with experimental data this relation may not be true due to the dependence of results on many factors. Nevertheless the obtained multifractal characteristics may be successfully applied to image classification. We discuss some problems connected with spectra calculation and results of experiments.

1. INTRODUCTION

The number of high-resolution digital images having complex structure grows steadily in various areas of scientific exploration. These data are of great importance in biology, medicine, geology. Currently there is the tendency to apply fractal and multifractal methods for analysis and classification of such images, because these methods are more appropriate to describe complex textures.

Fractal methods are based on the assumption that a measure of an element of the image partition (cell or box) is approximately equal to the cell size to a power. Fractal sets may be characterized by one power, which is called also by scaling or singularity power. In particular capacity dimension is determined by this power. For multifractal sets, which are unions of different fractals, one can obtain a set of dimensions — multifractal spectrum. This characteristic may be used as a classification criterion for image analysis.

It should be noted that the calculation of multifractal characteristics is based on using so called statistical (information) approach. The natural measure distributed on the image is expressed in terms of pixel intensities. It is calculated for each cell, and then the measure is normed, so we obtain a probability distribution.

There are two spectra describing a multifractal set: the spectrum of Rényi dimensions and multifractal spectrum. Theoretically, there is a connection between them that is called the Legendre transform. But such is not necessarily the case for experimental data. The discussion of possible reasons and results of calculation for some classes of images are given in [4, 6].

In our practice we calculated both spectra for complex texture images from various classes of biomedical preparations. This work summarizes the obtainned results and discusses possible reasons of discrepancy between typical multifractal spectrum and the spectra constructed by experimental data.

2. MULTIFRACTAL SPECTRA, STATISTICAL SUM AND OTHERS

Textures are often may be considered as fractal (or multifractal) sets. Fractal sets have a self-similarity property that may be characterized by a scaling exponent. A union of several fractals, which of them has its own fractal dimension, is called multifractal. It is usually assumed that an image is partitioned by cells with size l, the number of cells is $N(l)$ and the measure of i-th cell

$$p_i(l) \sim l^{\alpha_i}. \quad (1)$$

The numbers α_i are called singularity (scaling) exponents. Then we combine cells with close exponent values in subsets and calculate fractal dimensions $f(\alpha_i)$. Hence we have a correspondence $(\alpha, f(\alpha))$. Fractal dimensions form so called multifractal spectrum.

In many cases the graphic of multifractal spectrum has a canonical parabolic form [3,5,6]. The situation may be illustrated for two-scale Cantor set or the attractor of baker transformation, when one can define a measure distribution by analytical way. But for complex textures the obtained graphic may differ from the canonical one considerably.

There is another kind of spectrum – Renyi dimensions. Consider a partition of an image, a measure $p_i(l)$, and the generalized statistical sum

$$\varphi(q,l) = \sum_{i=1}^{N(l)} p_i^q(l)\ , \qquad (2)$$

where q is a real parameter.

We assume that there is such a function $\tau(q)$ that

$$\varphi(q,l) \sim l^{\tau(q)}. \qquad (3)$$

Then $\tau(q) = \lim_{l\to 0} \frac{\ln \varphi(q,l)}{\ln l}$, and Renyi spectrum is defined as

$$D_q = \frac{1}{q-1}\tau(q). \qquad (4)$$

For q = 0, 1, 2 we obtain capacity, information and correlation dimensions respectively.

One may obtain a connection between these spectra. We assume that the number of cells whose singularity exponents are in interval of the length α is also distributed by a power law, i.e. there is a distribution function $dn = l^{-f(\alpha)}d\alpha$. Then we substitute the cell measure in statistical sum (taking into account (1)), express the sum by using the distribution function as an integral, and for any q find a condition when the statistical sum is maximal. These actions result in obtaining the relation

$$f(\alpha) = \alpha q - \tau(q), \alpha = \tau'(q), \qquad (6)$$

which is well known as the Legendre transform from variables $(q, \tau(q))$ to $\left((\alpha, f(\alpha)\right)$.

When $f(\alpha)$ and D_q are smooth function of α and q, $f(\alpha)$ may be obtained from this relation. But in practice we usually know D_q only in several points with variable precision, so the application of the Legendre transform is incorrect.

In this connection in [3] a method of the calculation of multifractal spectrum without using Legendre transform was proposed. Given an initial distribution $\{p_i(l)\}$, construct the sequence of measures $\mu(q,l) = \{\mu_i(q,l)\}$ obtained by the direct multifractal transform:

$$\mu_i(q,l) = \frac{p_i^q(l)}{\sum_{i=1}^{N} p_i^q(l)}. \qquad (5)$$

Then we calculate singularity spectra and the Hausdorff dimensions of the supports of measures $\mu_i(q,l)$ as the functions of the parameter q of the statistical sum. Excluding q we obtain $f(\alpha)$.

3. METHODS OF CALCULATION

One may point out two methods for calculation of the spectrum.

3.1. Density function

This approach was proposed in [7] and used for image segmentation in [1,2].

We consider a special function (density function) to calculate the singularity power for every pixel. Then we combine all the pixels with close values of density function, which results in partition of the image on the subsets – so called level sets. For each level set we calculate its fractal dimension..

Let μ be a measure defined through pixel intensities. For $x \in R^2$ we denote $B(x,r)$ a square of length r with center x. Let $\mu(B(x,r)) = kr^{d(x)}(x)$, where $d(x)$ is the local density function of x and k some constant. Then

$$d(x) = \lim_{r\to 0} \frac{\log \mu(B(x,r))}{\log r}.$$

The density function measures the non-uniformity of the intensity distribution in the square $B(x,r)$. The set of all points x with local density α is a level set

$$E_\alpha = \{x \in R^2 : d(x) = \alpha\}$$

In practice, not to increase the number of level sets, one really consider sets

$$E(\alpha,\varepsilon) = \{x \in R^2, d(x) \in [\alpha, \alpha+\varepsilon)\}.$$

In [2] we constructed spectra for images of healthy liver and liver with a decease. Graphics did not have canonical form and depended from the measure choice considerably.

3.2. Using statistical sum

The second method uses statistical sum (2) and the sequence of measures (5) generated from the initial measure by the direct fractal transform [5]. The method was proposed in [3] and is based on the calculation of the Hausdorff dimension of a measure support M by the formula

$$\dim M = -\lim_{N\to\infty} \frac{\sum_{i=1}^{N} p_i \ln p_i}{\ln N} \qquad (7)$$

The direct multifractal transform results in a transformation of the initial measure by using statistical sum, and hence it depends on *q* as well. For any measure from the generated sequence one may calculate the singularity power averaged over the measure and the fractal dimension of the support of the measure corresponding to this singularity power. Hence we obtain the averaged singularity spectrum $\alpha(q)$, and the fractal dimension of the support of the measure $f(q)$ as functions of the parameter q. Eliminating *q* one can obtain the relation between singularity values and fractal dimensions of corresponding subset.

For each measure $\mu(q,l)$ one can calculate the Hausdorff dimension of its support by formula (7). As q changes, we have a set $f(q)$ of the Hausdorff dimensions of $\mu(q,l)$ supports, where

$$f(q) = \lim_{l\to 0} \frac{\sum_{i=1}^{N} \mu_i(q,l) \ln \mu_i(q,l)}{\ln l} = \lim_{l\to 0} \frac{f(q,l)}{\ln l}. \qquad (8)$$

We also calculate averaging exponents over the measure $\mu(q,l)$, i.e.

$$\sum_{i=1}^{N} \alpha_i \mu_i(q,l) = \frac{\sum_{i=1}^{N} ln\, p_i(l) \mu_i(q,l)}{ln\, l} = \frac{\alpha(q,l)}{ln\, l},$$

and then the limit $\alpha(q)$ of these averagings when $l \to 0$. Hence, we obtain

$$\alpha(q) = \lim_{l\to 0} \frac{\alpha(q,l)}{\ln l}. \qquad (9)$$

Such a method allows us to obtain the set of dimensions (multifractal spectrum) $f(q)$ and the set of averaging exponents $\alpha(q)$ as functions of the parameter *q*.

In practice, to obtain the above values by (8) and (9), we should do the following. For every *q* we take several values of variable l, calculate sets of points $(\ln l, f(q,l))$ and $(\ln l, \alpha(q,l))$ respectively. Then, by using the least square method, we determine the approximate values of $f(q)$ and $\alpha(q)$. Thus, we have the set of the Hausdorff dimensions of the supports of the measures that are obtained from the initial measure by the direct multifractal transform.

It is interesting to note that substituting $\mu_i(q,l) = \frac{p_i^q(l)}{\sum_{i=1}^{N} p_i^q(l)}$ in (8) we obtain

$$f(q) = \lim_{l\to 0} \frac{\sum_{i=1}^{N} \mu_i(q,l)\, ln\, \mu_i(q,l)}{ln\, l} =$$

$$\lim_{l\to 0} \frac{\sum_{i=1}^{N} \mu_i(q,l)\, ln \frac{p_i^q(l)}{\sum_j p_j^q(l)}}{ln\, l} =$$

$$q \lim_{l\to 0} \frac{\sum_{i=1}^{N} \mu_i(q,l)\, ln\, p_i(l)}{ln\, l}$$
$$- \lim_{l\to 0} \frac{\sum_{i=1}^{N} \mu_i(q,l)\, ln\, \varphi(q,l)}{ln\, l} =$$

$$q\alpha(q) - \lim_{l\to 0} \frac{ln\, \varphi(q)}{ln\, l} = q\alpha(q) - \tau(q).$$

Besides that,

$$\frac{d\tau(q)}{dq} = \lim_{l\to 0} \frac{1}{ln\, l} \frac{\sum_i p_i^q(l)\, ln\, p_i(l)}{\sum_j p_j^q(l)} =$$

$$\lim_{l\to 0} \frac{\sum_i \frac{p_i^q(l)}{\sum_j p_j^q(l)}\, ln\, p_i(l)}{ln\, l} =$$

$$\lim_{l\to 0} \frac{\sum_i \mu_i(q,l)\, ln\, p_i(l)}{ln\, l} = \alpha(q).$$

Experiments were performed for Brodatz textures and various classes of biomedical preparation images. Practically in all cases the obtained graphics did not correspond the expected canonical form. We illustrate the situation for the image of pharmacological solution of Ag. (Fig.1)

The measure of a cell is the ratio of the sum of pixel intensities to the sum of intensities for the whole image. The calculations were performed for H component of HSV palette

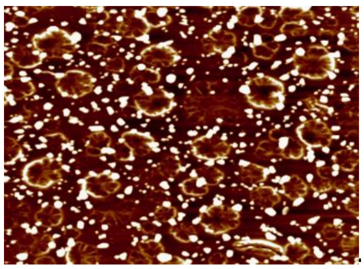

Fig. 1. Pharmacological solution of Ag

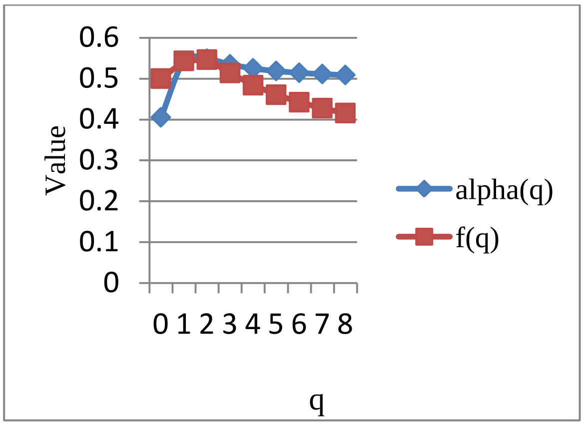

Fig. 2. Singularity and multifractal spectra

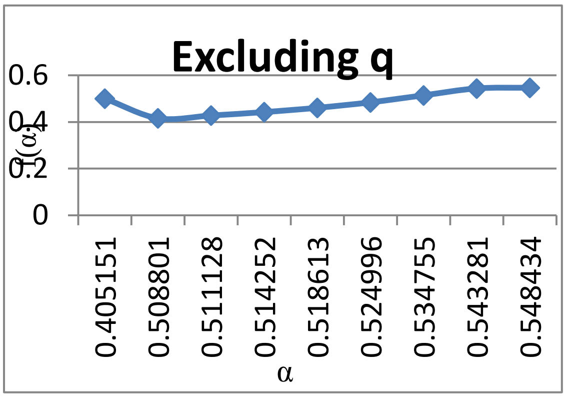

Fig. 3. Graphic $f(\alpha)$ obtained by excluding q

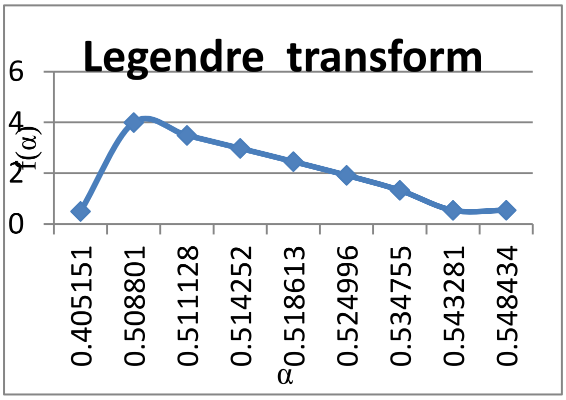

Fig. 4. Graphic $f(\alpha)$ obtained by Legendre transform

CONCLUSION

There are a lot of reasons that influence on the results. First and foremost the subsets of a multifractal are arranged by rather complicated manner, so that the problem of their separation may be solved only approximately. The cell measure may be calculated as the ratio the sum of pixel intensities of the cell to the common sum of intensities of the whole image, or as the ratio of the number of black pixels to the common number of black pixels (or the same for white ones), which means the implicit binarization of a grayscale image. For color images their reducing to grayscale ones may lead to a loss of the image structure, so we should consider the palette components separately. It is unknown a priori if the averaged characteristics may give a good approximation to the image measure. The question how to choose the range for *q* is also may be solved experimentally. It is easy to understand that there are no common rules to select the parameters for calculation, because they are defined by an image structure to a great extent.

Our experiments show that when using both the described methods we may not obtain canonical graphics due to dependence of results on many factors.

This circumstance should not prevent us from applying these techniques for calculation multifractal characteristics that are classification criteria in digital image analysis.

References

[1] N. Ampilova, I. Soloviev. Application of Fractal and Multifractal Analysis Algorithms to Image Segmentation and Classification. WSEAS Transactions on Biology and Biomedicine, ISSN / E-ISSN: 1109-9518 / E-ISSN: 2224-2902, Volume 13, 2016, Art. #3, pp. 14-21.

[2] N. Ampilova, Y. Shupletsov. Image segmentation algorithm based on multifractal spectrum computing. Proc. 9 Int. Conf. CEMA14, 16-18 Oct. 2014, Sofia, Bulgaria. p. 39-42.

[3] S. Bogokin, D. Parshin. Fractals and multifractals, Moscow, 2001(in Russian)

[4] Ashvin B. Chhabra, Charles Meneveau, Roderick V. Jensen and K.R. Sreenivasan.Direct determination of the f(α) singularities spectrum and its application to fully developed turbulence — Physical Review A, Volume 40, Number 9, November 1,1989. pp. 5284-5294.

[5] S. Kuznetsov. Dynamical chaos (in Russian). Moscow, 2013.

[6] G. V. Vstovsky. Elements of information physics, M., 2002.

[7] Yong Xu, Hui Ji, Cornelia Fermuller. Viewpoint Invariant Texture Description Using Fractal Analysis. Int. J. Comput. Vis (2009) 83, pp.85-100.

HUMAN EXPOSURE STUDY FOR SOME SCENARIOS

Tamar Nozadze, Revaz Zaridze, Veriko Jeladze, Vasil Tabatadze,Ivan Petoev, Mikheil Prishvin

Tbilisi State University, Laboratory of Applied Electrodynamics and Radio Engineering
3, Chavchavadze Ave. 0176, Tbilisi, Georgia

E-mail: revaz_zaridze@mail.ru, tamar.nozadze002@ens.tsu.edu.ge

Abstract

In this article The main aim of the research is to investigate EM exposure influence on a human homogenous model located in a car and study possible resonant fields. This problem is very topical, because in some cases the excitation source is located in vicinity to the sensitive tissues. We have investigated several cases when a human with a cellphone is located inside a car and also the case when the EM source is the base station antenna. The problems are solved using the Method of Auxiliary Sources (MAS) with a user friendly program package, created for numerical experiments realization for these particular problems. The results of the numerical experiment are presented and analyzed.

1. INTRODUCTION

With the rapid development of new technologies, such as mobile phones and other communication systems, exposure of users to electromagnetic fields (EMF) has enormously increased in recent years. It is important to study their EM influence on human, because excitation source is very close to the sensitive tissue. Also it is important to obtain some general conclusions about the nature of exposure process, in order to elaborate some safety recommendations and standards. Our goal in this research is to investigate EM influence on human, when is located inside the car and study the fields' behaviour in the near and far zone. There are many factors to consider, like complex body geometry [1], [2], location in an enclosed or semi-enclosed room, wall transparency and users hand position, etc. It is impossible to thoroughly quantitatively consider all these details, but we can estimate most importance of them.

In spite of many works on this issue, the problem is not studied completely. EM absorption by human is measured in terms of specific absorption rate (SAR), SAR values show the radiated power from mobile phone absorbed by the human over a particular volume of body tissue corresponding to 1g or 10 g of body tissues [3] and it is measured in watt per kilogram (W/kg) [4].

In the article [5] are investigated several scenarios with Mummy; one is when the Mummy is located inside of a room while talking over the mobile phone. The other is when the Mummy is located inside of the room but the EM source is a base station located outside. For these cases are studied the influence of the room walls transparency on the formation of the near field inside the room and far field pattern. As the numerical experiments shows, in some cases, the room behaves as a resonator and amplifies the antenna radiated field. The field value may be amplified and be dangerous for the user The Method of Auxiliary Sources is used to solve efficiently all these problems [6].

2. MODELS, METHODS AND RESULTS OF NUMERICAL SIMULATIONS

2.1. Models and methods

During the EM Exposure influence investigation it is forbidden to conduct real experiments on humans. Because of this the main tools of investigation represents the computer modelling based on numerical methods. We use a homogenous dielectric human shaped body 'Mummy' with averaged permittivity and losses values (according to muscle, bone and blood), since their inhomogeneity does not affect the final results significantly. The use of such model is needed to implement the Method of Auxiliary Sources for calculations diffraction problems on human model for the big scenarios, when it is located inside the car. It is important to take into account the possible resonant effects in the car, study SAR distributions for the human model and near and far field distribution in case of mobile phone and base station antenna.

Application of the MAS is deduced to the construction of two couples of closed auxiliary surfaces inside and outside of the Mummy and also inside and outside of the surrounded surface like the car (Figure 1).

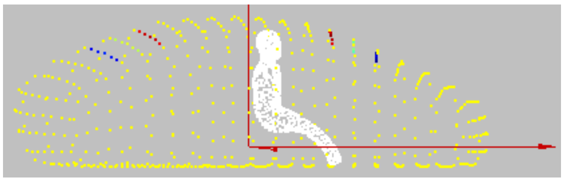

Figure 1. MAS model of cavity with using auxiliary surfaces

The calculations were conducted for frequencies used in the standard mobile frequency range.

2.2. Results of numerical simulations

In this paper we introduce a new approach to use the MAS methodology. Our final goal is to find the near field distribution inside of the human body as well as inside and outside of the car**.** We consider human homogenous model like Mummy, with complex permittivity, $\varepsilon=45+i2$, (an averaged value considering blood, muscle and bones). Several scenarios have been studied (when source is mobile phone and base station antenna). The EM field incidence angle is 30^0 which means, that base station antenna is located sufficiently near. Obtained results are presented below. Values of the near field distribution and SAR are provided in the relative units.

In the fig.2 a) and fig.3 a) are presented near field distribution in the car, far field pattern and SAR distribution inside of the head at the 300 MHz and 450 MHz, when source is mobile phone are shown on fig.2 b), fig.3 b) and fig.2 c) and fig.3 c) respectively. As it seen from the obtained results at the 300 MHz inside the car is created high reactive field, which might be dangerous for human.

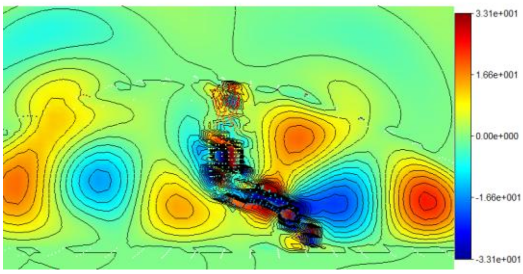

a)

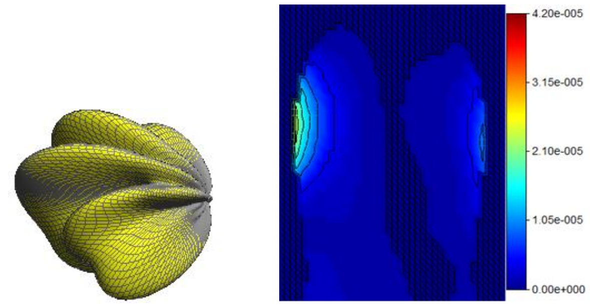

b) c)

Figure 2. Near field distribution in the car (a) and far field pattern (b), SAR distribution inside of human head c) at 300 MHz (source is inside the car).

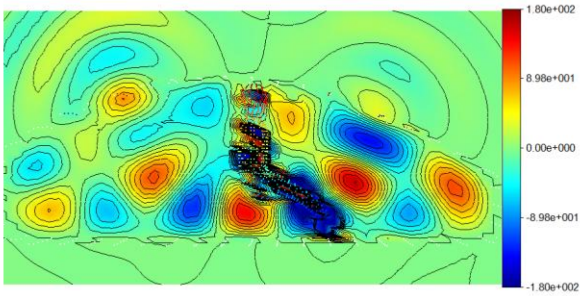

a)

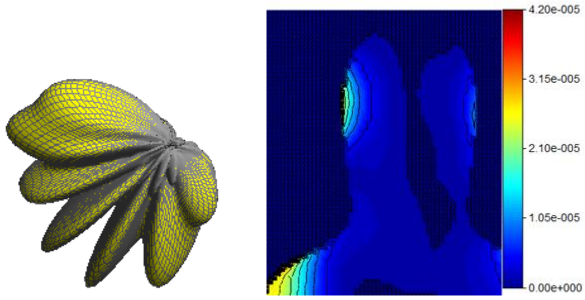

b) c)

Figure 3. Near field distribution in the car (a) and far field pattern (b), SAR distribution inside of human head c) at 450 MHz (source is inside the car).

The near field distribution for the case when the source is the base stations is shown of fig. 4 a). The far field pattern and SAR distribution inside of human head at the 450 MHz are presented on fig. 4 b) and c) respectively.

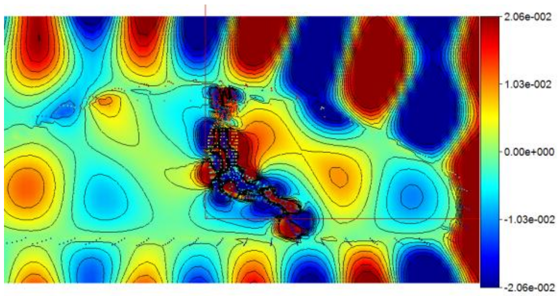

a)

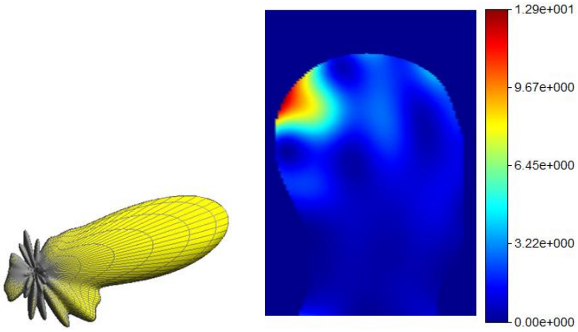

b) c)

Figure 4. Near field distribution in the car (a) and far field pattern (b), SAR distribution inside of human head c) at 300 MHz (source is base station antenna).

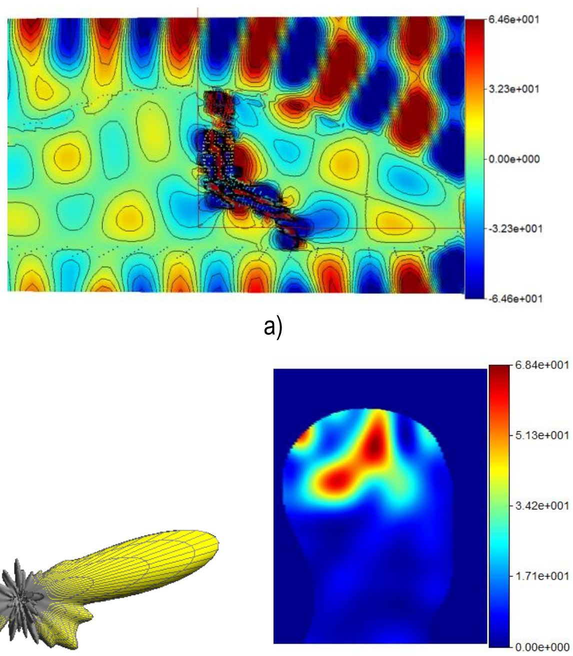

b) c)

Figure 5. Near field distribution in the car (a) and far field pattern (b), SAR distribution inside of human head c) at 450 MHz (source is base station antenna).

At the 450 MHz frequency, in case when source is base station antenna, obtained results are presented on the fig.5. The near field distribution for this case is shown on fig.5 a). For far field pattern we got result which is presented on fig.5 b) and SAR distribution inside of human head is shown on fig.5 c).

3. CONCLUSION

Main conclusions which follow from the study are following: It is not desirable speak on phone for a long time if user is located inside the car. The calculations, conducted with the created program package, showed the presence of resonance and reactive fields in several big scenarios which could be dangerous for a human.We study electromagnetic exposure problem for one human model, in some cases the results will not be applicable for other models. Every human is unique and differs in form, dimensions, weight and so more studies may be needed to make a firm conclusion.

4. ACKNOWLEDGMENT

This study is supported by Shota Rustaveli National Science Foundation grant: YS15_2.12_56.

References

[1] J. Krogerus, J. Toivanen, C. Icheln, and P. Vainikainen, "Effect of the human body on total radiated power and the 3-d radiation pattern of mobile handsets," IEEE Trans. Instrum. Meas., vol. 56, no. 6, Dec. 2007, pp. 2375–2385

[2] M. R. I. Faruque, M. T. Islam, N. Misran, "Effect of human head shapes for mobile phone exposure on electromagnetic absorption", Informacije MIDEM- Journal of Microelectronics, Electronic Components and Materials, vol. 40, no. 3, 2010, pp. 232-23

[3] A. H. Kusuma et al., "A new low SAR antenna structure for wireless handset applications", Progress in Electromagnetics Research, vol. 112, pp. 23-40, 2011.

[4] M. R. I. Faruque et al., "Effect of human head shapes for mobile phone exposure on electromagnetic absorption", Informacije MIDEM, vol. 40, no. 3, pp. 232- 237, 2010.

[5] V. Jeladze, I. Petoev, V. Tabatadze, M. Prishvin, R. Zaridze, "The Method of Auxiliary Sources for Study of Resonant Field Effects upon a Human Models for Big Scenarios", Journal of Communications Technology and Electronics, Moscow, Russia.

[6] J. A. Stratton. *Theory of Electromagnetism*. Moscow: OGIZ, 1948, pp. 383-387.

CHARACTERIZATION OF ROUGH FRACTAL SURFACES FROM BACKSCATTERED RADAR DATA

A. Kotopoulis, G. Pouraimis, A. Malamou, E. Kallitsis and P. Frangos

National Technical University of Athens
9, Iroon Polytechniou Str., GR 157 73, Zografou, Athens, Greece

Tel: +30 210 772 3694, Fax: +30 210 772 2281, E-Mail: pfrangos@central.ntua.gr

Abstract

In this paper the scattering of electromagnetic (EM) waves, emitted by a monostatic radar, from rough fractal surfaces is examined by using the Kirchhoff approximation. We examine here the way that the level of roughness of the fractal surface affects the back-scattered EM wave captured by a radar as a function of frequency (therefore, a 'spectral method'), and whether the roughness of the surface can be estimated from these radar measurements. The backscattering coefficient is calculated for a number of radar frequencies and for different values of the surface fractal dimension. It is found here that the values of the slopes between the main lobe and the first sidelobes of the backscattering coefficient as a function of the wavenumber (frequency) of the incident EM waves increase with the surface fractal dimension. Therefore, we conclude that the magnitude of the above slopes provides a reliable method for the classification of the rough fractal surfaces. The above are also investigated in the presence of electronic noise in the radar receiver (effect of SNR values in the above proposed technique).

1. INTRODUCTION

The scattering of electromagnetic (EM) waves from rough surfaces has been for decades a very interesting subject for scientific investigation. In many cases the main purpose of this research is the characterization of rough surfaces from scattered EM wave data for remote sensing applications, in the microwave or optical regime [1]–[16]. These surfaces can be modelled mathematically with deterministic or random functions [1]–[3]. However, introducing the fractal geometry, these surfaces can be described in a more detailed way in multiscale [1], [3], [8], [17].

In this paper the scattering of EM waves from rough surfaces using the Kirchhoff approximation is examined [1], [2]. In particular, in Section II the mathematical fundamentals for scattering of EM waves from fractal surfaces are summarized [1]–[3].

In Section III our simulation results for the characterization of the rough fractal surfaces from backscattered EM wave data are presented. Finally, conclusions and future related research of ours are described in Section IV.

2. PROBLEM GEOMETRY AND MATHEMATICAL FORMULATION

The geometry of the problem is shown in Fig. 1. An incident EM plane wave illuminates a one – dimensionally rough fractal surface extending from $x = -L$ to $x = L$, as shown in Fig. 1.The angle of incidence of the EM wave is θ_i with respect to the vertical z axis, where the incident and scattered wave vectors are denoted by $\boldsymbol{k}_i$ and $\boldsymbol{k}_s$ respectively [1].

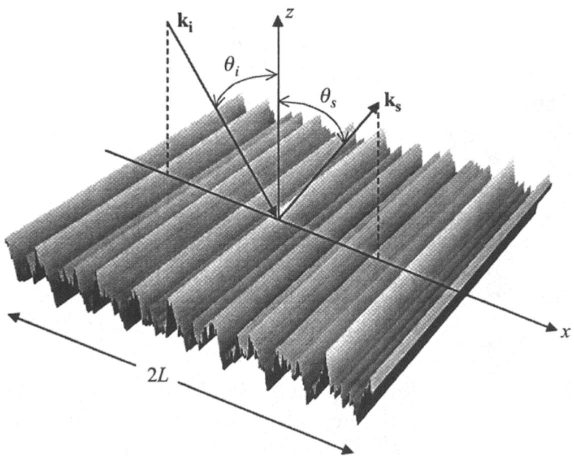

Fig. 1. Geometry of rough surface scattering problem in which an incident plane wave illuminates a fractal surface patch of size $2L$ at an angle θ_i

Following [1], and in order to describe the surface roughness, a one-dimensional fractal function is used [1], [3], [4]. This fractal function is described by the following equation:

$$f_r(x) = \sigma C \sum_{n=0}^{N-1} (D-1)^n \sin(K_0 b^n x + \phi_n) \qquad (1)$$

where D ($1 < D < 2$) is the fractal dimension of fractal surface [1], $K_0 = 2\pi/\Lambda_0$ is the fundamental spatial wavenumber of the fractal surface, Λ_0 is the corresponding fundamental spatial wavelength, b (where $b > 1$) is the spatial frequency scaling parameter, ϕ_n are arbitrary phases and N is the number of tones describing the surface. The amplitude control factor C is given by

$$C = \left\{ \frac{2D(2-D)}{[1-(D-1)^{2N}]} \right\}^{\frac{1}{2}} \tag{2}$$

so that surface function (1), has standard deviation (rms height) equal to σ (see [1]). It can be easily realized from (1) above, that when the surface fractal dimension D increases from value 1 to value 2, the surface roughness also increases (see [1], [3] for more details).

In order to calculate the scattered field from a rough fractal surface, as described in Fig. 1, the Kirchhoff approximation is used in this paper, for which it is assumed that the wavelength of the incident EM wave is small compared to the local radius of curvature of the surface roughness [1]–[3]. Furthermore, for the plane EM wave incidence of Fig. 1, in [1] it is shown that the scattered electric field is given by the following equation:

$$E_{sc} = \frac{ikL\exp(ikR_0)}{2\pi R_0} \int_{-L}^{L} (pf_r' - q)\exp[i\upsilon_x x + i\upsilon_z f_r(x)]dx \tag{3}$$

where

$$p = (1 \quad R)\sin\theta_i + (1+R)\sin\theta_s \tag{4}$$

$$q = (1+R)\cos\theta_s \quad (1 \quad R)\cos\theta_i \tag{5}$$

$$\upsilon_x = k(\sin\theta_i \quad \sin\theta_s) \tag{6}$$

$$\upsilon_z = \quad k(\cos\theta_i + \cos\theta_s) \tag{7}$$

In the above (3)–(7) R_0 is the distance from the observation point (monostatic radar) to the origin, coinciding with the 'source surface point', k is the wavenumber of the incident EM wave ($k=2\pi f/c$, where f is the frequency of the incident EM wave), R is the Fresnel reflection coefficient of the tangential plane at the point of interest, θ_s is the direction of the observer and f_r' is the derivative with respect to its argument (x). For simplicity we assume a perfectly conducting rough surface, in which case the Fresnel reflection coefficient is given by ($R^+ = 1$, $R^- = 1$), where the superscript + indicates the parallel (vertical) polarization and the superscript – denotes the perpendicular (horizontal) polarization, respectively [1], [2].

In the case of a smooth and perfectly conducting surface, the scattered field for horizontal polarization can be found in the direction of specular reflection, namely for $\theta_i = \theta_s$ [1], [2]:

$$E_{sc0} = \frac{i2kL^2\exp(ikR_0)\cos\theta_\iota}{\pi R_0} \tag{8}$$

By normalizing the value of the scattered field E_{sc} of (3) by the value provided by (8), the <u>*scattering coefficient*</u> γ is calculated by [1]:

$$\gamma = \frac{E_{sc}}{E_{sc0}} = \frac{1}{4L\cos\theta_\iota} \times \left(\left(q + \frac{p\upsilon_x}{\upsilon_z} \right) \times \int_{-L}^{L} \exp\left[i\upsilon_x + i\upsilon_z f_r(x)\right]dx - \left\{ \frac{ip}{\upsilon_z} \exp\left[i\upsilon_x x + i\upsilon_z f_r(x)\right] \right\}_{-L}^{L} \right) \tag{9}$$

The first term in the parenthesis provides the most significant contribution to the scattering process, while the second term represents an edge effect, which can be considered negligible when $L >> \lambda$, as assumed in this paper.

3. SIMULATION RESULTS

We concentrate on the backscattering of EM waves from rough fractal surfaces (e.g. monostatic SAR radar [9], [10]), i.e. $\theta_s = -\theta_i$ at Fig. 1 and (4)–(7), and we plot the backscattering coefficient $|\gamma(k)|$ (in magnitude). The surface is simulated as a zero-mean, band-limited fractal function, as in (1), and its roughness is controlled by the fractal dimension D [1], [3]. The backscattering coefficient $|\gamma(k)|$ was calculated from (9) for a number of frequencies $f_m = f_o + (m-1)\Delta f$, where $m = 1,2,...,M$ and M is the number of frequencies, f_o is the carrier frequency, $\Delta f = BW/M$ is the frequency step and BW is the bandwidth of the radar, i.e. 'stepped – frequency' transmitted radar waveform [9], [10]. Furthermore, in Figs. 2–5, below, the plots of $|\gamma(k)|$ for angle of incidence $\theta_i = 30^o$ are shown, while the values of the other parameters are BW=1GHz, f_0 = 10 GHz (initial radar carrier frequency) and M = 200 (i.e. 200 frequency steps in radar emitted stepped-frequency waveform).

As far as the simulated fractal surface is concerned, the frequency scaling parameter was set equal to

$b = 1.8$ while the number of tones was set equal to $N = 6$ [1]. Moreover, the rms height of the surface was set equal to σ = 0.05λ, Λ_0 = 10λ = 0.3 m and the illuminated length of the rough surface along x-direction ('patch size') was chosen to be 2L = 80λ (Fig. 1) in all calculations (so as $2L \gg \Lambda_0$ and $k\sigma$ <1), where $\lambda = c/f_o$ [1], [18].

Furthermore, at the top left corner of each figure a sample plot of the roughness fractal function $f_r(x)$ (1) is also shown.

The roughness of the simulated fractal surface (the fractal dimension D) is increasing per image, e.g. D = 1.05 (Fig. 2), D = 1.30 (Fig. 3), D = 1.55 (Fig. 4), D=1.80 (Fig. 5).

By observing Figs. 2–5, the following conclusion is made: as the value of the parameter D increases, i.e. as the roughness of the fractal surface increases, the emerging slope between the main lobe and the side lobes also increases.

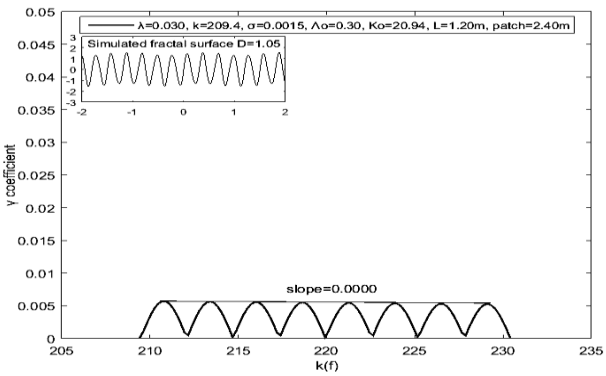

Fig. 2. Magnitude of backscattering coefficient $|\gamma(k)|$, as a function of the wavenumber k, for D = 1.05.

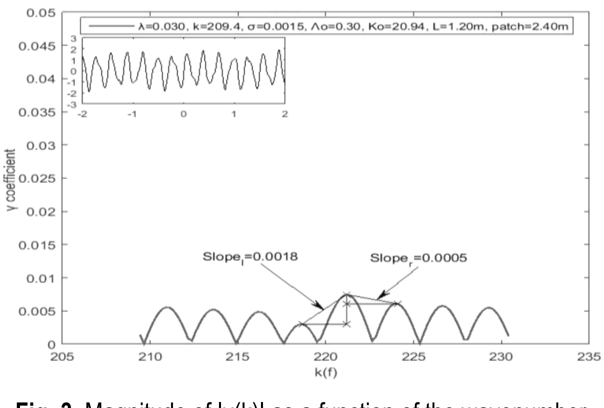

Fig. 3. Magnitude of $|\gamma(k)|$ as a function of the wavenumber k, for D = 1.30.

Therefore, it becomes clear in our simulations that the roughness of the fractal surface can be characterized by the mean slope between the main lobe of function $|\gamma(k)|$ and the two sidelobes, adjacent to the main lobe (see Figs. 2–5).

In Table 1, below, the relation between the fractal dimension D and the slope calculated from each graph is shown. The slope is equal to $|\Delta\gamma|/|\Delta k|$, where $\Delta\gamma$ represents the amplitude difference between the peak of the main lobe and the peak of the first side lobe, while Δk represents the difference of the wavenumbers where these peaks occur.

Table 1. Fractal dimension D and the resulting slope calculations

	Left slope calculations			**Right slope calculations**		
D	**Δγ**	**Δk**	**slope**	**Δγ**	**Δk**	**slope**
1.05	0.0000	0.00	0.0000	0.0000	2.62	0.0000
1.30	0.0044	2.51	0.0018	0.0014	2.93	0.0005
1.55	0.0285	5.03	0.0057	0.0202	3.77	0.0054
1.80	0.0883	3.98	0.0222	0.0819	3.77	0.0217

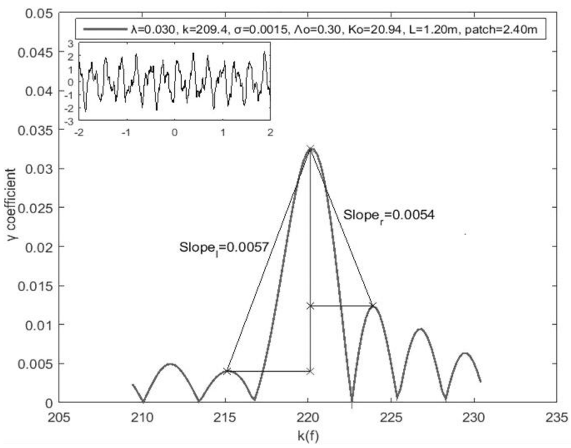

Fig. 4. Magnitude of $|\gamma(k)|$ as a function of the wavenumber k, for D = 1.55.

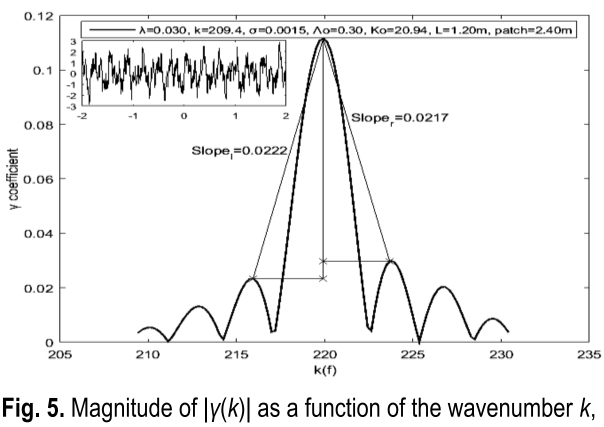

Fig. 5. Magnitude of $|\gamma(k)|$ as a function of the wavenumber k, for D = 1.80.

If the radar bandwidth decreases, then the information provided by the backscattered signal-wavenumber plots, of the type provided above, is not always enough in order to draw safe conclusions regarding the roughness (fractal dimension) of the surface. In other words, the bandwidth for our proposed method of surface characterization from backscattered radar data must be sufficiently large (at least 5% of the carrier frequency f_o), in order that the information contained in the plots of Figs. 2–5 to be observable and measurable.

In order to study further the relation between the surface fractal dimension *D* and the slopes of the scattering coefficient $|\gamma(k)|$, some additional simulations have been performed, as follows. The $|\gamma(k)|$ was calculated sequentially for different values of fractal dimension *D*, *D* = 1.05, 1.10, 1.15, …, 1.85, 1.90 (i.e. here for 18 subsequent values of parameter D), while the rest of the parameters used in these simulations remained the same as in Figs. 2-5. The left and right slope calculations of $|\gamma(k)|$, corresponding to each value of *D*, were averaged, thus creating one average slope calculation of $|\gamma(k)|$ for each value of *D*.

Furthermore, in order also to demonstrate the robustness of our proposed method, we inserted in (1) a uniformly distributed random phase variable φ_n in the interval [0, 2π], for every new surface simulation run, namely for every different *D* value. The calculation results, after 10 simulations for each D value, are presented in Fig. 6, below.

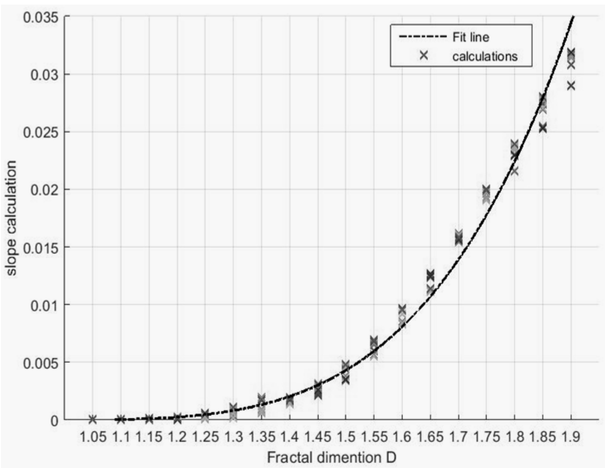

Fig. 6. Average slope' of the $|\gamma(k)|$ vs. value of the surface fractal dimension *D*.

By 'inverting' the data (slope calculations and fitting curve) provided in Fig. 6, the plots of Fig. 7 are provided, where in this case the surface fractal dimension *D* is plotted as a function of the 'slope calculations' of the scattering coefficient $|\gamma(k)|$.

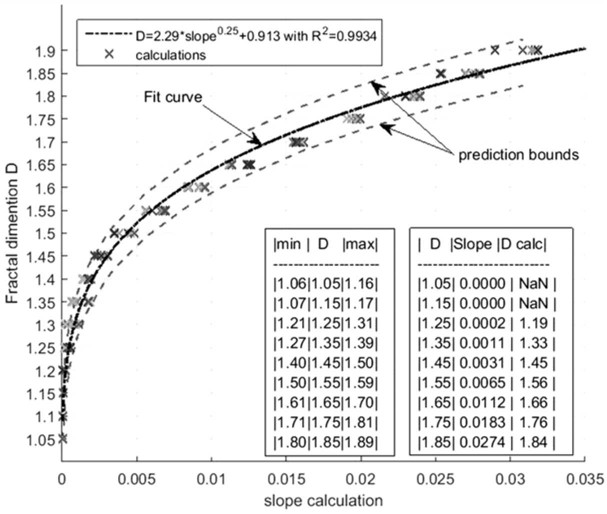

Fig. 7. Value of surface fractal dimension *D* vs. 'slope calculation' of $|\gamma(k)|$.

In Fig. 7 an analytical expression between the 'slope calculation' and the surface fractal dimension *D* has been calculated numerically by 'curve fitting'. Namely, it was found here that an excellent curve fitting exists if the fractal dimension D follows the relation $D = a * slope^b + c$. In Fig. 7 we plot the fit curve by using the following coefficients: *a* = 2.29, *b* = 0.25, *c* = 0.913, and as a measure of fit to our calculations we use '*R*-square criterion for curve fitting', which, for the above simulations, yielded the value R^2 = 0.9934. We plot also the prediction bounds for the fitted curve. The prediction is based on the existing fit to our simulation calculations by using a 90% 'probability of occurrence'. Based on the fitted curve model and the prediction bounds for the fitted curve, Tables 2 and 3 below are presented, as follows :

TABLE 2

ESTIMATION OF D_{CALC}

$$D_{calc} = 2.29 * slope^{1/4} + 0.913$$

D	Slope	D_{calc}
1.05	0.0000	none
1.15	0.0000	none
1.25	0.0002	1.19
1.35	0.0011	1.33
1.45	0.0031	1.45
1.55	0.0065	1.56
1.65	0.0112	1.66
1.75	0.0183	1.76
1.85	0.0274	1.84

TABLE 3

D_{CALC} PREDICTION INTERVAL

USING PREDICTION BOUNDS

D_{calc} lower	*D*	D_{calc} upper
1.06	1.05	1.16
1.07	1.15	1.17
1.21	1.25	1.31
1.27	1.35	1.39
1.40	1.45	1.50
1.50	1.55	1.59
1.61	1.65	1.70
1.71	1.75	1.81
1.80	1.85	1.89

Table 2 presents the value D that was used for the simulation, the slope that was calculated from this simulation and the Dcalc value, which was calculated using our model. For D = 1.05 to D = 1.15, namely for almost smooth surfaces, the slope is almost zero and for these cases our model could not establish a clear D_{calc} value. However for rough surfaces with D > 1.25, our proposed model proved to predict the fractal dimension D of the rough surface with excellent accuracy (see Table 2).

The accurate results of Table 2 gave us the motivation to stress the robustness of our method, by adding random phases φ_n to the rough surface modeling function (1), for each surface simulation. The variability of slope calculations for each value of D in Figs. 7, 8 depicts this added surface randomness. Table 3 presents the prediction intervals for the D_{calc} estimation. This interval indicates that for any new observation from a fractal surface, there exists 90% probability that the value of the fractal dimension of the surface lies within the prediction bounds of this Table 3. This Table demonstrates the fact that our proposed method is accurate and robust enough to characterize a rough fractal surface from backscattered radar data, and also provides a bound estimation for the fractal dimension D of this surface.

Note that if the angle of incidence is $\theta_i \approx \pi/2$ (i.e. EM wave incidence almost parallel to the rough surface, see Fig. 1), and since in this paper we are interested only for the backscatter case, i.e. $\theta_s = -\theta_i$, from (7) it follows that in this case $\upsilon_z \approx 0$, and from (9) we see that our method is *not* applicable in this special case, since the scattering coefficient $|\gamma(k)|$ can not be computed. Summarizing, our proposed method for characterizing a rough fractal surface provides reliable results for appropriate values of radar bandwidth, surface 'patch size' [19] and angle of incidence.

Furthermore in this paper, and in order to examine whether our method could have a practical implementation in a noisy radar environment, we add AWGN noise in $\gamma(k)$. We use eq. (10), below, for calculating the power level $P(\gamma)$ of signal $\gamma(k)$, and eq. (11) for calculating the noise level $N(\gamma)$ for a given SNR value.

$$P(\gamma) = \frac{1}{n}\sum\left|\gamma(m)\right|^2 \tag{10}$$

$$N(\gamma) = \frac{P(\gamma)}{SNR} \tag{11}$$

$$\gamma_{noisy} = \gamma + \sqrt{\frac{P(\gamma)}{SNR}}Norm(0,1) \tag{12}$$

where m=1 to n in the summation of eq. (10), above. The γ_{noisy} in (12) represents a $\gamma(k)$ signal that exhibits a certain SNR value using a Gaussian distribution with specific noise level.

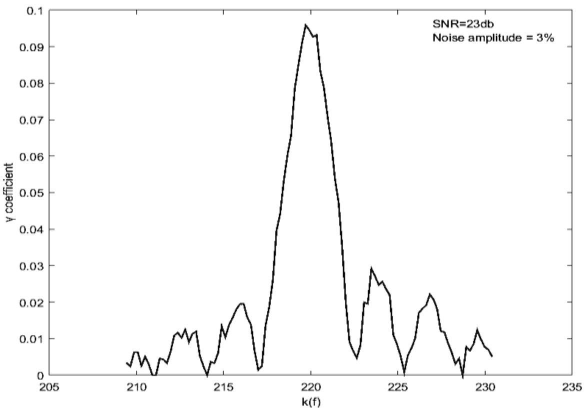

Fig. 8. γ(k) with SNR 23db inserts a noise amplitude 3% of $|\gamma(k)|$ max amplitude.

From figure 8 it is obvious that a signal $\gamma(k)$ exhibiting high SNR=23db does not affect our proposed method.

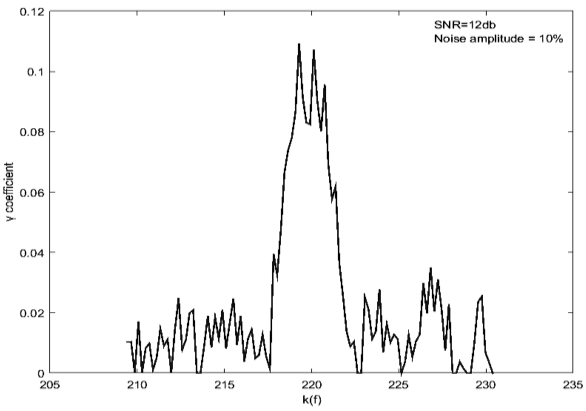

Fig. 9. γ(k) with SNR 12db inserts a noise amplitude 10% of $|\gamma(k)|$ max amplitude.

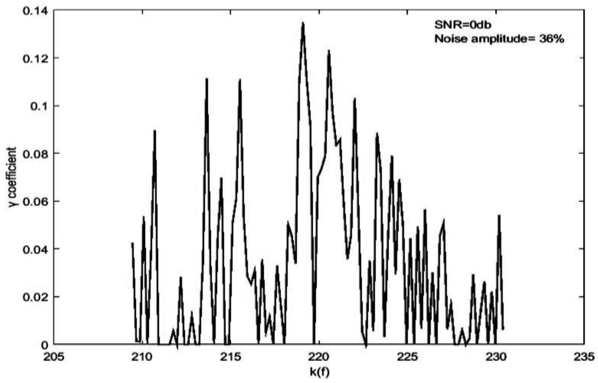

Fig. 10. γ(k) with SNR 0db inserts a noise amplitude 36% of $|\gamma(k)|$ max amplitude.

On the contrary a signal *γ(k)* exhibiting low *SNR*=0db (signal=noise), as demonstrated in figure 10, can totally suppress sidelobes and cancel our proposed method, if no additional noise suppression technique is applied.

Further to the above, there are several techniques that can be used to improve *SNR* and make our method useful for lower *SNR* values. Choosing the appropriate technique depends on what kind of noise interferes with the signal. In case of AWGN, it is possible to enhance the *SNR* by averaging measurements. Theory suggests that the noise goes down about as the square root of the number of averaged samples. Here we propose averaging over *N* successive bursts.

In figure 11 we obtain the improvement of figure 9 after an averaging of 25 samples (*N*=25 bursts). In figure 12 we obtain the improvement of figure 10 after averaging of 100 samples.

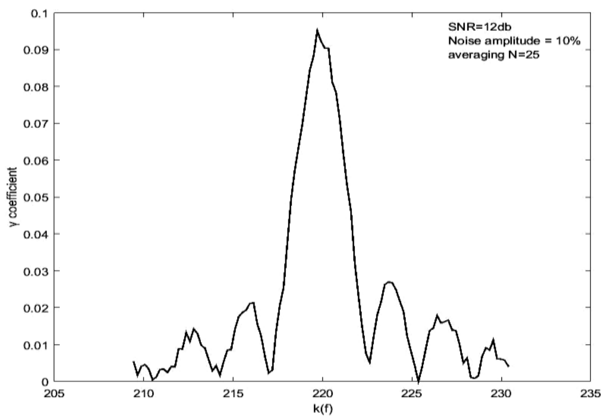

Fig. 11. γ(k) with SNR 12db after N=25 bursts averaging

It is obvious that the number *N* of bursts that are needed for having a useful signal of *γ(k)* depends on the *SNR* value, namely noise level. The only trade-off is that when number of *N* is increased, it is possible the target (e.g. sea surface) to look as a 'different target' during successive bursts. So the number of bursts is only limited by the rate of change of the target geometry.

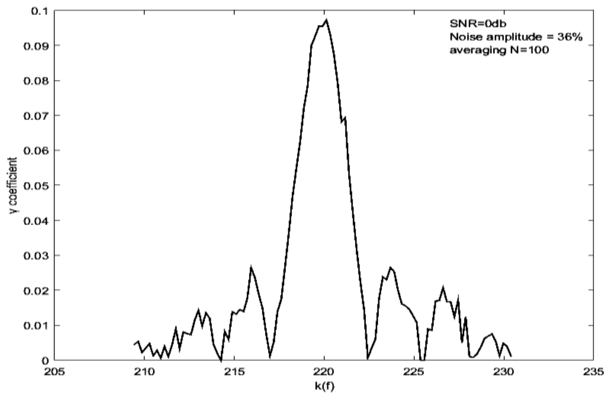

Fig. 12. γ-signal with SNR 0db after N=100 bursts averaging

4. CONCLUSION

In this paper, a novel method is presented for the characterization of rough fractal surfaces from backscattered radar data of *sufficient bandwidth* [9], [10]. As resulted from the plots of the backscattered signal magnitude as a function of the wavenumber (frequency, therefore a '*spectral method*') of the incident EM wave, as the roughness of the fractal surface increases, then the observed slope between the main lobe and the side lobes also increases. Moreover, the fractal dimension of the surface can be estimated by the average slope of backscattering coefficient |*γ*(*k*)|. Furthermore, the value of the available radar bandwidth is crucial and must be sufficiently large, for correct rough surface characterization. Finally, we prove that our method is useful even in a noisy radar environment which exhibits *γ(k)* with relatively low *SNR*. It is only a matter of selecting the appropriate averaging number of bursts in order to enhance *SNR* of signal *γ(k)*.

ACKNOWLEDGMENTS

The authors would like to express their sincere thanks to Prof. N. Ampilova and Prof. I. Soloviev, Faculty of Mathematics and Mechanics, St. Petersburg State University, Russia, for interesting discussions and suggestions of theirs, which stimulated this research at the various stages of its implementation.

References

[1] D. L. Jaggard, X. Sun, "Scattering from fractally corrugated surfaces", Journal of the Optical society of America A, Vol. 7, No 6, pp. 1131-1139, 1990.

[2] P. Beckmann, A. Spizzichino, The Scattering of electromagnetic waves from rough surfaces, Artech House Inc., 1987.

[3] D. L. Jaggard, A.D. Jaggard, P. Frangos, "Fractal electrodynamics: surfaces and superlattices", in Frontiers in Electromagnetics, Edited by Douglas Werner and Raj Mittra, IEEE Press, 2000, pp. 1-47.

[4] F. Berizzi, E. Dalle Mese, G. Pinelli, "One dimensional fractal model of the sea surface", IEEE Proc. Radar Sonar Navig., Vol. 146, No 1, pp. 55-64, 1999.

[5] A. K. Sultan – Salem, G.L. Tyler, "Validity of the Kirchhoff approximation for electromagnetic wave scattering from fractal surfaces", IEEE Trans. Geosc. Rem. Sensing, Vol. 42, No. 9, pp. 1860-1870, 2004.

[6] M. F. Chen, A. K. Fung, "A numerical study of the regions of validity of the Kirchhoff and small perturbation rough surface scattering models", Radio Science, Vol. 23, pp. 163 – 170, 1988.

[7] E. Jakeman, "Scattering by fractals", in Fractals in Physics, pp. 55-60, 1986.

[8] N. Ampilova and I. Soloviev, "On digital image segmentation based on fractal and multifractal methods", CEMA'15 Conference Proceedings, pp. 14-17, Sofia, Bulgaria, 2015.

[9] A. Malamou, A. Karakasiliotis, E. Kallitsis, G. Boultadakis, P. Frangos, 'Application of a fully automatic autofocusing algorithm for post – processing of synthetic aperture radar images based on image entropy minimization', Electronics and Electrical Engineering Journal, Vol. 19, No. 6, pp. 95 – 98, 2013.

[10] A. Malamou, C. Pandis, P. Frangos, P. Stefaneas, A. Karakasiliotis, D. Kodokostas, "Application of the modified fractal signature method for terrain classification from synthetic aperture radar images", Electronics and Electrical Engineering Journal, Vol. 20, No. 6, pp. 118–121, 2014.

[11] S. Savaidis, P. Frangos, D. L. Jaggard and K. Hizanidis, "Scattering from fractally corrugated surfaces : an exact approach", Optics Letters, Vol. 20, No. 23, pp. 2357-2359, 1995.

[12] S. Savaidis, P. Frangos, D. L. Jaggard and K. Hizanidis, "Scattering from fractally corrugated surfaces using the extended boundary condition method", Journal of the Optical Society of America *A*, Vol. 14, No. 2, pp. 475-485, 1997.

[13] D. L. Jaggard, X. Sun, "Fractal surface scattering: a generalized Rayleigh solution", Journal of Applied Physics, Vol. 68, No 11, pp. 5456-5462, 1990.

[14] M. F. Chen, A. K. Fung, "A numerical study of the regions of validity of the Kirchhoff and small-perturbation rough surface scattering models", Radio Science, Vol. 23, pp. 163-170, 1988.

[15] E. I. Thorsos, "The validity of the Kirchhoff approximation for rough surface scattering using a Gaussian roughness spectrum", Journal of Acoustical Society of America, Vol. 83, No 11, pp. 78-92, 1988.

[16] J. M. Soto-Crespo, M. Nieto-Vesperinas, "Electromagnetic scattering from very rough random surfaces and deep reflection gratings", Journal of the Optical Society of America A, Vol. 6, pp. 367-384, 1989.

[17] D. L. Jaggard, Y. Kim, "Diffraction by bandlimited fractal screens", Journal of the Optical Society of America A, Vol. 4, pp. 1055-1062, 1987.

[18] J. Fikioris, Introduction to Antenna Theory and Propagation of Electromagnetic Waves, pp. 155-156, National Technical University of Athens (NTUA), Athens, Greece, 1982.

[19] A. Kotopoulis, A. Malamou, G. Pouraimis, E. Kallitsis and P. Frangos, "Characterization of rough fractal surfaces from backscattered radar data", 'Electronics and Electrical Engineering' Journal, accepted April 2016.

THE RADIATION PROBLEM FROM A VERTICAL SHORT DIPOLE ANTENNA ABOVE FLAT AND LOSSY GROUND: VALIDATION OF NOVEL SPECTRAL DOMAIN ANALYTIC SOLUTION IN THE HIGH FREQUENCY REGIME AND COMPARISON TO EMPIRICAL TERRAIN PROPAGATION MODELS

G. Bebrov[1], S.Bourgiotis[1], A. Chrysostomou[1], S. Sautbekov[2] and P. Frangos[1]

[1]National Technical University of Athens
9, Iroon Polytechniou Str., 157 73, Zografou, Athens, Greece
Tel. +30 210 772 3694, Fax. +30 210 772 2281, E-mail: pfrangos@central.ntua.gr

[2]Eurasian National University 5, Munaitpassov Str., Astana, Kazakshtan,
E-mail : sautbek@mail.ru

Abstract

In this paper the results of a recently introduced novel solution to the well-known 'Sommerfeld radiation problem', are compared to those obtained through the classical Sommerfeld formulation. The method is novel in that it is entirely performed in the frequency domain, yielding simple integral expressions for the received Electromagnetic (EM) field and also in that they can end up into closed-form analytic formulas applicable to high frequencies. In this paper we compare our analytical results with existing numerical calculations found in the literature, based on the Sommerfeld formulation. The above comparison shows good agreement in the corresponding numerical results. Furthermore, a comparison of the method to the well-known Okumura-Hata empirical model is performed in an attempt to roughly estimate the extent to which the proposed model is suitable for real–environment EM field calculations.

1. INTRODUCTION

The 'Sommerfeld radiation problem' is a well-known problem in the area of propagation of electromagnetic (EM) waves above flat and lossy ground [1]. The original Sommerfeld solution to this problem is provided in the physical space by using the 'Hertz potentials' and it does not end up with closed- form analytical solutions.

In [2], the authors considered the problem from a spectral domain perspective, which led to relatively simple 1-D integral representations for the received EM field. Then with the use of the Stationary Phase Method (SPM, [2]) novel, closed-form analytic formulas were derived, applicable in the high frequency regime.

The comparison between the analytical expressions of [2] and their integral counterparts was performed in [3] where the requirements for the applicability of the SPM method were extracted. However, as mentioned there, due to the peculiarities of the integrands, which possess particular singularities, the integral expressions of [2] are not easily evaluated using standard numerical integration techniques, as for example the adaptive Simpson's method used in [3]. As a result, a confirmation of the results by using alternative integral evaluation techniques is justified. In this work, the results for the received EM field, taken via the application of the previously mentioned SPM method are juxtaposed against the ones available in a related research work [4]. The latter are obtained via 'a claimed to be accurate' evaluation of the original Sommerfeld integrals using commercially available simulation software, namely AWAS [4].

The last part of this work is devoted to comparing the above mentioned SPM-based analytical expressions to a well–known empirical model for path loss prediction, particularly Okumura- Hata [5]. This, as well as similar comparisons to be performed in the future, will eventually determine the extent to which the easily implemented model of [2] can be used for radio wave prediction in real life scenarios.

2. PROBLEM GEOMETRY

The problem geometry is shown in Fig. 1. A vertical Hertzian Dipole (HD), of dipole moment p, directed to the positive x axis, at altitude x_0 above infinite, flat, lossy ground radiates time-harmonic electromagnetic (EM) waves at angular frequency $\omega=2\pi f$ ($e^{-i\omega t}$ time dependence is assumed). The relative complex permittivity of the ground is $\varepsilon_r' = \varepsilon'/\varepsilon_0 = \varepsilon_r + i\sigma/\omega\varepsilon_0$, σ being the ground conductivity, f the carrier frequency and ε_0 = 8,854x10^{-12} F/m the absolute permittivity in vacuum or air. The wavenumbers of propagation are:

$$k_{01} = \omega/c_1 = \omega\sqrt{\varepsilon_1\mu_1} = \omega\sqrt{\varepsilon_0\mu_0} \tag{1}$$

$$k_{02} = \omega/c_2 = \omega\sqrt{\varepsilon_2'\mu_2} = k_{01}\sqrt{\varepsilon_r + i(\sigma/\omega\varepsilon_0)} \tag{2}$$

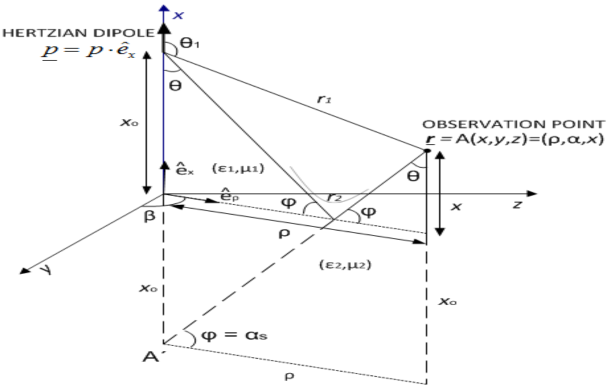

Figure 1. Geometry of the problem

In Fig. 1, point A΄ is the image of the HD with respect to the ground, r_1 is the distance between the source and the observation point (OP), r_2=(A΄A) the distance between the image and the OP, θ the 'angle of incidence' at the so–called 'specular point' and φ=π/2–θ the so–called 'grazing angle'.

3. INTEGRAL SPECTRAL DOMAIN REPRESENTATIONS FOR THE RECEIVED ELECTRIC FIELD AND ANALYTIC EXPRESSIONS IN THE HIGH FREQUENCY REGIME

In [2] it is shown that the electric field at the receiver's position above the ground level (x>0) can be expressed with the following integral formula ($\underline{E}^{LOS}$ denotes the direct field):

$$\underline{E}(\underline{r}) = \underline{E}^{LOS}(\underline{r}) - \frac{ip}{8\pi\varepsilon_{r1}\varepsilon_0}\times$$

$$\times\left\{\hat{e}_\rho\int_{-\infty}^{\infty} k_\rho^2\,\frac{\varepsilon_{r2}'\kappa_1-\varepsilon_{r1}\kappa_2}{\varepsilon_{r2}'\kappa_1+\varepsilon_{r1}\kappa_2}\,e^{i\kappa_1(x+x_0)}\cdot H_0^{(1)}(k_\rho\rho)\,dk_\rho\,-\right.$$

$$\left.-\hat{e}_x\int_{-\infty}^{\infty} k_\rho^3\,\frac{\varepsilon_{r2}'\kappa_1-\varepsilon_{r1}\kappa_2}{\kappa_1(\varepsilon_{r2}'\kappa_1+\varepsilon_{r1}\kappa_2)}\,e^{i\kappa_1(x+x_0)}\cdot H_0^{(1)}(k_\rho\rho)\,dk_\rho\right\} \tag{3}$$

where:

$$\kappa_1 = \sqrt{k_{01}^2 - k_\rho^2}\,,\ \kappa_2 = \sqrt{k_{02}^2 - k_\rho^2} \tag{4}$$

and $H_0^{(1)}$ is the Hankel function of first kind and zero order. Application of the 'Stationary Phase Method' (SPM) to (3), leads to the following analytic expressions for the electric field vector scattered from the plane ground, in the far field region and in the high frequency regime (for x>0) [3]:

$$\underline{E}_{x>0}^{SC} = \frac{pk_{01}\cos\varphi}{4\pi\varepsilon_0\varepsilon_{r1}(\mathrm{A'A})}\cdot\frac{\varepsilon_{r2}'\kappa_{1s}-\varepsilon_{r1}\kappa_{2s}}{\varepsilon_{r2}'\kappa_{1s}+\varepsilon_{r1}\kappa_{2s}}\cdot$$

$$\cdot e^{ik_{\rho s}\rho}\cdot e^{i\kappa_{1s}(x+x_0)}\cdot(-\kappa_{1s}\hat{e}_\rho + k_{\rho s}\hat{e}_x) \tag{5}$$

where,

$$k_{\rho s} = \frac{k_{01}\,\rho}{\sqrt{(x+x_0)^2+\rho^2}} = k_{01}\cos\varphi \tag{6}$$

$$\kappa_{1s} = \sqrt{k_{01}^2 - k_{\rho s}^2} = k_{01}\sin\varphi\,,\ \kappa_{2s} = \sqrt{k_{02}^2 - k_{\rho s}^2} \tag{7}$$

with $k_{\rho s}$ being the stationary point obtained from the SPM method [2].

4. COMPARISONS WITH EXISTING MODELS – NUMERICAL RESULTS

In this section various illustrations are presented, comparing the model of Section 3 with (i) the accurate Sommerfeld formulation, employed in related research work [4] and (ii) Okumura – Hata empirical model for path loss prediction [5].

4.1. Comparison with Sommerfeld formulation

Fig. 2 depicts the vertical component of the total received electric field, E_x, due to the radiation of a half wavelength, vertical dipole antenna above flat, lossy ground. The various plots refer to different transmitter heights. The set of the simulation parameters used for the production of these plots are shown in Table 1:

Table 1. Simulation parameters

Symbol	Description	Value
f	Operating frequency	1GHz
x_0	Height of transmitting dipole	5m, 10m, 20m 100m, 500 m
x	Height of observation point	2m
j	Distance range	1m – 50km
P	Radiated Power[1]	150W
$2h$	Length of the dipole antenna	λ/2
ε_r	Relative dielectric constant of ground (typical urban ground)	4.0
σ	ground conductivity	0.0002 S/m

[1] Used only in the simulated scenario of Section 3. The respective value used in [4] is not mentioned

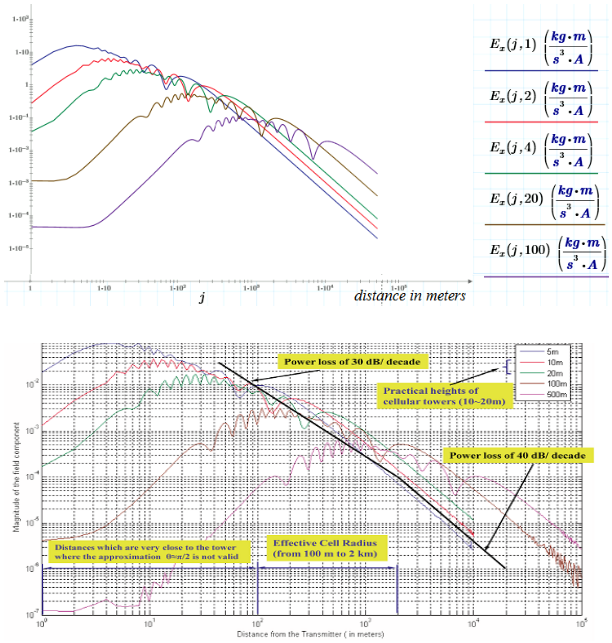

Figure 2. Variation of the magnitude of the E_x component (μV/m), for various transmitting antenna heights

The top plot of Fig. 2 refers to the field values according to the analytical expressions (5) – (7), whereas the bottom one are the respective results obtained after accurately evaluating the 'Sommerfeld integrals' for the total received EM field, [4].

Evidently, the results are in very good agreement. The SPM–based analytical method of Section 3 predicts the theoretical field behavior and this is true both for the near field as well as the far field region, as they are defined in [4]. In this regard, the so-claimed in [3], 'high frequency regime analytical method' of [2], is validated for such high frequencies as 1GHz.

As another validation of the previous arguments, Fig. 3 depicts the behavior of the electric field, for various scenarios regarding the electrical parameters of the ground, according to Table 2:

Table 2. Simulation parameters

Parameter	Value	
Operating frequency	900MHz	
Height of transmitting dipole	5m	
Height of observation point	2m	
Distance range	1m – 50km	
Radiated Power[1]	150 W	
Length of the dipole antenna	λ/2	
Ground Parameters	ε_r	σ (S/m)
Poor urban ground	4	0.001
Average ground	15	0.005
Good ground	25	0.02
Fresh water	81	0.01
Sea water	81	5.0
[1] Used only in the simulated scenario of Section 3.		

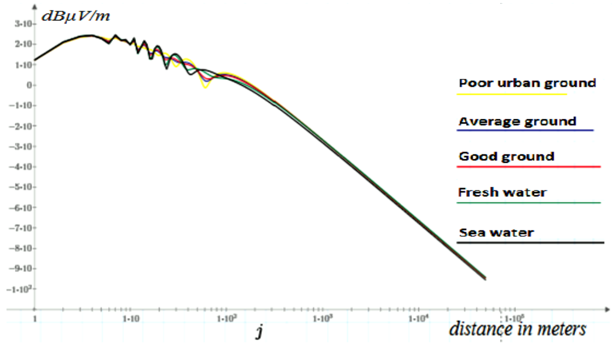

Figure 3. Variation of the magnitude of the E_x component (dBμV/m) for various types of ground

The field behavior shown in Fig. 3 is almost identical to that presented in Fig. 7 of [4], which is the equivalent case to the scenario considered here. In other words, the analytic expressions (5) – (7) validate the important finding of [4] (reached by numerical evaluation of the 'Sommerfeld integrals'), namely the fact that the type of the ground does not influence significantly the received EM field values.

4.2. Comparison with Okumura Hata empirical model

A preliminary check of the model proposed hereby against the well- known Okumura – Hata (OH) empirical model [5], commonly used for predicting signal loss in land mobile radio services, is carried out. Fig. 4 below illustrates the comparison.

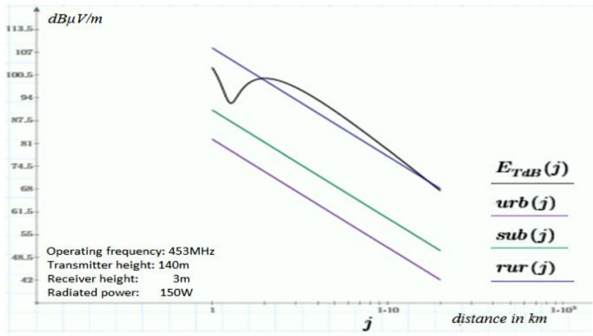

Figure 4. Comparison with OH model for urban (urb), suburban (sub) and rural (rur) environment

From Fig.4 it is evident that the proposed model exhibits similar behavior to the Okumura-Hata model for the case of an open (rural) area. On the contrary, there is an appreciable mismatch between them when applied to urban or suburban environments. A correction factor to accommodate for the specifics of the propagation environment (i.e. the presence of buildings, foliage, obstacles etc – typical to urban/suburban environment) is required and will be the subject of future research.

5. CONCLUSION-FUTURE RESEARCH

In this work, a comparison of a recently introduced solution to the 'Sommerfeld radiation problem in the spectral domain', against theoretical as well empirical approaches for the given problem is demonstrated. The proposed model leads to easily implemented analytical expressions for the received EM field and is proved to be valid in the high frequency regime.

Further validations against theoretically driven, numerical results like those of [4] used here, are required to determine the exact frequency limits of the analytic expressions (5) – (7). For this the perspective described in [3], which is believed to reduce the precision errors appeared there, will be followed, leading to a novel spectral domain representation for the surface wave as well [note that (5) neglects the role of the surface wave].

Finally, an attempt to determine the necessary corrections that will extend the model's applicability to more complex environments is also planned. Such checks will eventually determine the adoptions necessary for turning the novel propagation model of [2] to a robust prediction tool appropriate for radio planning purposes.

References

[1] N. Sommerfeld, "Propagation of Waves in Wireless Telegraphy", Ann. Phys., 28, pp. 665–736, March 1909; and 81, pp. 1135–1153, December 1926.

[2] K. Ioannidi, Ch. Christakis, S. Sautbekov, P. Frangos and S.K. Atanov, "The radiation problem from a vertical Hertzian dipole antenna above flat and lossy ground: novel formulation in the spectral domain with closed-form analytical solution in the high frequency regime", International Journal Antennas and Propagation, Hindawi Ed. Co., Special Issue 'Propagation of electromagnetic (EM) waves over terrain' (PEWT), vol. 2014.

[3] Chrysostomou, S. Bourgiotis, S. Sautbekov, K. Ioannidi and P. Frangos ,"Radiation of a Vertical Dipole Antenna over Flat and Lossy Ground: Accurate Electromagnetic Field Calculation using the Spectral Domain Approach along with Redefined Integral Representations and corresponding Novel Analytical Solution", Electronics and Electrical Engineering Journal, Vol. 22, No. 2, 2016.

[4] T. K. Sarkar et. al., "Electromagnetic Macro Modelling of Propagation in Mobile Wireless Communication: Theory and Experiment", IEEE Antennas and Propagation Magazine, Vol. 54, No. 6, pp. 17–43, Dec. 2012.

[5] Hata, Masaharu, "Empirical formula for propagation loss in land mobile radio services," IEEE Transactions on Vehicular Technology, Vol.VT-29, No.3, pp.317 – 325, August 1980.

IN SILICO SIMULATION OF GLIOBLASTOMA GROWTH AND INVASION INTO THE HUMAN BRAIN INCLUDING AN EXPLICIT MODELLING OF THE ADIABATIC BOUNDARY CONDITION IMPOSED BY THE SKULL

Stavroula G. Giatili and Georgios S. Stamatakos*

Institute of Communication and Computer Systems, National Technical University of Athens,
In Silico Oncology and In Silico Medicine Group,
9 Iroon Polytechniou, GR157 80, Zografos, Greece

giatili@mail.ntua.gr; * gestam@central.ntua.gr (corresponding author)

Abstract

The diffusive and infiltrative nature of glioma brain tumours and in particular glioblastoma constitutes a major barrier to their effective treatment. The present paper focuses on the numerical handling of a pertinent Neumann boundary value problem in the three-dimensional space acting as a tri-scale reaction – diffusion model of primary glioma growth and invasion into the surrounding normal brain. A complex anatomical and geometrical domain bounded by the skull is considered. The model takes into account the highly inhomogeneous nature of human brain. The generic finite difference – time domain (FDTD) method and more specifically the Crank – Nicolson technique in conjunction with the biconjugate gradient system solver have been utilized for the numerical solution of the problem. The model has been partly validated through comparing its predictions with real values of clinically pertinent macroscopic tumour characteristics. Numerical results are presented. They illustrate the potential of the model to support the clinician in designing the optimal individualized treatment scheme and/or schedule by using the patient's personal multiscale data and by experimenting in silico (=on the computer).

1. INTRODUCTION

Malignant gliomas, in general, and astrocytomas, in particular, account for approximately 50% of primary central nervous system (CNS) tumours in adults [1]. The median survival for glioblastoma multiforme (GBM) is 10-12 months. Because of the infiltrative nature of malignant gliomas [1,2], even a gross total resection is associated with tumour recurrence. In order to partly alleviate the corresponding complex treatment problem, cancer mathematical modelling [3] of diffusive tumour growth has been proposed and a number of models have been developed [2, 4].

The practical goal of this work, which can be viewed as a synthesis and an important extension of previous efforts [4], is to develop a "bottom-up" tri-scale diffusion-reaction based mathematical model of glioma growth and invasion that would serve as the core of the "Continuous Mathematics Based GBM Oncosimulator." [3].

For a biologically meaningful and computationally reliable diffusion-reaction based solution to the problem, consideration of the actual physical boundary of the cranium is important. An improper handling of the boundary conditions may lead to an unnatural behaviour of the simulated system and artificial loss of tumour cells. The model focuses primarily on the detailed numerical handling of the adiabatic Neumann boundary conditions imposed by the presence of the skull, considering the spatio-temporal characteristics of glioblastoma invasion.

2. THE TRI-SCALE REACTION – DIFFUSION MODEL

If Ω is the brain domain, GBM tumour growth and brain infiltration can be expressed by equation [5]:

$$\frac{\partial c(\vec{x},t)}{\partial t}=\nabla\cdot[D(\vec{x})\ \nabla c(\vec{x},t)]+\rho\ c(\vec{x},t)-G(t)c(\vec{x},t)\ \text{in}\Omega \quad (1)$$

where $\frac{\partial c(\vec{x},t)}{\partial t}$ denotes the rate of change of tumour cell concentration c at any spatial point $\vec{x}$ and time t, D denotes the diffusion coefficient and represents the active motility of tumour cells, $\rho\, c(\vec{x},t)$ expresses the net proliferation of tumour cells and $G(t)c(\vec{x},t)$ defines the loss of tumour cells due to treatment and also indirectly involves insufficient and inadequate angiogenesis.

The model takes into account the highly inhomogeneous nature of human brain. Two different approaches have been developed: the homogeneous and the inhomogeneous approach. In the inhomogenous approach, the structures of white matter, grey matter, cerebrospinal fluid (CSF) are taken into consideration and three values of the parameter *D* are considered: D_g, D_w and D_{CSF} if $(\vec{x})$ belongs to grey matter, white matter and CSF respectively. In the homogenous approach, where for simplification homogeneous brain tissue is considered, *D* has the same value all over the intracranial space.

Regarding the initial condition for the reaction–diffusion system, it is assumed that the initial spatial distribution of malignant cells is described by a known function $f(\vec{x})$.

In order to complete the model formulation, appropriate boundary conditions have to be added precluding migration beyond the skull boundary. Neumann boundary conditions, which correspond to no net flow of tumour cells out of or into the brain region across the brain-skull boundary, have been imposed.

In order to *numerically apply* the Neumann boundary condition, "fictitious nodes", $F_{i,j,k}$, have been used [6]. Their number is equal to the number of the adjacent nodes that belong to the cranium. An indicative case of numerically applying the boundary condition at the boundary point (x_i, y_j, z_k) in the negative z direction is the following:

$$-\left.\frac{\partial c}{\partial z}\right|_{(x_i,y_j,z_k)} = 0 \Rightarrow c_{i,j,k+1} = c_{F_{i,j,k-1}} \qquad (2)$$

An indicative equation at the boundary grid point (x_i, y_j, z_k) where skull tissue is found only in the negative x and the negative y direction by applying the Crank - Nicolson scheme is (3) for the homogeneous and (4) for the inhomogeneous approach respectively.

$$[1+6\lambda-\frac{\Delta t}{2}(\rho\text{-}G)]c_{i,j,k}^{t+1}-\lambda(2c_{i+1,j,k}^{t+1}+2c_{i,j+1,k}^{t+1}+c_{i,j,k+1}^{t+1}+c_{i,j,k-1}^{t+1})=$$
$$[1-6\lambda+\frac{\Delta t}{2}(\rho\text{-}G)]c_{i,j,k}^{t}+\lambda(2c_{i+1,j,k}^{t}+2c_{i,j+1,k}^{t}+c_{i,j,k+1}^{t}+c_{i,j,k-1}^{t})\quad(3)$$

$$\left[1+6\lambda_{i,j,k}-\frac{\Delta t}{2}(\rho\text{-}G)\right]c_{i,j,k}^{t+1}-2\lambda_{i,j,k}c_{i+1,j,k}^{t+1}-2\lambda_{i,j,k}c_{i,j+1,k}^{t+1}-$$
$$\left(\lambda_{i,j,k}+\frac{\lambda_{i,j,k+1}-\lambda_{i,j,k-1}}{4}\right)c_{i,j,k+1}^{t+1}-\left(\lambda_{i,j,k}-\frac{\lambda_{i,j,k+1}-\lambda_{i,j,k-1}}{4}\right)c_{i,j,k-1}^{t+1}=$$
$$\left[1-6\lambda_{i,j,k}+\frac{\Delta t}{2}(\rho\text{-}G)\right]c_{i,j,k}^{t}+2\lambda_{i,j,k}c_{i+1,j,k}^{t}+2\lambda_{i,j,k}c_{i,j+1,k}^{t}$$
$$+\left(\lambda_{i,j,k}+\frac{\lambda_{i,j,k+1}-\lambda_{i,j,k-1}}{4}\right)c_{i,j,k+1}^{t}+\left(\lambda_{i,j,k}-\frac{\lambda_{i,j,k+1}-\lambda_{i,j,k-1}}{4}\right)c_{i,j,k-1}^{t}\quad(4)$$

where $c_{i,j,k}^{t}$ is the finite difference approximation of c at the grid point (x_i y_j, z_k) at time t, Δt is the time step size for the time discretization, h is the space step size at each axis of the gridding scheme for the space discretization, $\lambda = D\Delta t\,/\,[2(h)^2]$ and $\lambda_{i,j,k} = D_{i,j,k}\Delta t\,/\,[2(h)^2]$.

The resulting system of equations may be written equivalently in the form $\overleftrightarrow{A}\vec{x} = \vec{b}$ where $\vec{x}$ denotes a vector that contains an approximation of the solution c at the mesh nodes at time t. Due to the high complexity of the biological system the BiConjugate Gradient method (BiCG) has been applied [6].

3. MODEL SIMULATIONS

Three-dimensional simulations of untreated glioma growth, assuming a complex anatomical and also geometrical domain bounded by the skull, have been performed. A three dimensional image of a typical real human head has been considered. The dataset used has been acquired from 3d Slicer which is a freely available application for image analysis and automatic segmentation of brain structures from MRI data. Two different scenarios have been executed and mutually compared; the homogeneous and the inhomogeneous scenarios. In the first case homogeneous brain tissue is considered. In the second case the structures of white matter, grey matter, CSF and skull have been segmented. Following the delineation of the skull boundary, a fictitious growing virtual spherical glioblastoma tumour of radius equal to 0.7 cm has been virtually placed inside the cranial cavity. It should be noted that glioblastoma diagnosis is possible when the volume of an enhanced CT-detectable tumour has reached a size equivalent to a sphere with an average 3 cm diameter [5].

The typical values of the parameters that have been used for the production of the results have been carefully selected from pertinent literature so as to best reflect aspects of glioblastoma dynamics. The net tumour growth rate ρ, which represents the net rate of tumour growth including tumour cell proliferation, loss and death has been set equal to 0.012 d^{-1} [5]. For the inhomogeneous scenario the value of the space dependent diffusion coefficient $D_{i,j,k}$, has been calculated as the average value of the growing diffusion coefficient and the migrating diffusion coefficient (D_g = 0.000102 cm²/d, D_w = 0.00051 cm²/d and D_{CSF} = 0.000001 cm²/d) [7].

The value of D for the homogeneous case has been estimated as the weighted average value of the diffusion coefficient for white matter, grey matter and CSF (D=0.00038$\mathrm{cm}^2/\mathrm{day}$). The concentration of tumour cells within the initial tumour has been arbitrarily assumed uniform and equal to 10^6 cells/mm^3 [8]. Diffusion phenomena before the time point corresponding to the start of the simulation have been ignored. Regarding the parameters associated to the numerical methods used, the time step Δt, the space step size h and the convergence tolerance for the bi-conjugate gradient method have been chosen equal to 0.5 d, 0.1 cm and 10^{-6} respectively. The virtual tumour grows for 180 days after the initialization time point. Figure 1 shows a virtual tumor on the first and the 180th simulated day for the inhomogeneous and homogeneous scenario. Figure 2 depicts tumour cell density for the inhomogeneous case. The simulated volume appears to meet the expected clinical macroscopic behaviour of glioblastoma. Moreover, the resulting virtual tumours proved the adiabatic behaviour of the skull without artificial cell loss in the skull-brain barrier. It is noted that the threshold of tumour detection has been set equal to 8000 tumour cells/mm^3 according to [5].

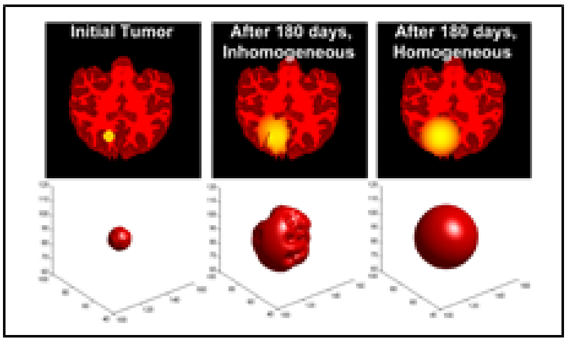

Figure 1. Coronal slice and a three dimensional snaphot of a virtual tumour for the inhomogeneous (second panel column) and homogeneous (third panel column) case after 180 simulated days. In the upper panels, the colour intensity level depends logarithmically on the tumour cell concentration.

The doubling time for gliomas, which is a classical metric of glioma growth quantification, ranges from 1 week to 12 months covering the range of high to low grade gliomas [9]. Predictions of the doubling time for both cases lie within published ranges. The typical value of 2 months is observed on the 33th simulated day. Following an *in silico* theoretical exploration indicates that even by using a pertinent homogeneous brain based model, a rough but nonetheless informative estimate of the expected tumour doubling time can be achieved.

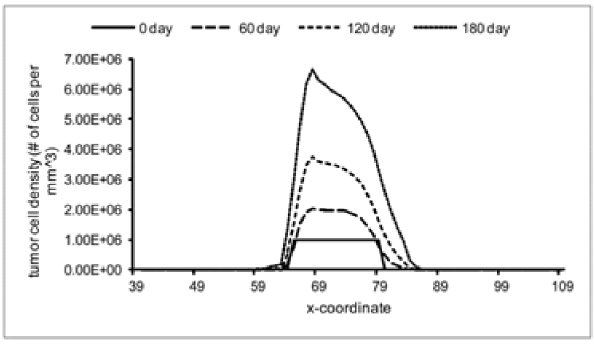

Figure 2. Tumour cell density along the x axis (the horizontal axis of the coronal plane) passing through the centre of the initial tumour for different simulated time points.

4. CONCLUSION

The major highlight of the paper is an explicit and thorough tri-scale numerical handling of the Neumann boundary value problem of GBM growth and invasion into the surrounding normal brain tissue in three dimensions. The heterogeneous nature of human brain and the complexity of skull geometry have been taken into consideration.

Comparison of the simulation predictions with clinical observational data has supported the reliability of the model. It has also illustrated the model's potential to be used as a basis for an individualized treatment planner through *in silico* experimentation by exploiting the patient's multiscale data. The presented model could serve as the main component of a continuous mathematics based GBM Oncosimulator.

Moreover, the study has established a generic methodology which could be translated into other mathematically similar phenomena of physics, chemistry biology and other domains. Further model development will also include explicit tumour response to treatment and an extensive clinical adaptation and validation of the extended model.

5. ACKNOWLEDGMENTS

This work has been supported in part by the European Commission in the framework the projects "p-Medicine: Personalized Medicine (FP7-ICT-2009.5.3-270089)", "CHIC: Computational Horizons in Cancer: Computational Horizons In Cancer: Developing Meta- and Hyper-Multiscale Models and Repositories for In Silico Oncology" (FP7-ICT-2011-9-600841), MyHealthAvatar (PI:600929) and DR THERAPAT (PI: 600852). The authors would like to thank Prof. Dr med N. Graf, Director of the Pediatric Oncology and Hematology Clinic, University Hospital of Saarland, Germany and Dimitra Dionysiou PhD, ICCS, NTUA, Greece for fruitful discussions

References

[1] C. A. Perez, L. W. Brady, Principles and Practice of Radiation Oncology, Lippincott-Raven, Philadelphia, 1997.

[2] J. D. Murray, Mathematical Biology II: Spatial Models and Biomedical Applications, Springer-Verlag, New York, USA, 2003.

[3] G. Stamatakos, D. Dionysiou, A. Lunzer, et al. "The Technologically Integrated Oncosimulator: Combining Multiscale Cancer Modeling with Information Technology in the In Silico Oncology Context", IEEE J. Biomed. Health Inform, 18, 2014, pp. 840-854.

[4] S. Giatili, G. Stamatakos, "A detailed numerical treatment of the boundary conditions imposed by the skull on a diffusion–reaction model of glioma tumor growth. Clinical validation aspects", Applied Mathematics and Computation, 218, 2012, 8779-8799.

[5] K. Swanson, E. Alvord, J. Murray, "Virtual brain tumors (gliomas) enhance the reality of medical imaging and highlight inadequacies of current therapy", Br J Cancer, 86, 2002,14 – 18.

[6] B. Bradie, A friendly Introduction to Numerical Analysis, Pearson International, USA, 2006.

[7] S. Eikenberry, T. Sankar, M. Preul, et al., "Virtual glioblastoma: growth, migration and treatment in a three-dimensional mathematical model", Cell Prolif., 42, 2009, 511-528.

[8] G. Steel, Basic Clinical Radiobiology, Arnold, London, UK, 2002.

[9] E. Alvord, C. Shaw, Neoplasm affecting the nervous system in the elderly. In: Duckett S, eds. The Pathology of the Aging Human Nervous System, Lea & Febiger, Philadelphia, 1991.

LASER-DIODE BASED PHOTOACOUSTIC SIGNAL EXCITATION FOR BIOMEDICAL APPLICATIONS

Viktor Stoev, Mityo Mitev, Ivo Iliev

Technical University of Sofia, Department of Electronics and Electronics Technologies,
Faculty of Electronic Engineering and Technologies, Sofia 1000, Bulgaria, 8 Kl. Ohridski Blvd.

E-mails: v.stoev@tu-sofia.bg, mitev@ecad.tu-sofia.bg, izi@tu-sofia.bg

Abstract

Recently, powerful pulsed laser diodes have attracted significant attention as a suitable means for the excitation of photoacoustic signals. Efficiently driving the laser diodes is the key to optimal photoacoustic signal generation. In this paper we propose a laser-diode based photoacoustic signal excitation system that relies on the peculiar phenomena of current mode second breakdown (commonly referred to as avalanche mode) intrinsic to bipolar junction transistors.

Starting from a single transistor driver capable of switching up to a few hundred mA in 30ns, we increase the switching capability by first stacking several transistors in a Marks-Bank design and considering a custom sandwich-like topology, which can hold up to eight identical single transistor drivers that are vertically stacked along the edge of a horizontal circular base, which holds the laser diode.

1. INTRODUCTION

The photoacoustic imaging (PAI) technique is swiftly maturing and is expected soon to be implemented in the clinical practice [1]. Usually Q-switched Nd:YAG pumped OPO, dye or Ti Sapphire laser systems are used for the efficient photoacoustic signal generation. However, they operate at low pulse repetition frequencies (PRF), may require cooling and have large dimensions, all of which is limiting their practical application in the clinical environment [2].

Powerful pulsed laser diodes (PLDs) provide only a few μJ of output energy [3], but can operate at much higher PRFs and have small dimension, which turns them into an attractive alternative to the more powerful, but bulky systems.

PLDs require tens of amperes of forward current crammed in a few hundred nanoseconds with short rise/fall times in order to generate an optimal photon flux [4]. To achieve this, different strategies can be applied, among which are the use of high–power field effect transistors, high–speed silicon controlled rectifiers, step recovery diodes and others [5]. An interesting alternative to these is the use of avalanche mode (current mode second breakdown) transistors, which besides being relatively cheap offer somewhat easily adjustable, variable length and amplitude output signals. Moreover, by using a Marks-bank configuration very high current switching can be achieved. In order to meet the stress confinement rule, intrinsic to the efficient photoacoustic signal generation [6], all transistors must breakdown simultaneously. To achieve this goal a sandwich topology is proposed, which guarantees that the signal paths from the transistor emitters to the laser diode will have the same length and thus induce the same delay.

2. THE SINGLE TRANSISTOR DRIVER

The basic laser diode driver block is depicted in Figure 1. It consists of a differentiator input circuit (C_1-R_1), an energy storage element (capacitor C_2) and a few resistors limiting the currents and setting the transistor in the desired mode.

2.1. Circuit design

To enter breakdown, large supply voltage must be applied between the transistor's reverse biased collector-base p-n junction. This increases the energy of the free charge carriers diffusing through the junction, with some gaining enough energy to release a new electron-hole pair upon collision with atoms from the crystal lattice. Typically this happens around BV_{CBO}, where the current flowing through the collector p-n junction increases above a threshold value after which the avalanche process can sustain itself. By adding the energy storage capacitor C_2 and keeping resistance R_4 small the current through the collector junction is kept large enough for avalanche breakdown to occur [7]. The avalanche process duration can be roughly defined as $\tau_d = C_2(R_4 + R_{LD1})$ and will seize once the current through the collector junction drops below the threshold level.

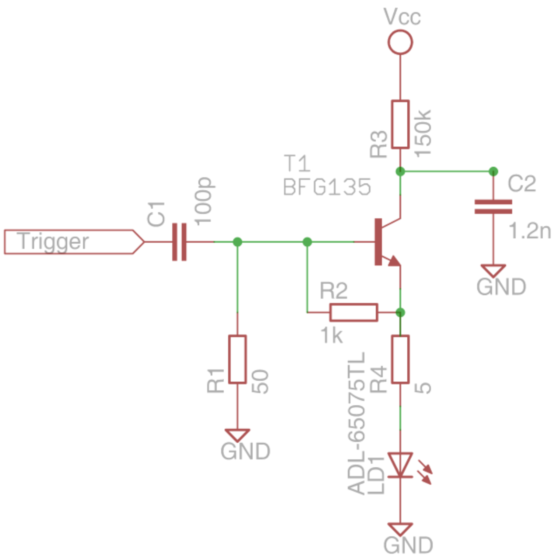

Figure 1. The laser driver circuit using BFG135 in avalanche mode and exciting a laser diode

The signal amplitude depends on the characteristics of capacitor C_2, the supply voltage V_{cc} and resistance R_4. Increasing V_{cc} has a limited effect on the current flowing through LD_1, while increasing C_2 and decreasing R_4 modifies tremendously the signal amplitude and duration. Basically, smaller capacitance leads to smaller amplitude, but fast rise/fall times of the output signal, while smaller R_4 increases the current flowing through the laser diode. Finding the balance between the two requires some empirical work the result of which is the circuit depicted in Figure 1.

Another major pillar in the design is the choice of the transistor. Special avalanche transistors are available (such as ZETEX's ZTX415 [8]), but it is well known that almost any NPN bipolar junction transistor can be used in avalanche mode [9]. In the current design NXP's BFG135 is implemented, which besides being wideband benefits from low BV_{CBO}. Actually, stable breakdown occurs at V_{cc} = 40V, which facilitates the design of the circuit and imposes significantly lower power supply requirements than those needed by 2N2369, ZTX415 and other.

2.2. Experimental results

Avalanche breakdown takes place when 5V, 200ns square pulses are applied to the base of BFG135 with a PRF of 1 kHz. The typical output (taken from R_4) and collector voltage are depicted in Figure 2.

The collector voltage reveals the process of charge and discharge of the energy storage capacitor C_2. Initially, it is fully charged through resistor R_3 and when the base-emitter junction forward biases, it discharges through the transistor driving the laser diode. The process is very fast with rise time in the order of 6ns and total duration of the semi-Gaussian part of the signal of approximately 30ns.

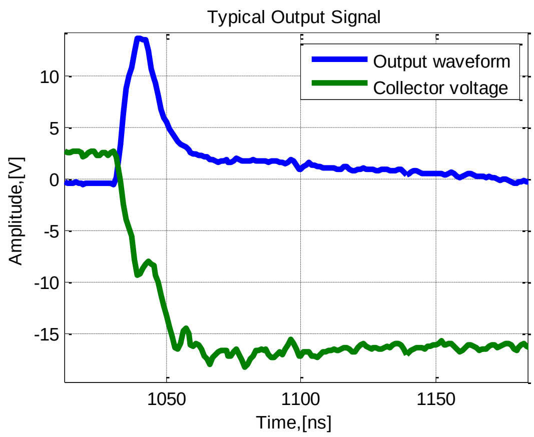

Figure 2. Emitter (top) and collector voltage (bottom) for the driver solution of Figure 1

However, the rear edge is typically less steep than its leading counterpart and contains a slowly decaying part that stretches for hundreds of nanoseconds. This is the result of parasitic inductances and capacitances that reside in the LD and the traces. These are actually a major concern when considering Marks-bank designs as will become clear shortly.

To explore the driver capabilities for laser diode stimulation, Laser Component's ADL-65075TL (continuous mode laser, 14mW, 650nm) was tested with the proposed circuit. The emitter photon flux was captured via a PIN photodiode and the corresponding voltage waveform was taken from a 50Ohm resistor connected in parallel to the photodiode terminals. The waveform is depicted in Figure 3.

Notice that the signal resembles strongly the output voltage presented in Figure 2. However, it has both fast leading and falling edges, which indicates that the laser diode is emitting light only during the semi-Gaussian part of output signal. A peculiar effect of the parasitic inductances is the negative voltage observed in Figure 3 following the Gaussian signal. Depending on the used resistor this effect can be augmented or reduced significantly.

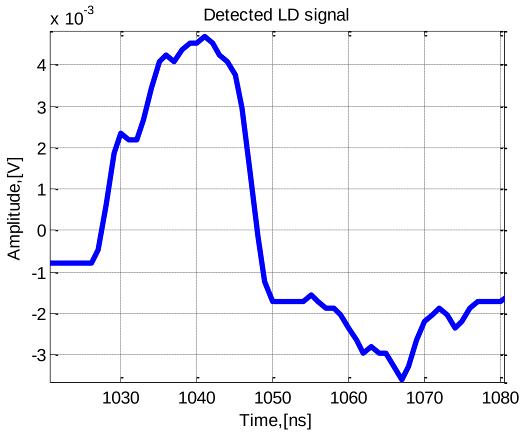

Figure 3. Measured laser diode signal with a PIN photodiode

3. THE MARKS-BANK DESIGN

Avalanche transistors are often combined in Marks-Bank designs [7,11], since powerful PLDs may require tens of amperes of forward current for optimal operation [10]. Here a similar approach is followed through a combination of several single transistor drivers.

3.1. The parallel stack

Initially a parallel configuration was studied consisting of three single transistor drivers, with the supply voltage and input pulses kept the same as before. To achieve better stability a modification with respect to the standard circuit is made as resistors are connected to each of the transistor emitters. The modified circuit is depicted in Figure 4.

The waveform depicted in Figure 5 is the output voltage drop across the laser diode. Notice that there are three distinct peaks accounting for the avalanche process occurring in each transistor. Considering that a 1cm trace on a 0.8 mm thick FR4 substrate introduces a delay of about 70ps and that positioning three identical avalanche transistor drivers on a 2D plane is hardly possible, this result is not surprising. As a result the breakdown process occurs at a slightly different moment of time with the amplitude never reaching a peak and stretching the signal length. It is not hard to imagine that the problem will worsen with the increase of the transistor count.

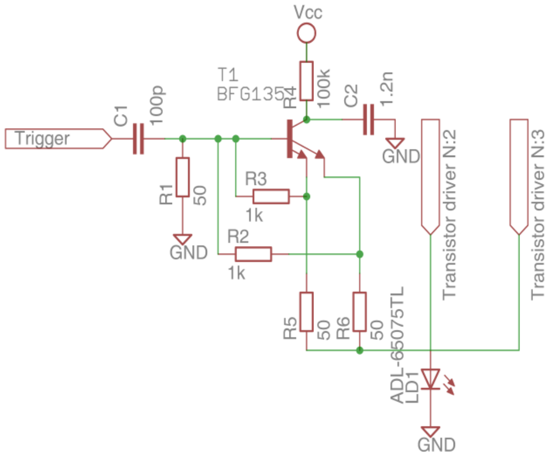

Figure 4. The parallel stack topology

3.2. The sandwich topology

To overcome the difficulty of trace length differences the Marks-Bank driver can be laid outs as a three part sandwich structure – a bottom PCB, holding the laser diode and the emitter resistors, up to eight identical vertically mounted PCBs (each of which represents a single transistor driver) and a closing top PCB that supplies the power and trigger pulses. Integrating the three parts can produce a compact laser diode driver and initial study of the structure shows good driving capabilities.

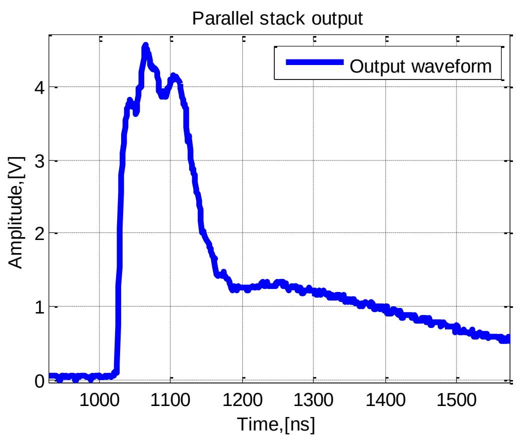

Figure 5. Output waveform of the parallel stack

4. CONCLUSION

Avalanche transistors are an interesting and promising alternative to laser diode excitation. A single transistor driver is shown to be capable of switching up to several hundreds of mA in 30ns. By changing the energy storage capacitor value the current switching capabilities can be easily modified, as well as the output signal length. The single transistor driver serves as the building block for the more powerful Marks-Bank driver which when constructed by three separate identical single transistor drivers was found to be capable of generating relatively strong output signals across the laser diode. However, it suffers from synchronization issues, due to differences in signal paths, which led to the consideration of a custom topology for the driver where the introduced delay is identical for each single transistor block. It is through this design that high current switching can be achieved and efficient photoacoustic signal generation can be made possible.

5. ACKNOWLEDGMENTS

This work is supported under project grant N: 152ПД0049-03 by the Technical University of Sofia.

References

[1] Paul Beard. Biomedical photoacoustic imaging. Interface Focus, 1(4):602–631, 2011.

[2] T. J. Allen and P C Beard. "Dual wavelength laser diode excitation source for 2D photoacoustic imaging". In Biomedical Optics (BiOS) 2007, pages 64371U–64371U. International Society for Optics and Photonics, 2007.

[3] Bell, M.A., Boctor, E., Guo, X., & Kang, H.J. "Improved Contrast in Laser-diode-based Photoacoustic Images with Short-lag Spatial Coherence Beamforming". IEEE International Ultrasonics Symposium Proceedings, 2014

[4] Allen, TJ, and Beard, PC (2006): Pulsed NIR laser diode excitation system for biomedical photoacoustic imaging, Optics Letters 31(23), 3462 - 3464

[5] Qing WANG, Xiao-Jian TIAN, Ge WU, Ming-yuan LUO, "Design of high-peak current and narrow pulse driver of laser diode", The Journal of China Universities of Posts and Telecommunications, Volume 16, Supplement 1, September 2009, Pages 82-85

[6] Minghua Xu and Lihong V. Wang. "Photoacoustic imaging in biomedicine". Review of Scientific Instruments, 77(4):041101+, 2006.

[7] R. J. Baker, "High voltage pulse generation using current mode second breakdown in a bipolar junction transistor", Review of Scientific Instruments, 62, 1031-1036 (1991)

[8] Zetex, "The ZTX415 Avalanche Mode Transistor", Application Note 8, Issue 2, January 1996

[9] Jim Williams, "High Speed Amplifier Technology", AN47, Linear Technology, 1991

[10] High Power Pulsed Laser Diodes –905D3J09 series, Laser components

[11] Guang-You Fang, Bin Zhou, Yi-Cai Ji and more "Lunar Penetrating Radar onboard the Chang'e-3 mission", Research in Astronomy and Astrophysics, 14, 2014.

KIDNEY SEGMENTATION IN ULTRASOUND IMAGES VIA ACTIVE CONTOURS

Veska M. Georgieva

Technical University of Sofia, Faculty of Telecommunications, Technical University of Sofia, Bulgaria
1000 Sofia, "Kl. Ohridsky" str.8
T. (+359 2) 965-3293; E-mail: vesg@tu-sofia.bg

Stephan G. Vassilev

Technical University of Sofia, Faculty of German Engineering Education and Industrial Management,
1000 Sofia, "Kl. Ohridsky" str.8
E-mail: stephan.vassilev@gmail.com

Abstract

In this paper is presented an effective approach for kidney segmentation in 2D ultrasound (US) images.

In regard to different limitations of US images such as poor signal-to-noise ratio, signal drop-out, missing or misplaced boundaries of the objects, a preprocessing stage is proposed. It consists of contrast enhancement based on CLAHE and speckle noise reduction with modified homomorphic filter based on wavelet packet decomposition of the transformed US image. The method of segmentation is based on active contour without edges. It can detect objects whose boundaries are not necessarily defined by gradient.

Some experimental results are presented, obtained by computer simulation in the MATLAB environment. Implementation results are given to demonstrate the effectiveness of the proposed approach in clinical diagnostics.

1. INTRODUCTION

Kidney segmentation in US images is a particularly difficult task. The US images have a poor signal-to-noise ratio, signal drop-out, missing boundaries, misplaced boundaries and reconstruction errors [1]. The kidney is an elastic organ and can suffer large deformations. Furthermore, in US the interior of the organ exhibits heterogeneous structures with different intensities, and many of the boundaries are lost due to the density similarity to surrounding structures [2].

US segmentation methods have been previously classified according to the prior knowledge employed to improve the accuracy of results. These constraints include image-derived priors (intensity, intensity derivatives, local phase, texture), and application-derived priors (shape and motion) [1]. Some of the classified the methods in different categories based on the shape, region, if the segmentation is automatic or manual and finally combing some of the categories together [3]. In Fig. 1 is presented the classification of methods for kidney segmentation according to the above mentioned categories [4].

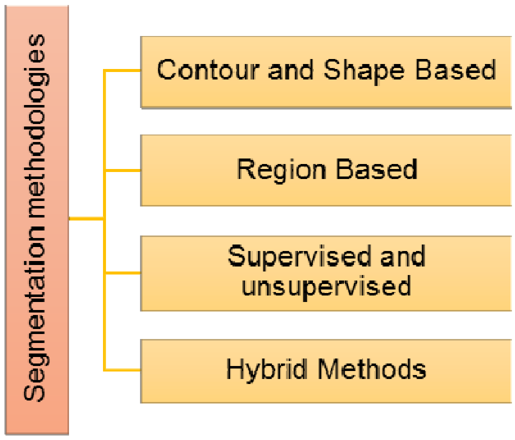

Figure 1. Classification of methods for kidney segmentation

The manually-selected elliptical approximations of the kidney region are usually provided in clinical practice [5]. However, the ellipse method is known to underestimate the kidney size up to a 25% error [6]. One of the best known and validated frameworks able to incorporate edges and shape priors is the active contour models []. The main idea behind this model is that the presence of an image feature depends not only on the value of the image at a given point in space or on its derivatives, but also on the spatial distribution of such features.

In this paper we propose an effective approach for kidney segmentation, which includes the preprocessing stage for enhancement of the US image, following by active contour segmentation based on active contour model of Chan and Vese [7]. Our goal was to implement this model and to investigate its advantage by application to US images in regard to their specific.

The paper is arranged as follows: In Section 2 is presented the main algorithm of processing; In Section 3 is presented the algorithm of kidney segmentation via active contour; in Section 4 are given some experimental results, obtained by computer simulation and their interpretation; in Section 5 - the Conclusion.

2. MAIN ALGORITHM OF PROCESSING

The flowchart of the main algorithm for US image processing is given in Fig. 2.

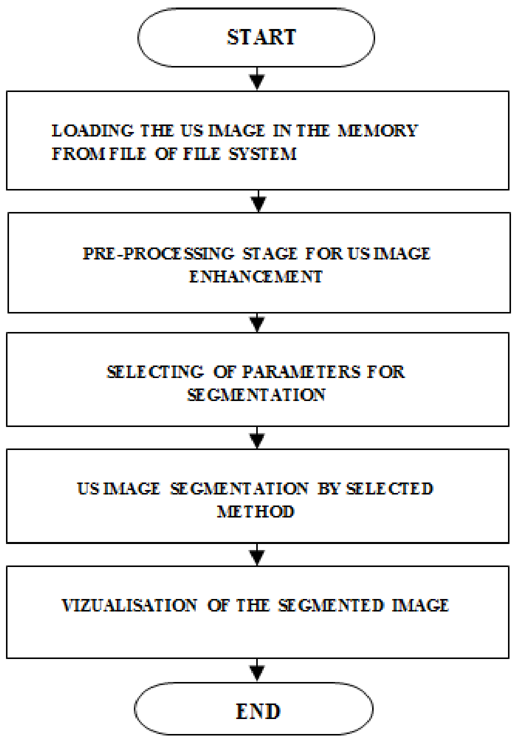

Figure 2. Flowchart of the maim algorithm

The pre-processing stage includes contrast enhancement based on CLAHE and speckle noise reduction. For modelling an image with speckle noise is used the generalized Gaussian distribution and generalized gamma distribution. For noise reduction is used modified homomorphic filter based on wavelet packet decomposition and adaptive threshold of the transformed US image [8].

The kidney segmentation is made by the implementation of the Chan and Vese active contour model. It is a special case of the Mumford–Shah problem [7]. The regularized Heaviside function H defines 2 different regions based on the level set function. The energy can be presented as a difference of the intensity function I from expected value c_1 and c_2, respectively. The Dirac function δ, which is the gradient of the Heaviside function, penalizes long boundaries between the regions. The minimization of the functional over region Ω optimizes this special case of the Mumford–Shah functional and is defined in (1):

$$E(\phi)=\int_\Omega a_1 H(\phi(x))[I(x)-c_1]+a_2[1-H(\phi(x))]\times [I(x)-c_2]+a_3\delta(\phi(x))dx \qquad (1)$$

The weights a_1, a_2 and a_3 depend on the importance and/or reliability of the three constraints. If the functional is convex (in case if the two intensities c_1 and c_2 are fixed and known), optimization can be done based on histogram of data values $I(x)$. In the other case, the segmentation will be dependent on the initial level set function. We have used that the initial 0-level set can be defined by the doctor.

The parameters which can be selected for segmentation are following:

- *mask* — Initial contour at which the evolution of the segmentation begins;
- *n — Maximum number of iterations* to perform in evolution of the segmentation;
- *Rad –Radius of the location in pixels;*
- *Alpha* – 'Smooth Factor' – Degree of smoothness or regularity of the boundaries of the segmented regions.

After choosing all input information the procedure of segmentation begins. Then the final result from segmentation is visualized – US image with segmented object.

3. ALGORITHM OF SEGMENTATION VIA ACTIVE CONTOUR

The flowchart of the presented algorithm is presented in Fig. 3.

To get faster and more accurate results we propose an initial contour position, which is close to the desired object boundaries to be selected interactively by the doctor.

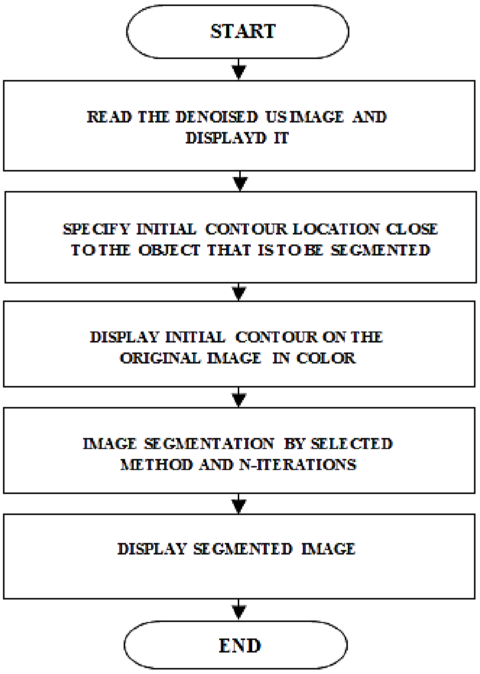

Figure 3. Flowchart of the algorithm for segmentation via active contour

If the initial contour position (specified by the region boundaries in mask) is far from the desired object boundaries, we propose to specify higher values of *n* in regard to achieve desired segmentation results. Higher values of *Alpha* produce smoother region boundaries but can also smooth out finer details. Lower values produce more irregularities (less smoothing) in the region boundaries but allow finer details to be captured.

4. EXPERIMENTAL RESULTS

The formulated stages of processing are realized by computer simulation in MATLAB 7.14 environment by using IMAGE PROCESSING and WAVELET TOOLBOXES [9]. In analysis are used 20 US images from kidney with size 640x480 pixels in jpg file format. For processing they are converted in bmp format.

Some results from simulation, which illustrate the working of proposed algorithm, are presented in the next figures below.

In Fig. 4 is shown the original US abdominal image of right kidney.

Fig. 5 illustrates the result from segmentation of the kidney. The segmentation is performing by *n=1000* iteration.

Figure 4. Original US image of right kidney

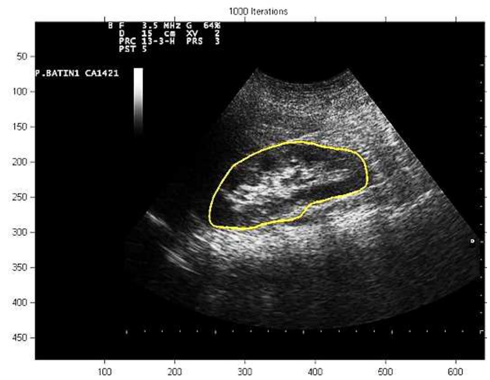

Figure 5. US image with segmented right kidney

For validation of the segmentation results, we compute the undirected partial Hausdorff distance [10] between the boundary of the computed segmentation and the boundary of the manually-segmented ground truth. The directed partial Hausdorff distance over two point sets *A* and *B* is defined in (2):

$$h_K = \underset{a \in A, b \in B}{K^{th}} \min \|a - b\| \qquad (2)$$

where *K* is a quantile of the maximum distance. The undirected partial Hausdorff distance is defined in (3):

$$H_K(A,B) = \max(h_K(A,B), h_K(B,A)) \qquad (3)$$

The obtained averaging results for the partial Hausdorff distance between automatic segmentation and the manually-segmented ground truth are given in Table 1.

Table1. Partial Hausdorff Distance

Method	K [%]
Manually-Segmentation	91
Active Contour Segmentation	95

The results shown in Table 1 indicate that virtually all the boundary points lie within some pixels of the manual segmentation, but the segmentation is better in the case of the proposed approach.

5. CONCLUSION

In this paper is presented a new and effective approach for kidney segmentation in US images. It consists of contrast enhancement based on CLAHE and speckle noise reduction with modified homomorphic filter based on wavelet packet decomposition. The method of segmentation is based on active contour without edges. The implemented study and obtained results have shown a high validation of the segmentation. We obtain that this method is very robust to initialization and gives better results, when there is a difference between the foreground and background. Our future work will be concentrated in hybrid methods for segmentation of other organs in US images in regard to their specific.

6. ACKNOWLEDGMENTS

The paper was supported by the PhD Students Research Project "Algorithms for US Image Segmentation based on Wavelet Transformation", NIS № 152 PD0019-07/2015.

References

[1] J. A. Noble, "Ultrasound image segmentation and tissue characterization", Journal of Engineering in Medicine, vol. 224, no. 2, pp. 307–316, 2010

[2] M. Martın-Fernandez, C. Alberola-Lopez, "An approach for contour detection of human kidneys from US images using Markov random fields and active contours," Medical Image Analysis, vol. 9, no. 1, pp. 1–23, 2005.

[3] S. Dahdouh*a, E. Frenoux and A. Osorioa, Real time kidney ultrasound images segmentation: a prospective study, SPIE Proceedings Vol. 7265, 2005

[4] S. Vassilev, A Brief Survey of Segmentation Techniques Applied in Kidney Ultrasound Images, Computer & Communications Engineering, Vol. 9 No. 2, /2015.

[5] C. Peters and R. Chevalier, "Congenital urinary obstruction: Pathophysiology and clinical evaluation," in Campbell-Walsh Textbook of Urology, Eds. Elsevier, Inc., Philadelphia, 2012

[6] J. Bakker, M. Olree, R. Kaatee, E.E. de Lange, K.G.M. Moons, J. J. Beutler, and F. J. A. Beek, "Renal volume measurements: Accuracy and repeatability of US compared with that of MR imaging," Radiology, vol. 211, no.3, pp. 623–628, 1999.

[7] T. Chan, L.Vese, "Active Contours Without Edges", IEEE Transactions on Image Processing, vol.10, № 2, pp.266-276, 2001.

[8] V. Georgieva, S. Vassilev, "Despeckling of Medical Ultrasound Images based on Wavelet Decomposition", Proceeding of 10th International Conference on Communications, Electromagnetism and Medical Applications (CEMA'15), pp. 31-34, Sofia, Bulgaria, 2015.

[9] MATLAB User's Guide. Accessed at: www.mathwork.com

[10] M.Leventon, W.Grinson, O.Faugeras, "Statistical Shape Influence in Geodesic Active Contours", Computer Vision and Pattern Recognition, vol.1, pp.316-323, 2000.

SIMPLIFIED METHOD OF LED LAMP USEFUL LIFE PROJECTION

Vytautas Dumbrava, Irmantas Kupčiūnas, Darijus Pagodinas, Vytautas Knyva, Gedeiminas Činčikas

Department of Electronics Engineering, Studentu str. 50-340, Kaunas, Lithuania, LT-51368
E-mail: vytautas.dumbrava@ktu.lt

Abstract

LED lamps have experienced growth of usage in artificial lightning because of high luminous efficiency, long life and resistance to mechanical stress. A lot of new manufacturers are starting to make such lamps and a part of them does not have experience in this particular field. This leads to cheap products, which does not meet product specific requirements. Due to this reason a case study was started in order to analyze standards governing LED lamps and do simplified evaluation of specific LED lamps.

1. INTRODUCTION

The area of artificial lighting has gone through a lot of important changes in last decades. At first, light emitting diodes (LED) were used only for identification purposes, but now using advanced technologies it is possible to fully replace 60W bulb with a LED lamp [1]. LED lamps are getting more and more popular because they have high luminous efficiency, long life (up to 50 000 hours) and low power consumption compared to conventional incandescent lamps. Such advantage allows reducing electricity bills. Production of LED lamps is growing and more manufacturers are starting make them. Most of the LED lamps in Europe are imported from China and these lamps are relatively cheap. However stability of LED lamps parameters and reliability becomes complicated. With increasing manufacture rates emerges production that does not meet claimed technical parameters and has low repeatability of characteristics. Because of these reasons buyer or importer may be harmed. To reduce chance of this harm and choose reliable suppliers, need for extensive testing of imported LED lamps arises.

The aim of this work is to evaluate possibilities of measuring LED lamps parameters, level of standardization, measure parameters of provided LED lamps and present the results of measurements.

2. OBJECT OF THE RESEARCH

The object of this research is integrated LED lamp. This type of lamp has integrated light source – matrix of light emitting diodes, LEDs driver and base compatible with ANSI standard. Lamp is suitable to be powered directly from mains. LED lamps for research was provided by Lithuanian importer UAB “SIRIJUS”. Since lamps were very cheap there was almost no characteristics provided. All data provided is listed in table 1.

Table 1. Initial data of examined LED lamps

Model	Angle of illumination	Luminous flux, lm
GU10-5050-F24	120	320
GU10-3*1W-B	45	240
GU10-4*1W	45	320
B45-E14	160	180
G50-5050-WC12	120	180
JDR E14	120	340
C30-5050-WC12	120	180
C30L-5050-WC12	120	180
JDR E14 60LED	120	180

Also there were lamps with no characteristics provided, so they are not included in table 1. Lamps differentiate by shape, used case materials, light emitting diodes, reflectors. One of the lamps used in research is depicted in figure 1.

Figure 1. GU10 3*1W-AC-L warm-white LED lamp

3. OVERVIEW OF LED LAMP CHARACTERISTICS AND MEASUREMENT TOOLS

We think that the most important characteristics of LED lamp are emitted luminous flux and its degradation over time. Measurement of emitted luminous is defined by Illuminating Engineering society (IES) in documents LM-79, LM-80 [2, 3]. For measuring total emitted luminous flux it is recommended to use an integrating sphere system or a goniophotometer. We shall cover only integrating sphere system.

There is simplified method proposed for relative measurement of emitted luminous flux in article [4]. The idea is to use wooden box to simulate black room. We used mentioned approach and built black box by ourselves, it is depicted in figure 2. The internal dimensions are: 56 cm height, 17 cm depth and 35 cm width. Section with holder is approximately 18 cm height. In figure 3: 1 – lamp holder, 2 – holder for lux meters probe, 3 – lux meter. The interior of box was coated with black mat paint to give closer approximation of dark room.

Although this way of measuring only evaluates forward emission of light, so results cannot be used to compare different models lamps. However it is possible to compare LED lamps of the same model or compare it to itself in order to evaluate its degradation over time.

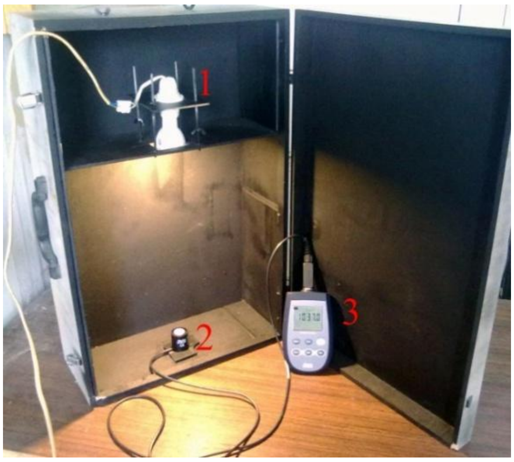

Figure 2. Black box, that we built

4. EVALUATION OF EMITTED LUMINOUS FLUX DEGRADATION

One of the drawbacks of light emitting diodes is luminous flux degradation over time. Normally there are two degradation levels defined – 50% (L50) and 70% (L70) of initial LED lamps luminous flux. However depending on application, L50 or L70 luminous flux degradation may by unacceptable. For example if LED lamp is used to illuminate writing desk it will become unsuitable for usage before reaching its luminous flux degrades to 50% of the initial flux.

There have been solid attempts to approximate light emitting diode luminous flux degradation over time as a function of time [5, 6]. Degradation may be approximated as exponential function [5]:

$$y = e^{\alpha t}. \tag{1}$$

In formula: y - relative luminous flux; t – time, h; α - degradation constant. Value of α is found from experimental results. According to [5] degradation constant depends on LEDs forward current I:

$$\alpha = 5 \cdot 10^{-5} \cdot e^{(0,0375)I}. \tag{2}$$

In accordance with formula 2 it should be possible to accelerate luminous flux degradation process by increasing LED forward current. By using data gathered when operating LEDs with increased current it is possible to predict degradation constant in normal conditions. But there is one major drawback – degradation constant must be estimated for every type of LED and this technique is not directly applicable to LED lamps, because they usually have built in current source.

In order to estimate LED lamps useful time until it reaches 70% degradation we adapted method proposed in TM – 21 – 11 published by IES.

5. LED LAMP USEFUL LIFE PROJECTION

TM – 21 – 11 [7] recommends curve – fitting experimentally collected data in order to extrapolate the luminous flux degradation to defined critical value – L70 or L50. Method is applied to each different type of LED lamp.

All experimentally collected data is normalized to 100% at 0 hours for each lamp. Next an exponential least squares curve – fit is performed for each tested type of lamps. The following equitation is used:

$$\Phi(t) = B \cdot \exp(-\alpha t), \tag{3}$$

here: t – operating time in hours; $\Phi(t)$ – normalized luminous flux output at time t; B – initial constant calculated using least squares curve fit; α –

degradation rate constant calculated using least squares curve fit. The following equation from TM – 21 -11 is used to project LED lamps useful life:

$$L_p = \frac{\ln\left(100 \cdot \frac{B}{p}\right)}{\alpha}, \tag{4}$$

here L_p – useful life expressed in hours where p is the percentage of initial luminous flux output maintained.

Coefficients B and α are derived from least squares formula (5, 6):

$$B = \exp(b) \tag{5}$$

$$\alpha = -m \tag{6}$$

Slope (m) and intercept (b) are calculated using formulas (7) and (8):

$$m = \frac{n \cdot \sum x \cdot y - \sum x \cdot \sum y}{n \cdot \sum x^2 - \left(\sum x\right)^2}, \tag{7}$$

$$b = \frac{\sum y - m \cdot \sum x}{n}, \tag{8}$$

here: x, y – experimental data points (x_1, y_1), … (x_n, y_n); n – total number of data points.

6. TEMPERATURE DISTRIBUTION IN LED LAMP

According to some sources [8, 9] LED temperature effect luminous flux output and may affect speed of emitted luminous flux degradation. Distribution of temperature was observed using "MikroSHOT" thermal imaging camera. Temperature of LED mounting plate was measured (Figure 3, 4).

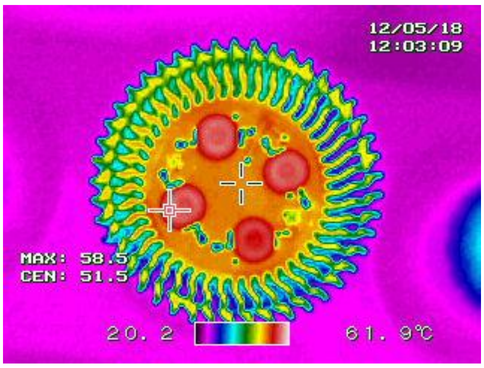

Figure 3. Thermal image of GU10 4X2W-WW

However not all lamps could be disassembled without damaging them, so their case temperature is reported later on (marked with * in table 2).

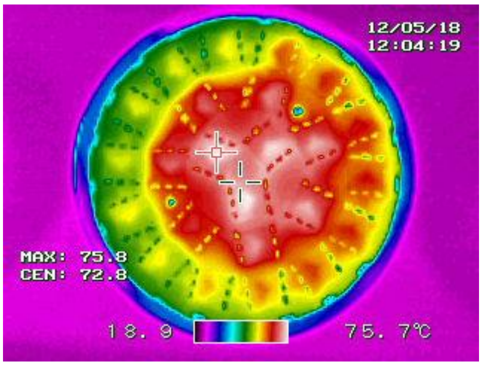

Figure 4. Thermal image of GU10 5050-F24 #1

7. EXPERIMENTAL RESULTS

We have done 2250 hours long test of supplied LED lamps. Measurement intervals were a lot smaller than 1000h suggested by TM – 21 -11 in order to compensate for noisy results due to loose lamp holding point. For each LED lamp model calculations as described earlier were done to calculate its useful time. Results are presented in table 2. The results were very different for each type of lamp – GU10 4X2W (CW) lamp shoved no degradation during test (Fig. 6) while GU10 – 5050 – F24 reached 72% of initial luminous flux output at the end of this test (Fig. 7). For GU10 – 5050 – F24 projected time is 2280 hours.

Table 2. Experimental results

Model	L70,h	α	B	LED temperature, °C
GU10 4X2W (WW)	27442	1.34E-05	1.012248	58.5
GU10 3X1W-AC-L WW	21977	1.66E-05	1.008834	51.8*
GU10-5050-F24 #1	2013	1.77E-04	0.999152	75
GU10-5050-F24 #2	2283	1.58E-04	1.003594	75
B45-14 SMD5050 12 LED	44101	7.54E-06	0.976058	42.1*
C30-5050-WC12	4795	7.42E-05	0.999057	37.6*
C30L-5050-WC12	7731	4.56E-05	0.996129	35.9*
G50-5050-WC12	6547	5.34E-05	0.992665	35.9 *
JDR E14 60LED	10514	3.03E-05	0.962255	65.5
JDR E14 SMD5050 24 LED #1	56162	5.91E-06	0.975720	60.1
JDR E14 SMD5050 24 LED #2	23615	1.40E-05	0.973800	65.5

*Case temperature is reported

The coefficient of determination (R^2) for a linear regression model with one independent variable is:

$$R^2 = \frac{1}{N} \cdot \frac{\sum_{i=1}^{N} (x_i - \bar{x})(y_i - \bar{y})}{\sigma_x^2 \cdot \sigma_y^2}, \qquad (9)$$

where N is the number of observations used to fit the model; x_i is the x value for observation i; $\bar{x}$ is the mean value, y_i is the y value for observation i, $\bar{y}$ is the mean y value, σ_x is the standard deviation of x and σ_y is the standard deviation of y.

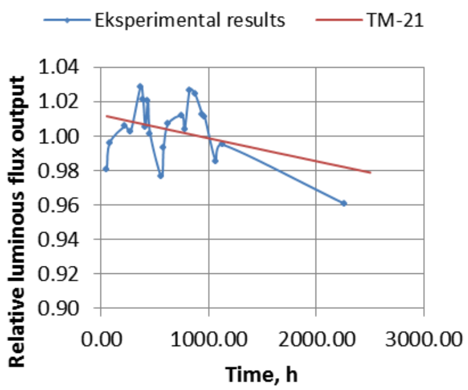

Figure 5. GU10 4X2W (WW) degradation curve

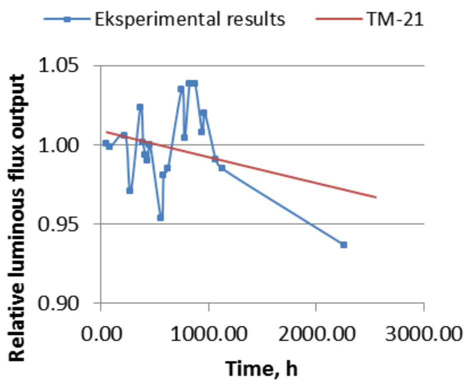

Figure 6. GU10 3X1W-AC-L WW degradation curve

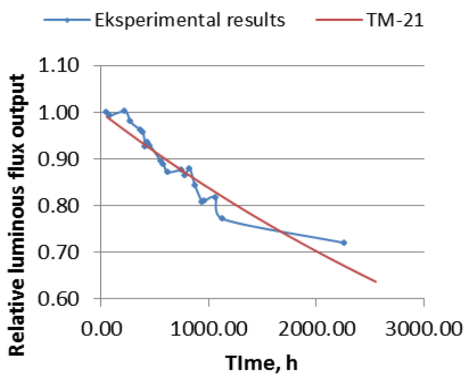

Figure 7. GU10-5050-F24 #1 degradation curve

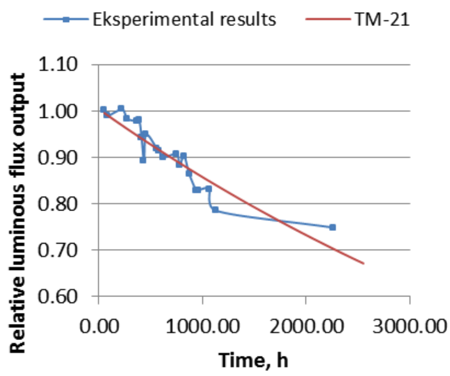

Figure 8. GU10-5050-F24 #2 degradation curve

8. CONCLUSION

Initial LED lamp testing using black box was done. One model of lamp reached 72% initial luminous flux output during this test and projected L70 time is 2280 hours. However in order to confirm this method further work must be done. We plan to significantly increase number of tested lamps and test duration. Also we aim to compare useful life projection results using out black box and integrating sphere.

References

[1] Philips wins L Prize for 60W-replacement LED lamps (MAGAZINE). Internet resource:<http://ledsmagazine.com/features/8/9/14>.

[2] IES LM-79-08. Internet resource: <http://www.lisungroup.com/IESNA-LM-79-08_EN.pdf>.

[3] IES LM-80-08. Internet resource: <http://www.lisungroup.com/IES-LM-80-08.pdf>.

[4] Marcelo Paschoal Dias, Danilo Pereira Pinto e Henrique A. C. Braga. A simplified technique of lighting performance evaluation applied to led-based modern luminaires.

[5] N. Narendran, J. D. Bullough, N. Maliyagoda, A. Bierman. What is Useful Life for White Light LEDs? – IES Paper #52.

[6] X. P. Li, L. Chen, M.Chen, An Approach of LED Lamp System Lifetime Prediction.

[7] IES TM-21-11 Projecting Long Term Lumen Maintenance of LED Light Sources. ISBN: 978-0-87995-259-4.

[8] Biber, C., LED Light Emission as a Function of Thermal Conditions. Semiconductor Thermal Measurement and Management Symposium, 2008. Semi-Therm 2008. Twenty-fourth Annual IEEE.

[9] L. Liu, D. Yang, G. Q. Zhang, Z. You, F. Hou, D. Liu. Thermal Performance Analysis of Photoelectric Parameters on High-power LEDs Packaging. Thermal, Mechanical and Multi-Physics Simulation and Experiments in Microelectronics and Microsystems (EuroSimE), 2011 12th International Conference on CD-ROM.

DIFFERENT SIGNALS' PARAMETERS INFLUENCE ON IMAGE QUALITY ASSESSMENT

Tomas Adomkus*, Lina Narbutaitė*, Rasa Brūzgienė**

*Faculty of Informatics, Kaunas University of Technology
**Faculty of Electrical and Electronics Engineering, Kaunas University of Technology
Studentu str. 50-204a, Kaunas, Lithuania, LT- 51368

E-mail: tomas.adomkus@ktu.lt

Abstract

Currently, the growing number of video transmissions in mobile networks takes an increasing part over all telecommunications services usually got by mobile users. High-quality mobile video transmissions are dependent on the parameters of wireless transmission medium, so it is very important to choose the appropriate signal parameters as wireless transmission medium is particularly responsive to environmental factors. Due to this, the authors carried out the different investigations. The evaluation of different wireless signals' modulations and various noises was done in order to investigate it influence on the quality of the transmitted video images. The investigations were carried out by analyzing images of different types and compressions. The different criteria were used for the objective assessment of video quality in these investigations. The results of all investigations and it based conclusions are presented in this paper.

1. INTRODUCTION

The opportunity for users' mobility and streaming of video services to anywhere and access it content at any time is a uniqueness of wireless networks, which allows to lead in competition with wired networks. However, the streaming of high quality video services is a challenging process to the providers of wireless networks. The digital video transmission passes a number of processing stages with a variety of devices in wireless system while it reaches the end user's mobile device. Therefore, various distortions in a video stream can occur during it transmission. These distortions can be visually visible to the mobile users and can cause their negative emotions on perceived quality of video services [1]. Moreover, a high quality wireless video transmission is very challenging for multi UAV (*Unmanned Air Vehicle*) systems, such as FANET (*Flying Ad-Hoc Networks*) [2]. It is related not only to the video stream processing over different devices in the wireless systems, but with signals' parameters over different wireless transmission medium (as LTE [3], WiFi [4], *etc.*) as well. The wireless signals' modulations and wireless signal strength in the level of background noise are one of the main characteristics, which affect quality of video stream, transmitted over wireless medium. SNR (*Signal-to-Noise Ratio*), PSNR (*Peak Signal-to-Noise Ratio*), and BER (*Bit Error Rate*) are well known key parameters that are used in assessing wireless systems. The authors used these criteria in combination with objective video quality methods as MOS (*Mean Opinion Score*) for the assessment of different wireless signals' parameters influence on transmitted video quality.

So the task of this paper was to investigate the influence of different wireless signals' parameters to the quality of transmitted video stream. Based on the results of investigations, the authors recommended the approach for the video transmission process, which would help to improve the quality of video services transmission over wireless networks.

The paper is organized as follows. Section 2 describes the investigations and video snapshots of the evaluation of influence of wireless signal's parameters on quality of video images. Section 3 combines video snapshots with a graphical results and objective video quality assessment. Finally, Section 4 presents the conclusions and authors' recommendations.

2. EVALUATION OF INFLUENCE OF WIRELESS SIGNAL'S PARAMETERS ON QUALITY OF VIDEO IMAGES

The investigations were done by using MATLAB simulation platform. Three different wireless signals modulations were used:

- QPSK (*Quadrature Phase Shift Keying*),
- QAM (*Quadrature Amplitude Modulation*) - 64,
- QAM - 256.

The two types of video images with different colour basis were taken for the investigations:

- video image with cat – greyscale and size 656x368;
- video image with tucan – colourful and size 640x336.

The parameters, which authors used in investigations [4, 5]:

$$PSNR = 10\log\frac{(2^n - 1)^2}{MSE}, \qquad (1)$$

$$MSE = \frac{1}{MN}\sum_{i=1}^{M}\sum_{j=1}^{N}(f(i,j) - f'(i,j))^2; \qquad (2)$$

where *f(i,j)* describes original picture of the video; *f'(i,j)* – describes transmitted picture to the user mobile device; *M* x *N* – the resolution of video in pixels.

The conversion of PSNR to objective MOS value was done according [6].

First of all, the investigation of evaluation of SNR level impact to the quality of video images transmitted with different wireless signals' modulations were done. Figures 1 and 2 present visual results from this investigation. It is clearly visible, that the highest quality of transmitted video is for QPSK modulation in both figures (fig. 1-2). The increased level of SNR eliminates most visually visible artifacts from video images, which were transmitted with QAM-64 and QAM-256 modulations. However, it isn't competitive to quality of video with QPSK modulation.

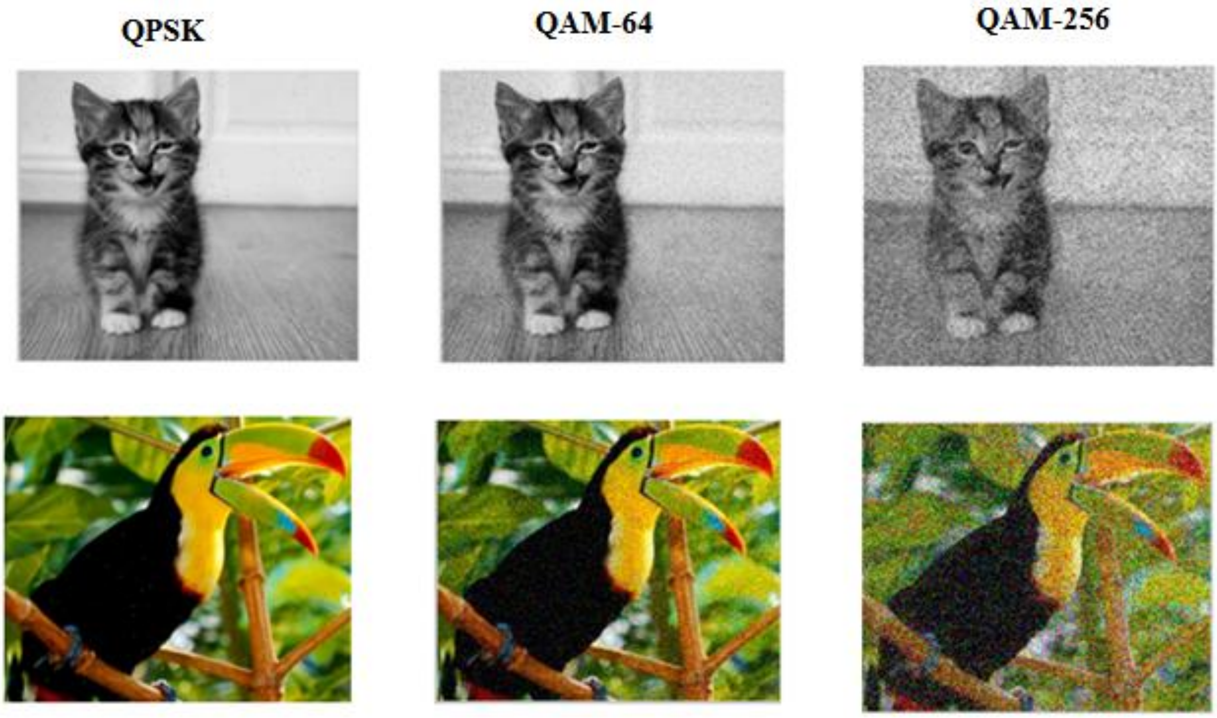

Figure 1. Video image quality for different modulation of wireless signal, when SNR=10 dB

Secondly, the authors investigated how different SNR levels can affect quality of transmitted video, when the modulation is QAM-256 (Fig. 3). This modulation was selected, because it is able to carry more bits of information per symbol in difference from others. The results of this investigation showed, that SNR level should be increased more than 3 times for the satisfying transmission of video without visual hum.

The noise level and type [7, 8] is very important factor for video transmission quality in wireless networks. Therefore, the authors investigated influence of Additive White Gaussian noise (*AWGN*) and multiplicative uniform noise to the quality of transmitted video over different wireless signal's modulations (Fig. 5).

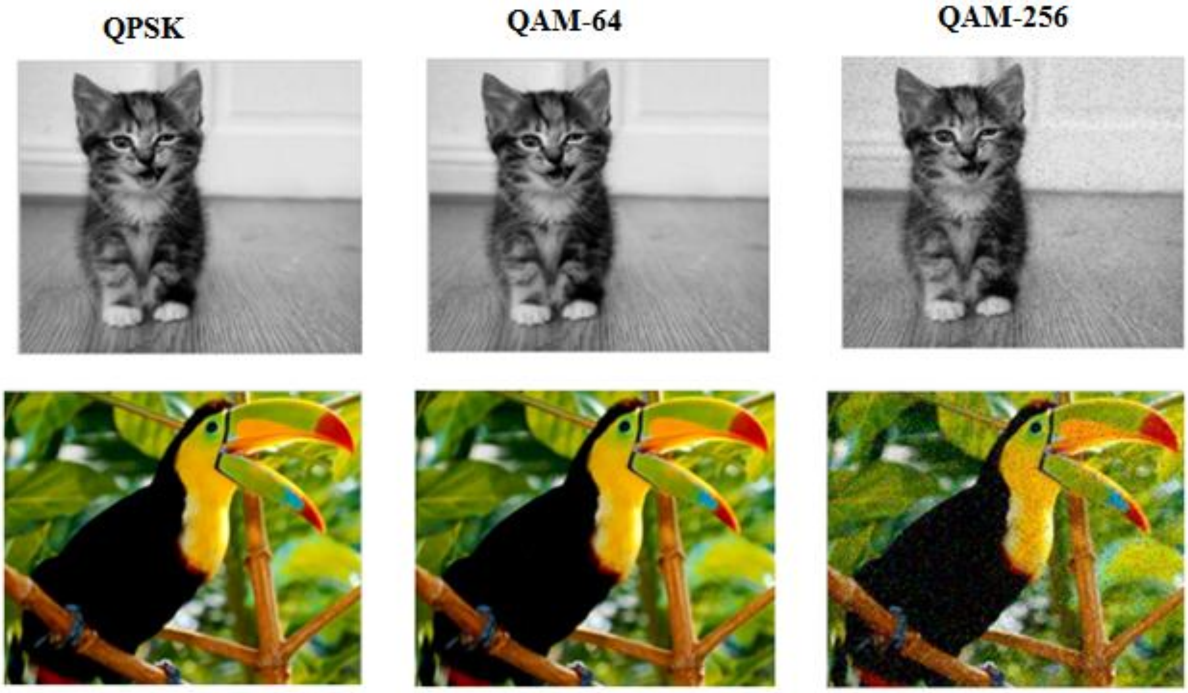

Figure 2. Video image quality for different modulations of wireless signal, when SNR=18 dB

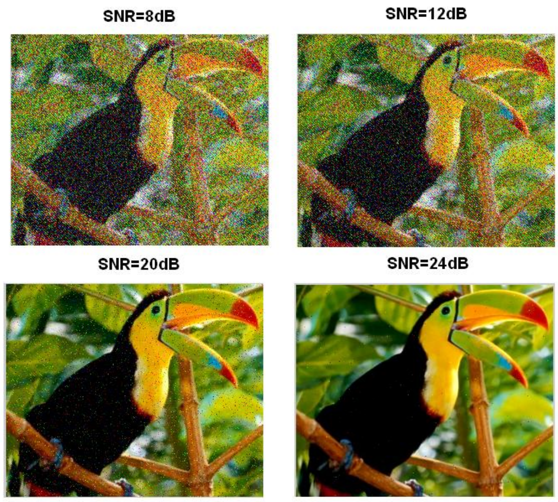

Figure 3. Video image quality for different SNR values, when modulation is QAM-256

AWGN is the effect of thermal noise generated by thermal motion of electrons in all dissipative electrical components. The results showed that AWGN more influences quality of video, which was transmitted over QPSK. The significant difference is for multiplicative uniform noise, which affect quality of video in all modulations.

Figure 4. Video image quality, when BER= 11.7882e-004

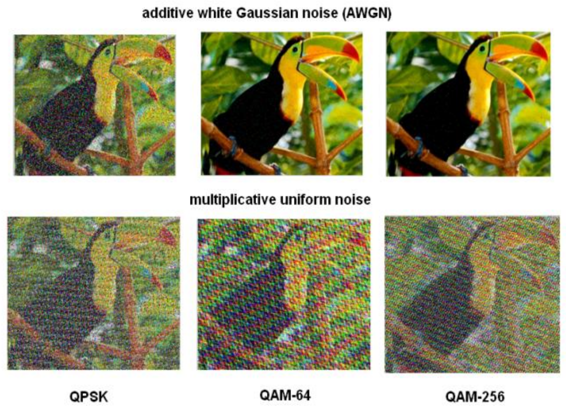

Figure 5. Video image quality for different types of noise

The last investigation was done for the evaluation of necessary SNR level for each wireless signal modulation in order to receive the video image with a good quality (without any visual artefacts). The BER criterion was used as the required maximum 2E-3 level of bit errors for perceived video of a good quality. BER is the estimated probability that a bit transmitted will be received incorrectly through a device or network. Figure 4 shows results from this investigation. It was stated, that for QAM modulation it is necessary to have several times higher SNR value in comparison to QPSK in order to have a good quality video transmission over wireless networks. In addition, it comes a recommendation for a higher SNR to ever-higher type of QAM modulation as well.

3. ASSESSMENT OF VISUAL VIDEO SNAPSHOTS WITH A GRAPHICAL RESULTS AND MOS

The visual results from the previous investigations were combined with graphical results, presented in Figures 6 and 7. Image enhancement or improving the visual quality of a digital image can be subjective. Saying that one method provides a better quality image could vary from person to person. For this reason, it is necessary to establish quantitative/ empirical measures to compare the effects of image enhancement algorithms on image quality. Therefore, we calculated parameters BER and PSNR. After that, main metric PSNR was converted to objective MOS value. The parameters of investigation - BER, PSNR and MOS - were calculated using MATLAB.

PSNR is defined as the ratio of the total number of pixels in the compressed image to the mean square error in dB. Typical PSNR over 40dB is often considered undistinguishable from the original. The lower and upper limits for PSNR are 20dB and 40dB, respectively [9].

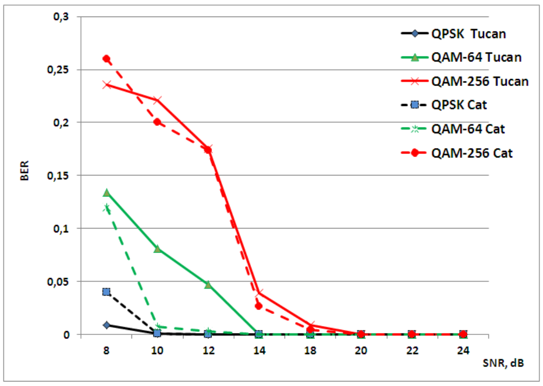

Figure 6. Dependence of BER on SNR for different quality of video images

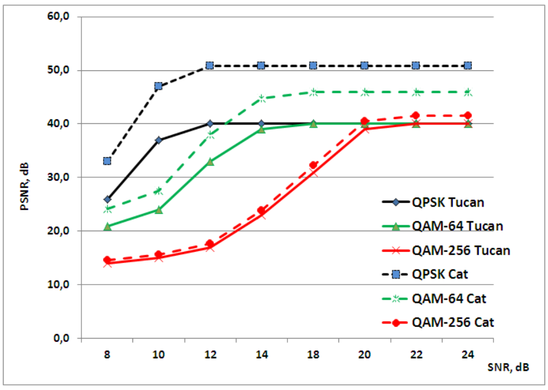

Figure 7. Dependence of PSNR on SNR for different quality of video images

In Figure 7, we can observe that PSNR values decreases when SNR is less then 14dB, because from this value increases the BER value (see Figure 6). It influences very much the quality of video image, if it was used QPSK modulation in wireless medium and was a different image compression and colour ratio. The proposal is that the higher PSNR level, the better-degraded image will be reconstructed to match the original image as well the better reconstructive algorithm will be used. This would occur because we wish to minimize MSE (*Mean Squared Error*) between images with respect of the maximum wireless signal value to the video image quality.

The dependency of MOS on SNR for different signals' modulations was calculated using the mapping between PSNR and MOS. The results are presented in the Figure 8.

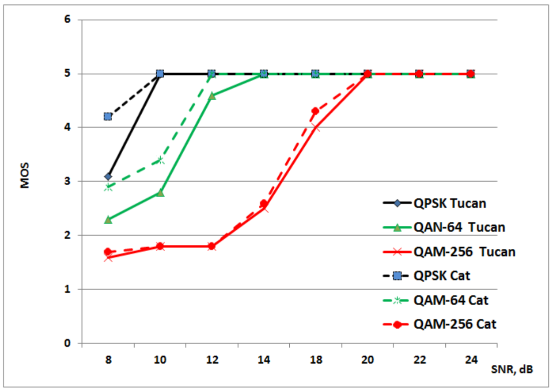

Figure 8. Dependence of MOS on SNR for video images of different modulations

As it can be seen, the higher MOS values are for the both types of video images, which were transmitted with QPSK modulation. The worst evaluation of video quality is for video images with QAM-256 modulation. This leads to the conclusion that using of QAM modulation for a video streaming over wireless networks increases the probability of errors in all video streams. And this impacts to the appearance of annoying artifacts visible during the wireless video transmission, which affect the subjective assessment of video quality (to a lower grade of MOS) by the mobile users.

4. CONCLUSIONS

The investigations for different signals' parameters influence on image quality assessment showed, that the wireless signals' modulations affect quality of transmitted video images in different ways. The lower signal modulation, as QPSK, will be used for a video transmission, the better quality of video the mobile user will receive. However, the lower signal modulation will gives a lower data rate of a wireless link, which also will cause a negative impact on the mobile users' visual perception and emotions. QAM-64 or QAM-256 modulations give a higher data rate for a wireless video transmission, but it impacts the quality of transmitted video images in several times. This is because the higher modulations are less resilient to noise or interference over wireless transmission medium. Due to this, the main recommendation is to balance the level of SNR for an ever-higher type of signal modulation in such way, that it could improve the quality of transmitted video images in a positive way. The level of SNR should be increased for an ever-higher type of wireless signal modulation.

5. ACKNOWLEDGMENT

This work has been partially supported by the ICT COST Action IC1304 - Autonomous Control for a Reliable Internet of Services (ACROSS), November 14, 2013 – November 13, 2017, funded by European Union.

References

[1] Anush Krishna Moorthy, Kalpana Seshadrinathan, Rajiv Soundararajan, Alan Conrad Bovik. "Wireless Video Quality Assessment: A Study of Subjective Scores and Objective Algorithms", IEEE Transactions on Circuits and Systems for Video Technology, vol. 20, no. 4, 2010, pp. 587 - 599.

[2] Bekmezci; O., K., Sahingoz; Ş., Temel. "Flying Ad-Hoc Networks (FANETs)", Ad Hoc Networks, vol. 11, issue 13, 2013, pp. 1254-1270.

[3] PTCEL. "Maximizing LTE Performance Through MIMO Optimization", white paper, April, 2011, pp. 1-14.

[4] Brūzgienė, R.; Narbutaitė, L.; Adomkus, T.; Cibulskis, R. "The impact of video streaming on quality of experience over 802.11n dual Band networks: experimental evaluation", Electronics and electrical engineering, vol. 20, no. 6, 2013, pp.158-161.

[5] M. Mrak; S. Grgić; M. Grgić. "Picture Quality Measures in Image Compression Systems", In Proceedings of the Eurocon 2003 conference, 2003, Ljubljana, Slovenia, pp. 233-237.

[6] T. Kratochvil; P. Šimiček. "Utilization of Matlab for picture Quality evaluation", In proceedings of Institute of Radio Electronics, Brno University of Technology, Czech Republic, 2005.

[7] M., S., El-Mahallawy; A., Hashad; H., Hassan Ali; H., Sami Zaky. "Quality Estimation of Video Transmitted over an Additive WGN Channel based on Digital Watermarking and Wavelet Transform", In World Academy of Science, Engineering and Technology, 2009, pp. 419 – 423.

[8] R., Verma; J., Ali. "A Comparative Study of Various Types of Image Noise and Efficient Noise Removal Techniques", International Journal of Advanced Research in Computer Science and Software Engineering, vol. 3, issue 10, 2013, pp. 617 – 622.

[9] S. Khan; S. Uhovnikov; E. Steinbach. "MOS-Based Multiuser Multi-application Cross-Layer optimization for Mobile Multimedia Communication," Advances in Multimedia, Hindawi Publishing, 2007

CAVITY RESONATOR FOR STUDYING THERMAL AND NON-THERMAL EFFECTS OF RADIO WAVES ON BIOLOGICAL TISSUES

Hristo Gochev [1], Boncho Bonev[2], Peter Petkov[3]

Faculty of Telecommunications at Technical University of Sofia, 8 Kl. Ohridski Blvd, Sofia 1000, Bulgaria

E-mails: gochev.h@gmail.com; bbonev@tu-sofia.bg; pjpetkov@tu-sofia.bg

Abstract

In this article a design and simulation of a circular cavity resonator is presented. The resonator will later on be used to conduct a study on thermal and non-thermal effects of radio waves on cancer cells. The cells will be irradiated with different intensities and modulation schemes and later on the samples will be examined by medical scientists to determine if cancer treatment could benefit from the non-thermal effects of RF radiation.

***Keywords** – Microwaves, Cancer treatment, Cavity resonator, non-thermal effects, thermal effects*.

1. INTRODUCTION

The research of the effects of Electromagnetic Field on biological systems is of growing interest. In recent years one of the main directions of research on this topic is the application of RF fields in medicine [1] [2] [4]. Our work is concentrated on cancer treatment using radio waves. There are multiple studies conducted on microwave heating and very few on non-thermal effects of radio waves on malignant cell. Microwave heating, or microwave hyperthermia, is a procedure where high frequency electromagnetic field is applied on parts of the human body and is used to elevate their temperature [1]. Non-thermal effects occur at low power of the applied field, which is not enough to heat the tissue.

This paper describes a device that will be used to conduct a study on how low power FR radiation affects cancer cells. On this early stage of our research however we will study the ability of radio waves at 434 MHz to penetrate and heat different types of tissues. The experiment itself will be performed in collaboration with medical scientists who will study the samples and will analyze all the possible effects of RF radiation on the cancer cells, if any.

2. DESCRIPTION OF THE RESONATOR

To conduct the experiment described above we will have to put the samples containing the cancer cells in controlled environment and radiate them with electromagnetic radiation. In order to have reliable results the samples must be radiated by constant EM field which has well known spatial distribution. We should also ensure that the samples won’t be subjected to the influence of sources of FR radiation other than our own. This is important because all unwanted and uncontrolled influence can compromise the results.

Such a device that can meet both conditions is a cavity resonator. The electromagnetic field inside the cavity resonator is incased within the boundaries of the cavity. Its structure can be calculated using software model and later on it can be experimentally measured. This means that we will have full knowledge of the EM field inside the cavity and can guarantee that it will be the same during the whole experiment. On the other hand no outside EM energy can penetrate within the cavity. This makes the cavity resonator very convenient for conducting our study.

We have chosen to utilize cylindrical cavity resonator with resonant frequency 443 MHz for mode TM_{010}. One of the walls of the cavity will be removable and the sample will be put inside of it.

The resonant frequency of the cavity is calculated using[3]:

$$f_r = \frac{1}{2\sqrt{\mu\varepsilon}}\sqrt{(\frac{x_{np}}{a})^2 + (\frac{q\pi}{d})^2} \quad (1)$$

For mode TM_{010} n=0, p=1, q=0, and for the resonant frequency we have:

$$f_r = \frac{3.10^{10}}{2}\sqrt{\left(\frac{2.405}{2}\right)^2} \quad (2)$$

The calculated dimensions of the cavity are as follows – height d=0.25 m; radius a= 0.259m. The size of the cavity is big enough to contain the sample with the cancer cells.

Slots will be cut out on the walls of the resonator so that we can experimentally measure the EM field inside of it and to compare it to the simulation results.

The cavity will be fed by coaxial line from RF generator.

3. SIMULATION AND RESULTS

The properties of the resonator are simulated using COMSOL Multiphysics software. COMSOL calculates the electric and magnetic field inside the cavity resonator, surface losses and surface currents density. We are also able to calculate the microwaves induced heating in the biological tissues.

To calculate the temperature of the tissues Pennes bioheat equations is used [1]:

$$\rho C_p \frac{\partial T}{\partial t} + \nabla \cdot (-k\nabla T) = \rho_b C_b \omega_b (T_b - T) + Q_{met} + Q_{ext} \quad (3)$$

where ***k*** is the corresponding tissue's thermal conductivity (W/(m·K)), ρ_b represents the blood density (kg/m3), C_b is the blood's specific heat capacity (J/(kg·K)), ω_b denotes the blood perfusion rate (1/s), and T_b is the arterial blood temperature (K). Further, Q_{met} is the heat source from metabolism, and Q_{ext} is an external heat source, both measured in W/m3. The initial temperature equals ***Tb*** in all domains. This model neglects the heat source from metabolism.

The model assumes that the blood perfusion rate is ω_b=0.0036 s-1, and that the blood enters the corresponding tissue at the body temperature T_b = 37 °C and is heated to a temperature, ***T***. The blood's specific heat capacity is C_b=3639 J/(kg·K).

We use simple models of three types of tissues- liver, fat, muscle. The electromagnetic properties of these tissues at the frequency of interest 443 MHz are given in Table 1 [5].

Tissue	Permittivity	Electrical Conductivity [S]
Liver	50.5	0.672
Muscle	56.8	0.807
Fat	11.6	0.0826

On Figure 1 and Figure 2 the mesh and the geometry of the model is shown. The biological tissue is modelled as a sphere with radius of 5 centimeters and is placed along the vertical axis of the resonator.

On Figure 3 you can see the distribution of the Electric and magnetic fields inside the cavity. The EM field is stronger near the axis of the cavity and drops to zero at the side walls which is in compliance with the air- conductor boundary conditions.

The configuration of the EM field inside the resonator points out that the best location to place the cancer cells is at the center of the cavity as far as possible from its walls.

On Figure 4 the surface losses and surface current density of the resonator is displayed.

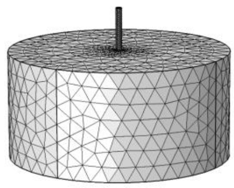

Figure 1. Mesh used for the calculation

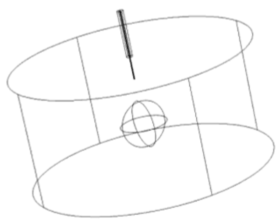

Figure 2. The geometry of the model. The sphere inside the resonator represents the biological tissue.

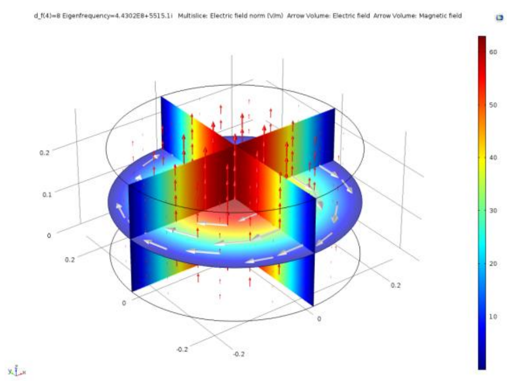

Figure 3. Electromagnetic field distribution inside the resonant cavity

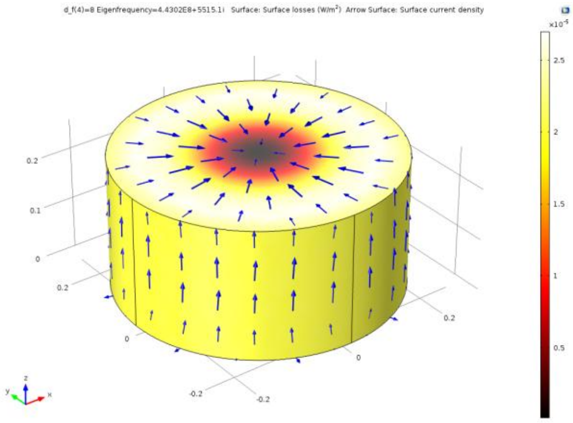

Figure 4. Surface losses and surface current density

In the model we simulate electromagnetic radiation with constant power for 10 minutes. The initial temperature of the tissue is 37 ℃. On figure 5 the temperature distribution after 6 minutes of heating of a liver tissue is displayed. Because of the symmetry of the model we only represent the results in a single plane that goes along the central axis of the tissue.

The temperature distribution after 10 minutes of heating is presented on Figure 6. It's visible that the heating is concentrated in the center of the sample and that the longer we heat the temperature rises and the heating becomes more uniform.

On the next two set of figures Figure 7 and Figure 8 the temperature distributions for muscle tissue after heating for 6 and 10 minutes are displayed.

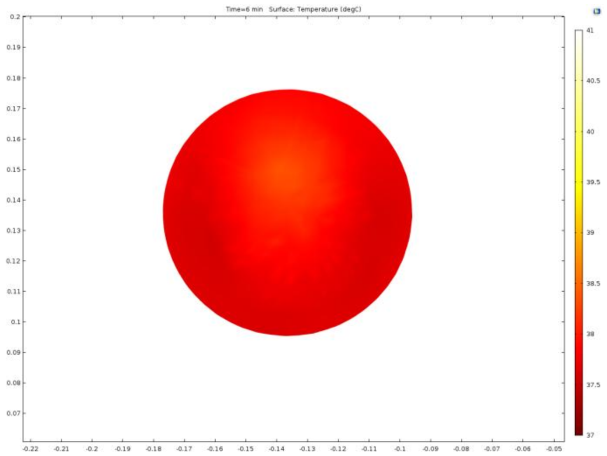

Figure 5. Temperature distribution in liver tissue after 6 minutes of heating

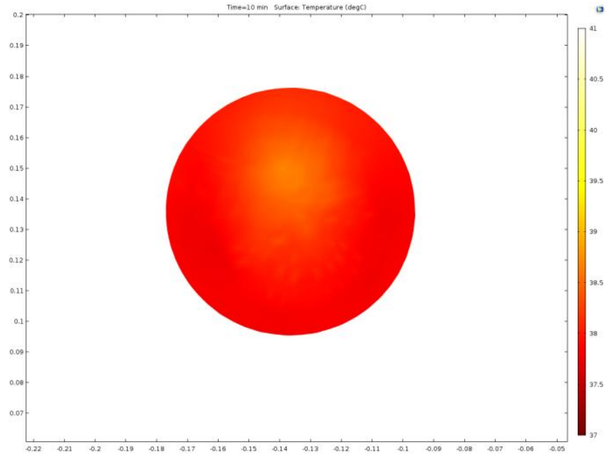

Figure 6. Temperature distribution in liver tissue after 10 minutes of heating

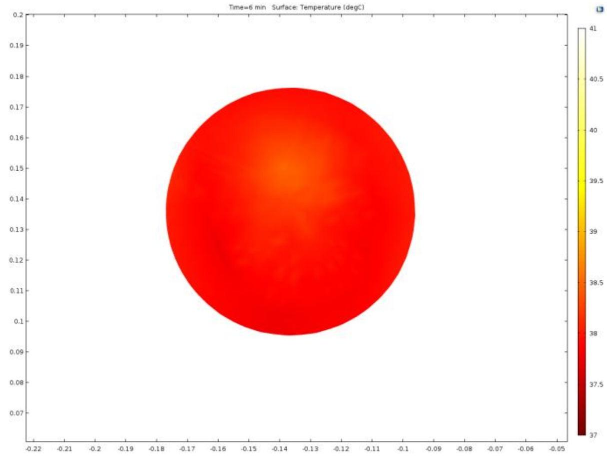

Figure 7. Temperature distribution in muscle tissue after 6 minutes of heating

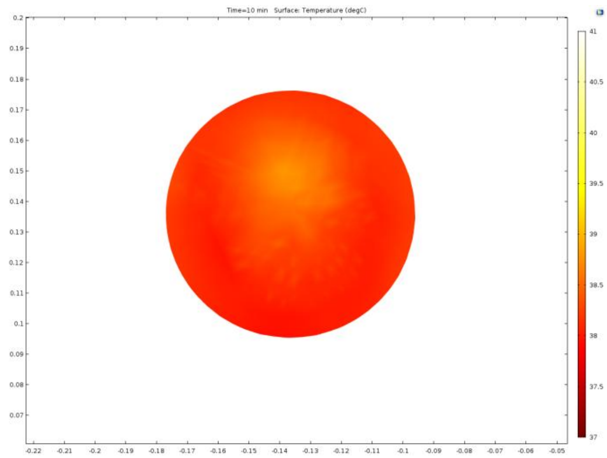

Figure 8. Temperature distribution in muscle tissue after 10 minutes of heating

On Figure 9 Figure 10 the temperature distributions for fat tissue after heating for 6 and 10 minutes are displayed.

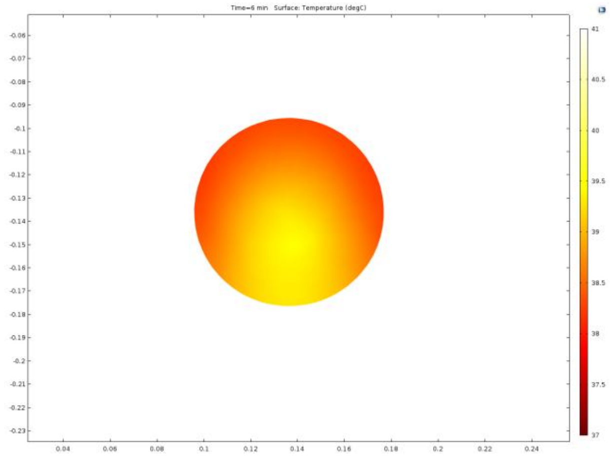

Figure 9. Temperature distribution in fat tissue after 6 minutes of heating

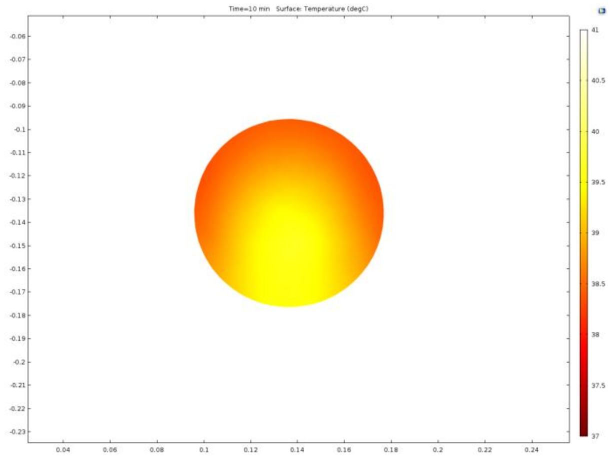

Figure 10. Temperature distribution in fat tissue after 10 minutes of heating

It's easily seen that different kinds of tissues react to the heating in different way. The degree of heating of a certain tissue greatly depends on the blood perfusion for this tissue.

From the results of the simulation we can conclude that using radio waves with frequency of 443 MHz we can achieve significant penetration in the tissue of interest.

The results of the simulation include only the thermal effects of the irradiation, because non-thermal ones can't be simulated using software model. They will be studied later on when we fabricate the resonator using real tissue samples.

4. FUTURE CHALLENGES

After the software simulation next step is to produce the resonator and to measure its properties. If they agree with the simulation results and we can guarantee constant field distribution, we can proceed with the actual study of the effects of the EM field on the cancer cells.

The samples will be irradiated with different types of electromagnetic waves:

- Different intensities of the field
- Time modulation of the wave – periods of irradiation will be followed by periods of silence.
- The high frequency (443MHz) wave will be modulated with modulated with low frequency (several kilohertz) one

The influence of radio waves on the samples will be examined also in combination of drugs to test whether or not the RF radiation can improve the effect of the drugs.

References

[1] Mihaela Morega, Laura Mogos, M. Neagu, Al. Morega, "Optimal Design for Microwave Hyperthermia Applicator"

[2] Barbora Vrbova, J. Vrba, "MICROWAVE THERMOTHERAPY IN CANCER TREATMENT: EVALUATION OF HOMOGENEITY OF SAR DISTRIBUTION"

[3] David M. Pozar, "Microwave Engineering", Fourth Edition, John Wiley & Sons, 2012

[4] Tomas DRIZDAL, Michal VRBA, Michal CIFRA, Paolo TOGNI, Jan VRBA, "Feasibility Study of Superficial Hyperthermia Treatment Planning Using COMSOL Multiphysics"

[5] http://www.itis.ethz.ch/virtual-population/tissue-properties/database/dielectric-properties/

OPTIMIZATION OF THE MECHANICAL UNITS IN MEDICAL CENTRIFUGE, (CHAIR OF BARANY) WITH VARIABLE MECHANICAL TIME CONSTANT

Ts. Kachamachkov, D. Bakardzhiev, Hr. Bakardzhiev, V. Manoev

Technical University of Sofia, Bulgaria,

E-mails: eng_kachamamachkov@abv.bg; dim_bak@abv.bg; vmanoev@tu-sofia.bg

Abstract

We researched the influence of the mass, diameter and the structure of the mechanics on the moment of inertia, the mechanical time constant and the coefficient of efficiency for a class of the mechanisms. We offer a specific solutions to optimize the mechanical units and increase the efficiency of the medical centrifuge, intended for astronauts. Studies have been conducted for a wide range of changing mechanical time constant.

Keywords: *mechanism, mechanical units, efficiency, mechanical time constant, medical centrifuge, astronauts, speed, acceleration, optimization, reliability.*

1. INTRODUCTION

The subject of the research in this work are the nodes that make the mechanical-electrical part of the rotating chair for studies of the vestibular system [1], [2]. Typical of it is that you have to provide a trapezoidal speed chart sinusoidal oscillation – pendulous effect and stop impetus.

The chair is designed for responsible research in the selection of pilots and astronauts the electromechanical part (Figure 1) has a changing radius of rotation, which in turn in medical aspect ensures angular accelerations up to 12g. This is are limit in tests for astronauts.

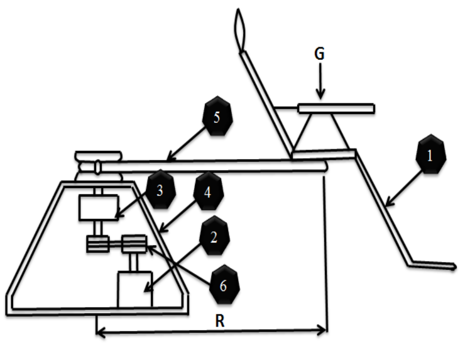

Fig. 1. Electromechanical part of medical centrifuge. Electromechanical part consists of:
1 – chair, 2 – electric motor, 3 – reducer, 4 – housing,
5 – shoulder with changing diameter, 6 - belt drive;

For the sake of high efficiency we offer the following structural changes: elimination of the belt drive and it's replace with perifleks coupler (the coupler is shown in FIG. 2 along with the mechanical properties in Table 1), replacing the coupler with the profiled specifically for the relevant medical centrifuge.

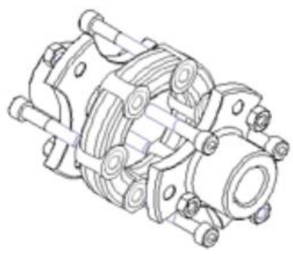

Fig. 2. Perifleks coupler.[3]

Determination of torque $\mathrm{M_H}$

$$\mathrm{M_H} = \frac{P_\mathrm{H}}{\omega_\mathrm{H}} \tag{1}$$

Where:
P_H – is nominal propulsion power.
ω_H – is the nominal rotational speed.

тип-параметър			ДК-60	ДК-80	ДК-100	ДК-150	ДК-200	ДК-250
номинален въртящ момент	Tk n	Nm	10	40	100	400	800	1600
максимален въртящ момент	Tk max	Nm	12	48	120	480	960	1920
максимална честота на въртене	nmax	min-1	3500	3500	3500	3000	3000	3000
диаметри	D	mm	60	80	100	150	200	250
	d1	mm	32	42	47	69	100	150
	dminH8	mm	10	14	19	28	48	55
	dmaxH8	mm	19	24	32	48	65	80
	nxd/R	mm	M6	M6	M8	M12	M16	M20
дължини	l	mm	68	82	122	194	250	325
	b	mm	25	30	50	80	100	130
	e	mm	22	22	24	34	50	65
допустимо несъосие на валовете	Y	mm	2	3	3	4	5	5
макс. относ. завъртане на главините	j	deg	12o	12o	12o	10o	10o	9o
допустимо пресичане на осите	b	deg	2o	2o	2o	2o20'	2o40'	2o40'
допустимо осово изместване	x	mm	2	2	2	3	4	5

parameters selected perifleks coupler for acceleration up to 12 g. Because of these structural changes the kinematic chain acquires the type shown in FIG. 3.

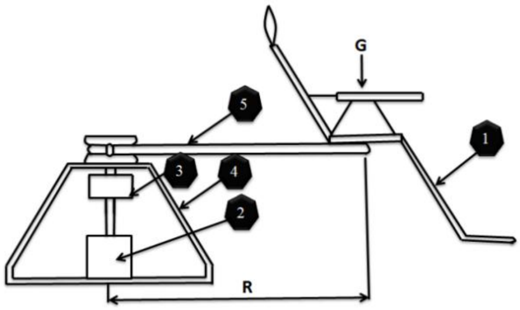

Fig. 3. Electromechanical part with optimized units.

Electromechanical part consists of: 1 - chair; 2 - electric motor; 3 - reducer; 4 - housing; 5 – shoulder with changing diameter;

$$\mathrm{M}_{\text{дв}} - \mathrm{M}_{\text{с}} = J\frac{d\omega}{dt} \pm \frac{\omega^2}{2}\frac{dJ}{d\alpha} = \mathrm{M}_{\text{дин}} \quad (2)$$

Where:

$\mathrm{M}_{\text{дв}}$ – Moment developed by the motor,

$\mathrm{M}_{\text{с}}$ – Moment brought to the shaft of the motor,

$\mathrm{M}_{\text{дин}}$ – Dynamic moment,

J – Brought inertial moment to the motor shaft,

$\frac{d\omega}{dt}$ – Angular acceleration,

α – Angle of rotation,

$$J = \frac{GD^2}{4g} \quad (3)$$

Where:

G – Weight,

D – Diameter under which the electromechanical part rotates (D=2R)

Typical of the tests in the electromechanical system is that the parameter G changes from 392 N to 1373 N, and the parameter D - from 0 to 0,6 m, respectively the moment of inertia changes and the mechanical time constant $\mathrm{T_M}$ by orders of the same magnitude. This makes difficult the optimal adjustment of the electric drive in cases where it is constructed by the system with dependent adjustment also makes difficult the design of adaptive control system under these conditions [4].

Mechanical part incorporates all interconnected moving masses: engine, gearbox and the actuating device of the machine are shown on fig. 4. This movement is realized by a motor Д, reducer КРП, perifleks coupler CM1 and rod Б propelling the chair. The working mechanism, on the schematic diagram are armchair with mass m1 and patient with mass m2. Actuating device transfers the cargo m1 + m2, loaded with a mass $m_{\text{гр}}$, moving with speed $V_{\text{гр}}$, rotating with angular velocity ω and subjected to a force $F_{\text{гр}}$.[5]

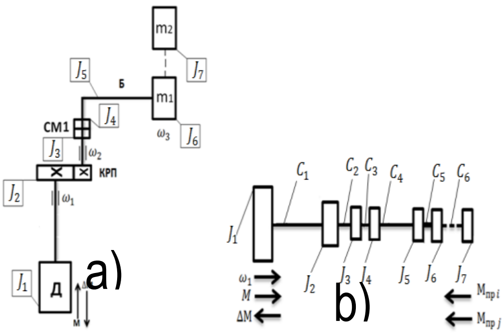

Fig. 4. Schematic diagram of the mechanical part a) and defined kinematic chain b) of medical centrifuge.

On the diagram in Fig. 4 with arrows are shown the applied to the individual mases in the system, adduced moments of the active in the system external forces $M_{\text{пр}\,i}$ and $\mathrm{M}_{\text{пр}\,j}$. To the rotor of the engine J_1 is applied the electromagnetic moment of the engine M and the moment of the mechanical es ΔM, to properly calculate we assumed to be positive sign the direction of the angular velocityω_1. In simplifying of the scheme it is necessary to calculate all externally applied forces on the masses which are connected by means of solid bodies. The study of the dynamics of the electric drive shows that the direct calculation of mechanical scheme in most cases gives the same output as the detailed calculation of the individual forming mechanism. Therefore we identify the main masses and stiffness and bring it down to a two mass system shown on fig. 5, where the system is broth down to the unit with the lowest stiffness and result inertial momentum.[5]

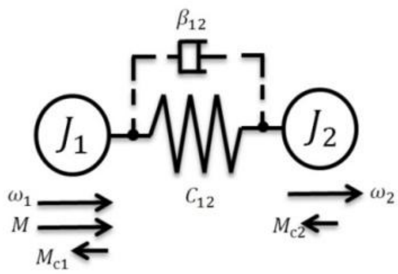

Fig. 5. Summarized two - mass scheme for medical centrifuge

Parameters of two – mass flexible mechanical system (fig. 5), are reduced to the total moment of inertia moments J_1 and J_2, directed to the mechanical connection between them. We accept the moment of elasticity which is brought to the stiffness of a mechanical link J_1 and $J_2 - C_{12}$. The first mass represents the rotor of the engine himself and the mechanical components which have direct contact with him. To this we add the applied electromagnetic moment of the engine *M* and the moment of static load $\mathrm{M_{c1}}$. To the intermediate masses in the mechanism J_2 is applied the resistance moment M_c. [6]

In calculating the above-quoted static moment M_C, when all active forces and momentums in the mechanism are defined. In most cases, losses from friction in the mechanism are unknown and are calculated with the use of the efficiency coefficient of the mechanism.

$$\eta_{\text{мех}} = \eta_1\eta_2\eta_3 \dots, [7]$$

Where $\eta_1, \eta_2, \eta_3 -$ are efficiency coefficients of the units in the kinematic chain.

Comparison of mechanisms based on efficiency:

Medical centrifuge before optimization of mechanical units:

$$\eta_{\text{мех}-\text{пр}} = \eta_{\text{CH}}.\eta_{\text{P}}.\eta_{\text{PEM}}.\eta^5_{\text{ЛАГ}} = 0{,}64 \qquad (4)$$

Where:

$\eta_{\text{CH}} -$ Is efficiency of the coupling.

$\eta_{\text{P}} -$ Is efficiency of the gearbox.

$\eta_{\text{PEM}} -$ Is efficiency of the belt drive.

$\eta^5_{\text{ЛАГ}} -$ Is efficiency of the bearings.

Medical centrifuge after optimization of mechanical units:

$$\eta_{\text{мех}-\text{сл}} = \eta_{\text{CH1}}.\eta_{\text{P}}.\eta^3_{\text{ЛАГ}} = 0{,}72 \qquad (5)$$

Where:

$\eta_{\text{CH1}} -$ is efficiency of the perifleks coupler.

$\eta_{\text{P}} -$ is efficiency of the gearbox.

$\eta^3_{\text{ЛАГ}} -$ is efficiency of the bearings.

If the moment $\mathrm{M_{MEX}}$ of the load in the mechanism is positive, the moment of the static load is detriment from the equations. [6],[5]

$$\mathrm{M_C}\omega_1 = \mathrm{M_{мех}}\omega_{\text{мех}}/\eta_{\text{мех}} + \Delta\mathrm{M}\omega_1 \qquad (6)$$

Therefore

$$\mathrm{M_C} = \mathrm{M_{мех}}/i_0\eta_{\text{мех}} + \Delta M, \qquad (7)$$

Where $\Delta M -$ is the moment of mechanical losses in the engine.

$i_0 = \frac{\omega_1}{\omega_{\text{MEX}}} = i_1 i_2 i_3 \dots -$ overall gear ratio from the motor to the actuating device.

The equation of the power capacity can be written in the following way, thanks to the efficiency - in the system.

$$\mathrm{M_C}\omega_1 = M_{\text{мех}}\omega_{\text{мех}}\eta_{\text{мех}} - \Delta\mathrm{M}\omega_1 \qquad (8)$$

In this case:

$$\mathrm{M_C} = (\mathrm{M_{мех}}/i_0)\eta_{\text{мех}} - \Delta M. \qquad (9)$$

The moment caused by mechanical losses in the engine isn't bigger then 1-5 % of the rated torque of the engine. In this case we assume $\Delta M \approx 0$, and $\mathrm{M_{мех}}$ becomes:

$$\mathrm{M_C} = \mathrm{M_{мех}}/i_0\eta_{\text{мех}}; \qquad (10)$$

For motor rotating in the opposite direction:

$$\mathrm{M_C} = (\mathrm{M_{мех}}/i_0)\eta_{\text{мех}} \qquad (11)$$

When $\Delta\mathrm{M} = 0$, the equation can be written:

$$M_C\omega_1 = F_{\text{мех}}v_{\text{мех}}/\eta_{\text{мех}} \qquad (12)$$

From where:

$$\mathrm{M_C} = (F_{\text{мех}}/\eta_{\text{мех}})\mathrm{p} \qquad (13)$$

So for motor rotating in the opposite direction:

$$\mathrm{M_C} = F_{\text{мех}}\mathrm{p}\eta_{\text{мех}} \qquad (14)$$

From the kinematic chain in fig. 4 we can write the current example the three most - significant masses are given the rotor, the engine with inertia moment $J_{\text{дв}}$ and load J_c.

$$1/C_{\text{екв}} = 1/C_1 + 1/C_2 + 1/C_3 + \dots \text{(15)[8]}$$

The behavior of the system depends on the variable parameter T_M to get the required quality of the transition process. [1]

The algorithm taking into account the variable mechanical time constant. Is calculated and explained in [1].

Electromechanical time constant is:

$$T_M = \frac{J_{\Sigma.} r_e}{(c\Phi)^2}; = c\Phi = \frac{M_H}{I_H}; \quad (16)$$

$$J_{\Sigma.} = J_{дв} + J_P + J_{CM1} + \frac{J_C}{\eta_{мех}\, i_p^2}; \quad (17)$$

$$J_C = \frac{GD^2}{4g}; J_P = 0{,}2J_{дв}; J_{\Sigma.} = 1{,}2J_{дв} + J_{CM1} + \frac{GD^2}{4g\eta_{мех}\, i_p^2}; \qquad G = G_C + G_П; \quad (18)$$

Where:

$J_{дв}$ – motor inertial moment,

J_{CM1} – inertial moment, perifleks coupler.

J_P – inertial moment of the profiled designed gear,

J_c – inertial moment of the load,

i_p – ratio of the gearbox,

η_{MEX} – efficiency,

From the made calculations it is seen that with the change of the T_M disturbing the optimal setting of the internal and external contour. Fig. 5 and Fig. 6 shows the dependencies between dynamic moment and the parameters G and R.

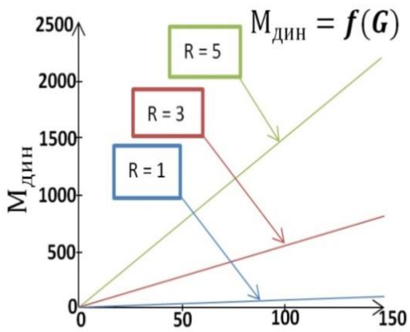

Fig. 5. $M_{дин} = f(G)$, when $\varepsilon = 6$

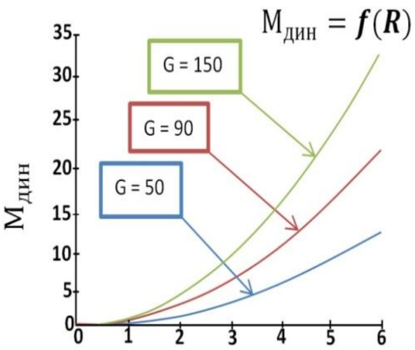

Fig. 6. $M_{дин} = f(R)$, when $\varepsilon = 0{,}6$

The dependence of the dynamic moment and of the two parameters (G and R) is given in Fig. 7.

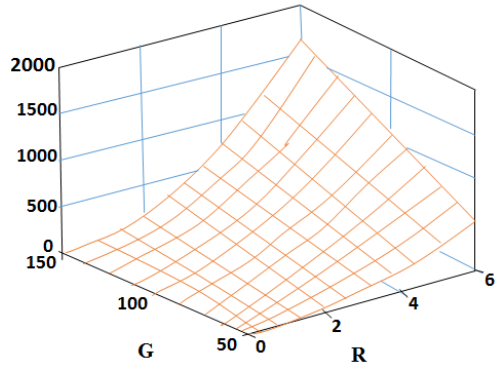

Fig. 7. Dependence of the dynamic moment and of the two parameters (G and R)

2. CONCLUSION

With the applied optimization, the system reliability is increased, noise levels fall due to the applications of perifleks coupler and repair suitability significantly increased due to the lack of belt drive. Because of the absence of belt drive the period for external intervention significantly increases, the system can operate a long time, as independent. From the economical point of view, the price dropped because it is not necessary to purchase a belt drive and repair costs are also drastically reduced. The overall friction in the system is also decreased.

References

[1] Bakardjiev D., BC Bakardjiev, D. Angov M. Zhilevski, management kupolometar to study the vestibular system, Proceedings of the Technical University of Rousse, Scientific and technical conference with international participation, 2005.

[2] Bakardjiev D., Zhilevski M. Bakardjiev Hr., Zhilevska M. Kochevska V. Zhilevski M., Management swivel chair for Medical Research Generation IV, Science University of Rousse Volume 48 3.1 series, 2009.

[3] The electronic textbook "Machine elements - Part I" is the first revised edition of the textbook "Machine elements" Publishing-VVTU "T.Kableshkov", Sofia, 1997.

[4] Mihov M., Electromechanical Systems Control - Part II, TU 2009

[5] Theory of electric VI key, Moscow Energoatomisdat 2001 BBK 31,191, K 52, 62-83 UDC (075.8)

[6] The total electric rate, MG Chilikin, AS Sandler, Moscow Energoizdat 1981.

[7] Machine Parts, G.Angelov, fourth edition, CI,, TECHNOLOGY "Sofia - 1964

[8] Calculation and design of machine elements, D. Hristov D. Petkov, N. Chavushtyan S. Nachev, M. Prodanov Technique. Sofia. 1967 year.

OPTIMIZATION OF THE PARAMETERS OF THE MECHANICAL GEAR IN MEDICAL CENTRIFUGE (CHAIR OF BARANY)

Ts. Kachamachkov, D. Bakardzhiev, Hr. Bakardzhiev, V. Manoev

Technical University of Sofia, Bulgaria,

E-mails: eng_kachamamachkov@abv.bg; dim_bak@abv.bg; vmanoev@tu-sofia.bg

Abstract

We researched the influence of the mass, diameter and the structure of the mechanics on the moment of inertia, the mechanical time constant and the coefficient of efficiency for a class of the mechanisms. We offer, a specific solutions to optimize the mechanical units in medical centrifuge (chair of Barany) by these parameters: mechanical time constant, volume, weight, power, efficiency. Studies have been conducted for several mechanisms in order to find the optimal structure for the chair of Brany.

Keywords*: mechanism, mechanical units, efficiency, mechanical time constant, volume, weight, power, chair of Barany.*

INTRODUCTION

The subject of the research in this work are the mechanical parts that make the mechanism of the rotating chair for studies of the vestibular system [1], [2]. Typical of it is that you have to provide a trapezoidal speed chart and sinusoidal oscillation, pendulous effect and stop impetus.

Representation

The chair is designed for responsible research in the vestibular system for civilian patients and pilots the electromechanical part is shown on Figure 1. It must provide the necessary conditions for the tests: The values of accelerations are strictly defined 0,06; 0,2; 0,8; 1,0; 3,0; 6,0; 9,0; 10,0; 15,0; 20,0; ${}^{o}/_{s^2}$, or 0,001; 0,0035; 0,014; 0,0174; 0,1047; 0,157; 0,174; 0,262; 0,35 ${}^{rad}/_{s^2}$.

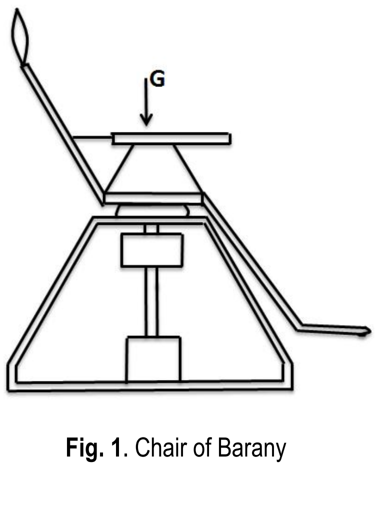

Fig. 1. Chair of Barany

The mechanical part comprises from:

1 - chair; 2 - electric motor; 3 - reducer;

For the sake of high efficiency we offer the following structural changes: standard, gearbox and engine are replaced by specifically designed for chair of Barany. Their production is justified by the wide-spread obtained by the chair of Barany over the past century. The mechanical part incorporates all interrelated moving masses or with other words engine, gearbox and actuator shown in Fig. 2. Motion is implemented by the engine Д, reducer КРП, perifleks coupling CM1, propels the mass m1 and patient with mass m2. Loading Actuator moves cargo m1 + m2.[3]

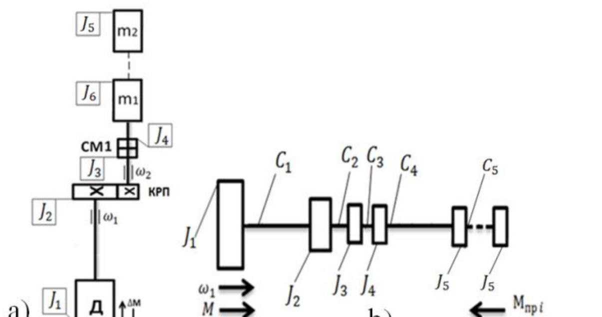

Fig. 2. Schematic diagram of the mechanical part a) and defined kinematic chain b) of medical centrifuge.

On the diagram in Fig. 2 with arrows are shown the applied to the individual mases in the system, adduced moments of the active in the system external forces $M_{\text{пр}\, i}$ and $\mathrm{M}_{\text{пр}\, j}$. To the rotor of the engine J_1 is applied the electromagnetic moment of the engine M and the moment of the mechanical es ΔM, to properly calculate we assumed to be positive sign the direction of the angular velocity ω_1. In simplifying of the scheme it is necessary to calculate all externally applied forces on the masses which are connected by means of solid bodies. The study of the dynamics of the electric drive shows that the direct calculation of mechanical scheme in most cases gives the same output as the detailed calculation of the individual forming mechanism. Therefore we identify the main masses and stiffness and bring it down to a two mass system shown on fig. 3, where the system is broth down to the unit with the lowest stiffness and result inertial momentum.[4]

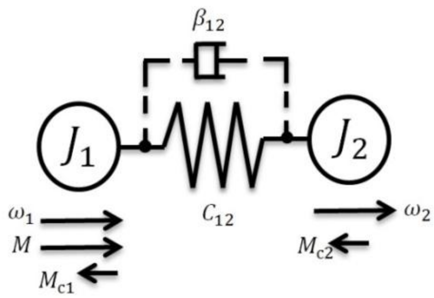

Fig. 3. Summarized two - mass scheme for medical centrifuge

Parameters of two – mass flexible mechanical system (fig. 3), are reduced to the total moment of inertia moments J_1 and J_2, directed to the mechanical connection between them. We accept the moment of elasticity which is brought to the stiffness of a mechanical link J_1 and $J_2 - C_{12}$. The first mass represents the rotor of the engine himself and the mechanical components which have direct contact with him. To this we add the applied electromagnetic moment of the engine M and the moment of static load $\mathrm{M_{c1}}$. To the intermediate masses in the mechanism J_2 is applied the resistance moment M_c. In calculating the above-quoted static moment M_C, when all active forces and momentums in the mechanism are defined. In most cases, losses from friction in the mechanism are unknown and are calculated with the use of the efficiency coefficient of the mechanism. [4]

$$\eta_{\text{мех}} = \eta_1\eta_2\eta_3 \ldots, \qquad (1),[6]$$

Where $\eta_1, \eta_2, \eta_3 -$ are efficiency coefficients of the units in the kinematic chain.

If the moment $\mathrm{M_{MEX}}$ of the load in the mechanism is positive, the moment of the static load is detriment from the equations. [4],[5]

$$\mathrm{M_C}\omega_1 = \mathrm{M_{мех}}\omega_{\text{мех}}/\eta_{\text{мех}} + \Delta\mathrm{M}\omega_1 \qquad (2)$$

Therefore

$$\mathrm{M_C} = \mathrm{M_{мех}}/i_0\eta_{\text{мех}} + \Delta M, \qquad (3)$$

Where $\Delta M -$ is the moment of mechanical losses in the engine.

$i_0 = \frac{\omega_1}{\omega_{\text{MEX}}} = i_1 i_2 i_3 \ldots -$ overall gear ratio from the motor to the actuating device.

The equation of the power capacity can be written in the following way, thanks to the efficiency - in the system.

$$\mathrm{M_C}\omega_1 = M_{\text{мех}}\omega_{\text{мех}}\eta_{\text{мех}} - \Delta\mathrm{M}\omega_1 \qquad (4)$$

In this case:

$$\mathrm{M_C} = (\mathrm{M_{мех}}/i_0)\eta_{\text{мех}} - \Delta M. \qquad (5)$$

The moment caused by mechanical losses in the engine isn't bigger then 1-5 % of the rated torque of the engine. In this case we assume ∆M≈0, and $\mathrm{M_{мех}}$ becomes:

$$\mathrm{M_C} = \mathrm{M_{мех}}/i_0\eta_{\text{мех}}; \qquad (6)$$

For motor rotating in the opposite direction:

$$\mathrm{M_C} = (\mathrm{M_{мех}}/i_0)\eta_{\text{мех}} \qquad (7)$$

When $\Delta\mathrm{M} = 0$, the equation can be written:

$$M_C\omega_1 = F_{\text{мех}}v_{\text{мех}}/\eta_{\text{мех}} \qquad (8)$$

From where:

$$\mathrm{M_C} = (F_{\text{мех}}/\eta_{\text{мех}})\mathrm{p} \qquad (9)$$

So for motor rotating in the opposite direction:

$$\mathrm{M_C} = F_{\text{мех}}\mathrm{p}\eta_{\text{мех}} \qquad (10)$$

From the kinematic chain in fig. 4 we can write the current example the three most - significant masses are given the rotor, the engine with inertia moment $J_{\text{дв}}$ and load J_c.

$$1/C_{e\text{кв}} = 1/C_1 + 1/C_2 + 1/C_3 + \ldots \quad (11)[7]$$

The behavior of the system depends on the variable parameter T_M to get the required quality of the transition process. [1] The algorithm taking into account the variable mechanical time constant. Is calculated and explained in [1].

Electromechanical time constant is:

$$T_M = \frac{J_{\Sigma.} r_e}{(\text{с}\Phi)^2}; = \text{с}\Phi = \frac{\text{М}_\text{Н}}{I_\text{Н}}; \qquad (12)$$

$$J_{\Sigma.} = J_{\text{дв}} + J_P + J_{CM1} + \frac{J_C}{\eta_{\text{мех}}\, i_p^2}; \qquad (13)$$

$$J_C = \frac{GD^2}{4g}; J_P = 0{,}2J_{\text{дв}}; J_{\Sigma.} = 1{,}2J_{\text{дв}} + J_{CM1} + \frac{GD^2}{4g\eta_{\text{мех}}\, i_p^2}; G = G_C + G_\Pi; \qquad (14)$$

Where:

$J_{\text{дв}}$ – motor inertial moment,

J_{CM1} – inertial moment, perifleks coupler.

J_P – inertial moment of the profiled designed gear,

J_c – inertial moment of the load,

i_p – ratio of the gearbox,

η_{MEX} – efficiency,

In this current example it is shown the parameters of the gear of medical centrifuge used in the of Barany.

Reducer used at the moment.

- transmission ratio i = 63
- rotational speed of the input n_1=1512 min^{-1}
- rotational speed of the output shaft $n_n = 24\, min^{-1}$
- transmitted rated power (output) P = 400 W
- the number of teeth of the worm wheel Z_2 = 63
- input torque $T_1 = 3{,}7\, N.m$
- output torque $T_2 = 119{,}4\, N.m$
- the axle spread a = 52 mm
- the functional length of the worm wheel $b_1 = 62\, mm$
- superlative diameter $d_2 = 82\, mm$
- width of the worm wheel $b_2 = 25{,}2\, mm$
- the distance between the bearings and the worm shaft l1 = 157 mm
- the distance between the bearings l_2 = 108 mm

Reducer designed for chair of Barany

- transmission ratio i = 88
- rotational speed of the input n_1= 3000 min^{-1}
- rotational speed of the output shaft $n_n = 34\, min^{-1}$
- transmitted rated power (output) P= 270 W
- the number of teeth of the worm wheel Z_2 = 88 бр.
- input torque $T_1 = 1{,}3\, N.m$
- output torque $T_2 = 76\, N.m$
- the axle spread a = 10 mm
- the functional length of the worm wheel $b_1 = 65\, mm$
- superlative diameter $d_2 = 36\, mm$
- width of the worm wheel $b_2 = 8{,}5\, mm$
- the distance between the bearings and the worm shaft l_1 = 40 mm
- the distance between the bearings l_2 = 64 mm

Determine the required power of the electric motor

$$P_{\text{ел}} = \frac{P_{\text{изх}}}{\eta_{\text{мех}}} \qquad (15)[7]$$

Where:

$P_{\text{изх}}$ – Output power

$\eta_{\text{мех}}$ – Efficiency of the system

$P_{\text{ел}}$ – rated power of the electric motor.

$$d = \text{m.q} \qquad (16)$$

Where:

m – Modules of engagement of the worm gearing.

q – Coefficient of the diameter of the worm.

$$d_2 = \sqrt[3]{\frac{T_2}{0{,}2.\tau_{\text{доп}}}} \qquad (17)$$

Where:

$\tau_{\text{доп.ус}}$ – is allowable tension twist.

T_2 – output torque.

d – the diameter of the outlet end of the worm wheel shaft.

Comparative analysis on parameters in % of change from previous to current.

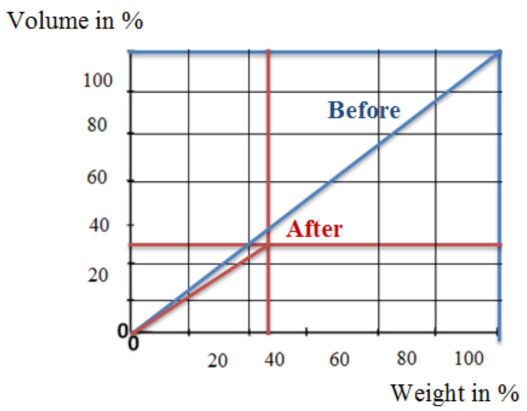

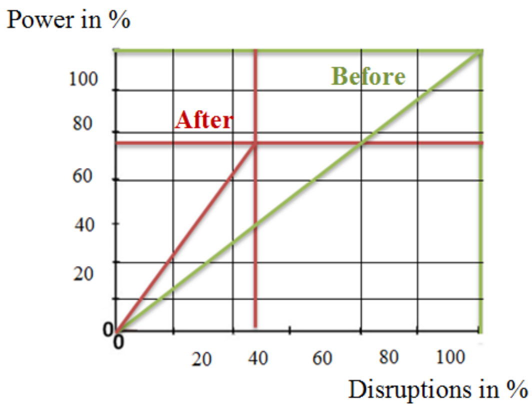

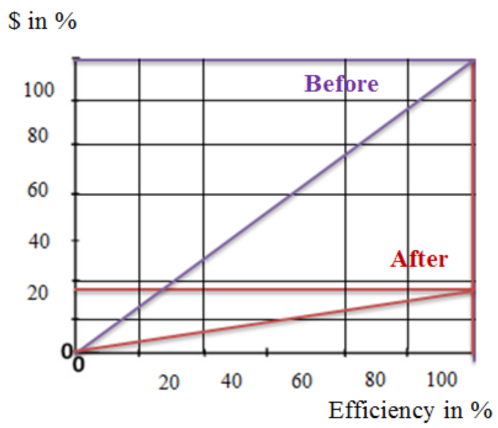

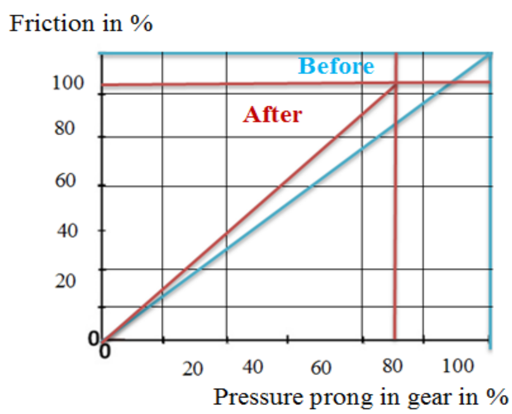

CONCLUSION

In applying the designed gearbox, friction in the system is reduced the volume of the used gear is reduced, weight decreased, the power required to drive also falls, the money required for production drops.

References

[1] Bakardjiev D., B. C. Bakardjiev, D. Angov M. Zhilevski, management kupolometar to study the vestibular system, Proceedings of the Technical University of Rousse, Scientific and technical conference with international participation, 2005.

[2] Bakardjiev D., Zhilevski M. Bakardjiev Hr., Zhilevska M. Kochevska V. Zhilevski M., Management swivel chair for Medical Research Generation IV, Science University of Rousse Volume 48 3.1 series, 2009.

[3] Theory of electric VI key, Moscow Energoatomisdat 2001 BBK 31,191, K 52, 62-83 UDC (075.8)

[4] Теория электропривода В. И. Ключев, Москва энергоатомиздат 2001 г. ББК 31.191, К 52, УДК 62-83(075.8)

[5] The total electric rate, M. G. Chilikin, A. S. Sandler, Moscow Energoizdat 1981.

[6] Machine Parts, G. Angelov, fourth edition, CI,, TECHNOLOGY "Sofia - 1964

[7] Tasks and course design theory of mechanisms and machines, Eng. Tcanko K. Nedev, Eng. Alexander G. Vrigazov, Eng. Mihail I. Milkov State Publishing House,, Technique "Sofia 1963.

ANALYSIS OF IMPULSE RESPONSE MEASUREMENT SIGNALS USED IN ROOM ACOUSTIC

Snejana Pleshkova-Bekiarska, Stanislav Filipov

Department of Telecommunications,
Technical University - Sofia, Kliment Ohridski 8, Sofia

snegpl@tu-sofia.com

Abstract

A test measurement signals are used to examine the acoustic ambience in open acoustic spaces where combined noise sources exist. Using different test signals and approaches we can measure the reverberation time in any premises. These test signals can be different type and we will observe which signal is the most suitable for exact room. Early acoustic measurement was made by complicated and heavy tube equipment which not always gives the proper results. Also the measurement microphones were not so sensitive for small acoustic fluctuations and artifacts. Generally one modern acoustic measurement system is built up from isotropic sound source called dodecahedron, music interface, measurement amplifier, Omni microphone and acoustic software. However, using this set up we can measure reverberation time and other acoustic parameters via test signals like periodic or white noise, sweep signal and maximum length sequence - MLS. Further researches shows that using the described signals we can reach very high accuracy. In this topic we will look at the modern test signals and compare them.

Keywords: *acoustic measurement, open acoustic space, impulse response, reverberation time, acoustic ambience, test signals, periodic noise, swept-sine, MLS.*

1. INTRODUCTION

The acoustic parameters of any room can be obtained from impulse response of the room via real-time spectrum analysis and measurement of the frequency response. There are many tools for acoustical measurements which can deliver accurate results but usually they are sophisticated software programs with many features. Each software tool used for measurements of acoustic ambience should have the follow main features or options:

- Option for measurement of impulse response
- Option for measurement of frequency response
- Built in spectrum analyzer

The frequency response measurement is a major feature and it's based on the classical Fourier analysis which states that every time signal with a finite energy has a corresponding Fourier transform [1, 2, 7]. In a system analysis we assume that linear time-invariant (LTI) system – Fig.1 is excited with a signal *x(t)* and on output has a signal *y(t).* Both signals *x(t)* and *y(t)* have corresponding Fourier transforms *X(f)* and *Y(f).*

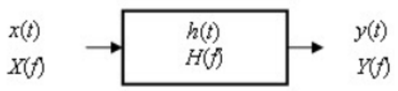

Fig.1. LTI system

The principle of the impulse response measurement is the same as in the Fourier analyzer that we will check later. Only difference is that the impulse response measurement is a non-real time measurement which we will see during our tests.

The spectrum analyzer is convenient option where you can monitor real time fluctuations of the sound pressure level and other events related to frequency domain.

Looking back in the analogous time we will see that the major technique for acoustic measurement uses some type of periodic noise usually pink or white. The benefits from this are that we receive information for the acoustic ambience in whole audio range which is fully enough to analyze the room in frequency or time domain [4,5]. Of course the results in time domain are more complicated and insist more complex calculations where you can easily make a mistake and compromised the results. That's why during the 90's were developed new more precise digital test signals to help downsizing the amount of data and to improve efficiency. Generally two new signals for measurement were implemented – Swept-sine and MLS excitation.

Of course the good old one periodic noise signal was not forgotten. The researches show that he can be adjusted to perfection and more options regarding his spectrum can be added [9,10]. One of these new options is the possibility to generate periodic noise with speech spectrum which is used to measure any premises like open acoustic spaces, offices, rail way terminals and many more.

Let's get back in the digital era and impulse response and to make the conclusion that there are three main types of measurement excitation:

1) Impulse Response Measurement with Periodic Noise Excitation
2) Impulse Response Measurement with Logaritmic Swept-sine technique
3) Impulse Response Measurement with MLS Excitation
4) Impulse Response Measurement with IRS technique.

2. IMPULSE RESPONSE THEORY

The relationship between the input and the output of an LTI system, in the frequency domain, can be expressed as:

$$Y(f) = X(f)*H(f), \tag{1}$$

Where the complex function *H(f)* is called a frequency response:

$$H(f) = \frac{Y(f)}{X(f)} = |H(f)|e^{j\varphi(f)}, \tag{2}$$

H(f) is termed magnitude response, and *φ(f)* is termed phase response. The frequency response shows how the system changes the magnitude and phase spectrum of an input signal.

The inverse Fourier transform of frequency response *H(f)* is a function *h(t)* and it is a system impulse response. We show it by following reasoning. The product *X(f)*H(f)* has a Fourier pair in the time domain defined by the convolution $x(t)\otimes h(t)$. This convolution is equal to the output signal *y(t):*

$$y(t) = x(t)\otimes h(t) = \int_{-\infty}^{\infty} h(\tau)x(t-\tau)d\tau, \tag{3}$$

Where the function *h(t)* is called impulse response of the system, as it is a system response to an impulse *δ*-function excitation. It is obvious, as by analyzing the convolution $\delta(t)\otimes h(t)$, we get:

$$h(t) = \int_{-\infty}^{\infty} h(\tau)\delta(t-\tau)d\tau, \tag{4}$$

The system frequency response is usually estimated by using the input-output cross-spectrum and the input auto-spectrum. By rewriting the expression for the transfer function in the following form:

$$H(f) = \frac{Y(f)}{X(f)} = \frac{Y(f)X'(f)}{X(f)X'(f)} = \frac{S_{xy}(f)}{S_{xx}(f)}, \tag{5}$$

We can get the frequency response by dividing an input-output cross-spectrum with an input auto-spectrum (star denotes the complex conjugate value). This equation is usually called *H1* estimator. Fourier transform pairs of the cross-spectrum *Sxy(f)* and the input auto-spectrum *Sxx(f)* are the cross-correlation *Rxy(t)* and the auto-correlation *(Rxx(t))*, i.e.

Rxy(t) ⇔ *Sxy(f) – cross-correlation*

Rxx(t) ⇔ *Sxx(f) – auto-correlation*

If the system input has a white spectrum *(Sxx(f)=1)*, then *Rxx(t)=δ(t)*, the impulse response is equal to the input-output cross-correlation.

$$h(t) \approx Rxy(t), \tag{6}$$

if the input has white spectrum.

Using the *H1* estimator for the frequency (and impulse) response estimation is important, as it will be shown that this estimator has good properties in reducing the influence of the noise and distortions..

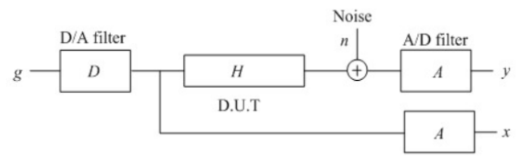

Fig. 2. Measurement setup of dual channel system

Fig.2 shows the measuring system that is typical for acoustical measurements. The computer generate signal – g and after D/A filtering with transfer function D, the signal is applied to the test system that has the transfer function H. Note that H represents the best linear fit of the possible nonlinear transfer function. The noise generator is neglected. The output from the test device (D.U.T), together with the additive system noise n, is acquired by the computer as a discrete signal sequence y. The acquisition process implies the use of an antialiasing filter that has the transfer function A.

3. GENERAL STRUCTURE AND EXCITATIONS TYPES IN DUAL CHANNEL SYSTEMS

3.1. Continuous noise excitation

In a classical Fourier analyzer the excitation is a random noise and the frequency response is estimated by dividing the averaged cross-spectrum *X*Y* with the averaged auto-spectrum *X*X* of *N* input and output discrete sequences *xi* and *yi*. We define the *H1* estimator as:

$$H_e(w) = \frac{\sum_{i=1}^{N} Yi(f)X'(f)}{\sum_{i=1}^{N} Xi(f)X'(f)} = \frac{<Sxy(f)>}{<Sxx(f)>}, \quad (7)$$

Where *He(w)* denotes the estimated frequency response and the brackets < > denote the averaged value. The (7) describes the dual channel system with continuous noise excitation. The *H1* estimator gives a biased estimate of the real transfer function *H(f)*, which is dependent on the noise, distortions and the delay between input and output channel. When only the noise contributes to the bias, the effect of averaging can be expressed by the equation:

$$H_e(f) \cong H(f) + \frac{\sqrt{n} < Ns(f)A(f)X'(f) >}{n < X'(f)X(f) >} \cong$$

$$\cong H(f) + \frac{1}{\sqrt{n}} \frac{< Ns(f)G'(f) >}{< G(f)G'(f) >} \frac{D'(f)}{|D(f)|^2}, \quad (8)$$

Note that signal term is summed coherently, while the stochastic part of the noise is power summed.

The conclusion is that averaging lowers the noise level proportionally with a square root of number of averages, thus improving the measurement S/N by 10log(n). If nonlinear distortions are present, then part of the system noise is coherent with a generated signal and a better measure for the proportionality of the noise + distortion and a number of averages are $1/\gamma\sqrt{n}$, where γ is the input-output coherence function, defined as:

$$\gamma^2 = \frac{|< Sxy(f) >|^2}{< Sxx(f) >< Syy(f) >}, \quad (9)$$

The coherence function is a measure of the proportion of the power in *y* that is due to linear operations on the signal *x*. When estimating the transfer function, the coherence function is a useful check on the quality of data used. The maximum value of coherence is 1. Sometimes we can display the coherence, so it is possible to check the coherence associated with "double channel" measurements. Practically, we must have γ^2 close to 1 to ensure the good estimation, but we must keep in mind that coherence has a sense only if the number of averages is greater than 1.

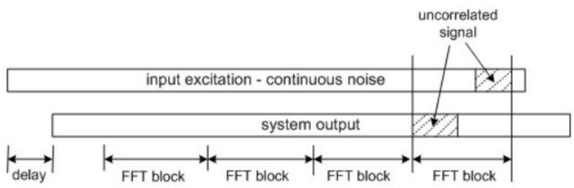

Fig. 3. Uncorrelated estimation in a classical Fourier analyzer

Of course there are some problems in a classical Fourier analyzer with the continuous noise excitation because of:

- The excitation signal does not have constant spectrum at all frequency bins. This gives the frequency selective noise bias. It is high at frequencies where generator spectrum has notches. This resolution bias can be greatly reduced by increasing the number of averaging cycles. It is recommended to make at least 6 spectrum averages and monitor the coherence function.
- In a system with a large delay between the input and the output (Fig.3), i.e. when measuring the loudspeaker in room response, there will be low correlation between measured input and output signals. In some tools it is possible to delay the acquisition of the input channel, so this kind of error can be eliminated. But, if we measure the frequency response in the highly reverberant environment, it is not possible to compensate for all possible delays.

Both problems can be eliminated by using the periodic noise excitation.

3.2. Periodic noise excitation

If the excitation is done with *N* different periodic noise sequences, the frequency response estimator can also be of the form:

$$H_e(f) = \frac{1}{N}\sum_{i=1}^{N}\frac{Yi(f)X'(f)}{Xi(f)X'(f)}, \quad (10)$$

This type of averaging is called the frequency domain asynchronous averaging. Theoretically it has the same power in reduction of the noise and distortions as the *H1* estimator, but the use of the *H1* estimator is preferred as it enables us to monitor the coherence function.

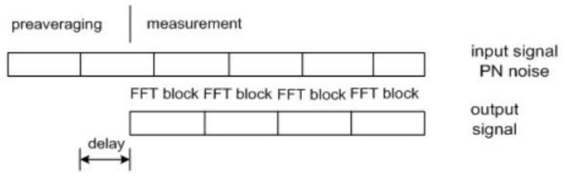

Fig.4. Signal generation during the time domain synchronous averaging process

If the excitation is done with a single periodic sequence, repeated *N* times (Fig.4), the estimator can be of the form:

$$\begin{aligned} &y^{-}(t)\sum_{i=1}^{N} yi(t) \\ &x^{-}(t)\sum_{i=1}^{N} xi(t) \\ &H_e(w) = \frac{^{-}Y(f)^{-}X'(f)}{^{-}X(f)^{-}X'(f)} \end{aligned} \quad (11)$$

This type of averaging is called the time domain synchronous averaging. This estimator reduces the system random noise, but it can't reduce nonlinear distortions and the stationary noise that is periodic within the excitation period.

When measuring in reverberant environment the period of the multi-sine must be greater than the reverberation time - T60. The following reasoning can approve this requirement. The room acoustical response has the bandwidth of resonance peaks equal to 2.2/T60. If we choose that a frequency difference between two multi-sine component is less than half of this value, to allow built up of all room resonances, we can conclude that period of the periodic noise have to be equal or greater than the reverberation time. Also, it follows that length of the pre-averaging cycle must be greater or equal to the reverberation time.

3.3. MLS and IRS techniques

The impulse response measurements using the MLS technique were first proposed by Schroeder [!] in 1979 and have been used for more than thirty years. The measurement with MLS technique is based upon the excitation of the acoustical space by a periodic pseudo-random signal having almost the same properties as the white noise. The number of samples of one period of an *m* order MLS signal is: $L = 2m - 1$.

With the MLS technique, the impulse response is obtained by circular cross-correlation between the measured output and the determined input (MLS sequence). Because of the use of circular operations to de-convolve the impulse response, the MLS technique delivers the periodic impulse response *h'[n]* which is related to the linear impulse response by the following equation:

$$h'[n] = \sum_{l=-\infty}^{\infty} h[n + lL], \quad (12)$$

This equation reflects the major problem of the MLS technique: the time-aliasing error. This error is significant if the length *L* of one period is shorter than the length of the impulse response to be measured.

While the MLS is fighting with the distortion artifacts caused by distortion peaks the IRS technique uses sequence with a *2L* samples period *x[n]* is defined from the corresponding MLS sequence of period *L(mls[n])* by the following relation:

$$x[n] = \begin{cases} mls[n],\ \textit{if n is even, } 0 \le n \le 2L \\ , \\ -mls[n],\ \textit{if n is odd, } 0 < n < 2L \end{cases} \quad (13)$$

The deconvolution process is exactly the same as for the MLS technique.

3.4. Impulse response measurement with logaritmic swept-sine technique

The MLS, IRS and Time-Stretched Pulses methods are based on the assumption of LTI systems and cause distortion artifacts to appear in the deconvolved impulse response when this condition is not fulfilled.

The Swept-Sine technique was developed by Farina ([!]) eliminate these limitations. It is based on the idea by using an exponential time-growing frequency sweep. This means that it is possible to simultaneously deconvolve the linear impulse response of the system and to selectively separate each impulse response corresponding to the harmonic distortion orders considered. The harmonic distortions appear prior to the linear impulse response. Therefore, the linear impulse response measured is assured exempt from any non-linearity and, at the same time, the measurement of the harmonic distortion at various orders can be performed.

In mathematical manner the Swept-sine signal is defined as a sine signal *g(t)* with a time varying phase function *φ(t):*

$$g(t) = \sin(2\pi\varphi(t)), \tag{14}$$

where the frequency of this signal is defined as:

$$f(t) = \frac{d\varphi(t)}{dt}, \tag{15}$$

If we have logarithmic swept-sine according to Farina the phase function of this signal is:

$$\varphi(t) = \frac{f_1 T}{\ln \frac{f_2}{f_1}} \left(e^{\frac{t}{T}\ln f2/f1} - 1\right), \tag{16}$$

Where *f1* is the start frequency, *f2* is the end frequency and *T* is the duration of the signal.

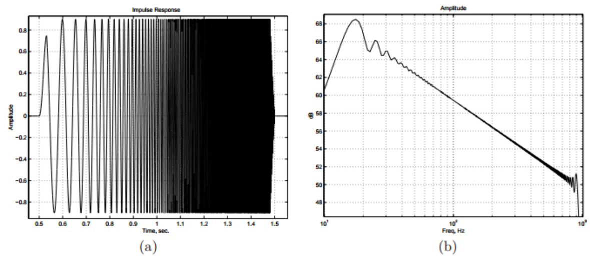

Fig. 5. (a) Time domain representation of logarithmic swept-sine signal, (b) Amplitude representation

4. ACOUSTICAL CHARACTERISTICS, MEASUREMENT SETUP AND COMPARASION OF METHODS AND ALGORITHMS USED IN IMPULSE RESPONSE MEASUREMENTS

4.1. Measurement block diagram

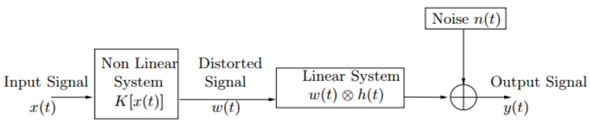

Fig. 6. Nonlinear system (speaker) and LTI measurement system

As for nonlinear system is used Philips AH587 MFB Studio monitor and for LTI is used omnidirectional microphone, Roland professional interface UA-25 and Arta with 64 bit FFT.

Fig. 7. The legendary Philips 22AH587

Fig. 8. Cost effective solution Behringer ECM-8000

4.2. Measurement Setup

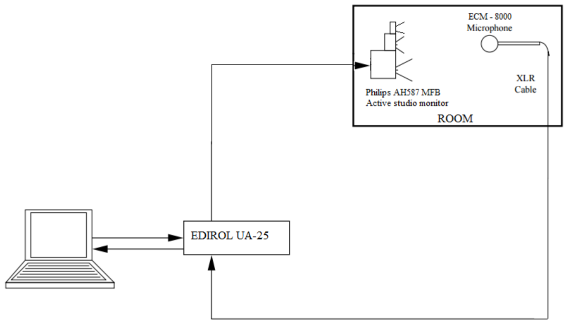

Fig. 9. Measurement setup in casual room

5. RESULTS

Our measurements and tests will be performed in non-anechoic room to see the practical side of the impulse response measurement. According the expression in the previous chapter we will extract the reverberation time from impulse response of all measurements to see what the differences are. Also don't forget that Philips 22AH587 studio monitor is closed box with MFB driver and this can control the room resonances in normal limits.

The test conditions for all measurements will be:

- Sampling frequency – 48 kHz
- Bit resolution – 24bit
- Time constant - 5461.31msec (duration of emitted signal)
- Sequence length – 16k, 64k, 256k, 262k only for MLS
- Number of Averages – 3 (number of times the emitted signal will be send to the monitor)
- Noise level at mic position – MLS-60dBA, Swept-Sine – 80dBA, Periodic noise – 78dBA.

5.1. Periodic noise speech spectrum – sequence length 16k

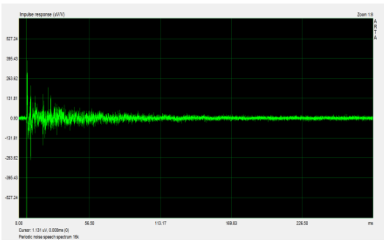

Fig. 10

5.2. Periodic noise speech spectrum – sequence length 64k

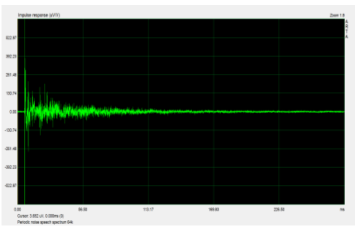

Fig. 11

5.3. Periodic noise speech spectrum – sequence length 256k

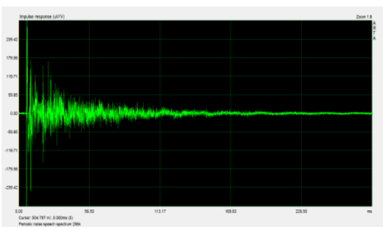

Fig. 12

5.4. MLS – sequence length 16k

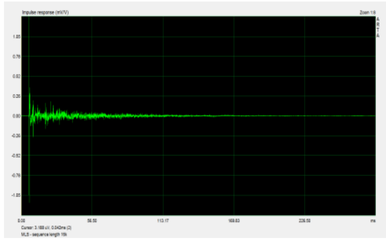

Fig. 13

5.5. MLS – sequence length 65k

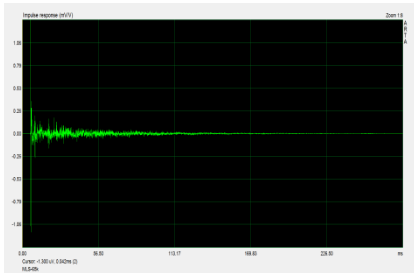

Fig. 14

5.6. MLS – sequence length 262k

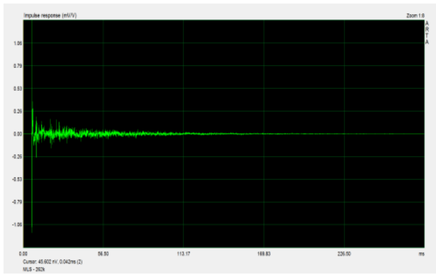

Fig. 15

5.7. Swept-sine – sequence length 16k

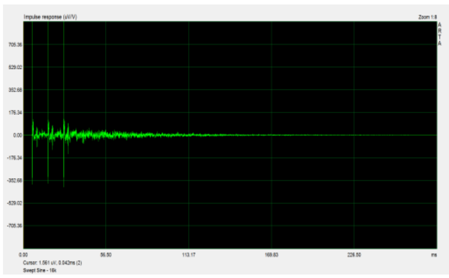

Fig. 16

5.8. Swept-sine – sequence length 64k

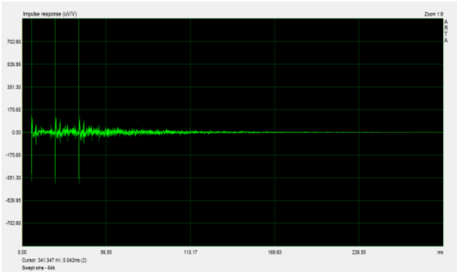

Fig. 17

5.9. Swept-sine – sequence length 256k

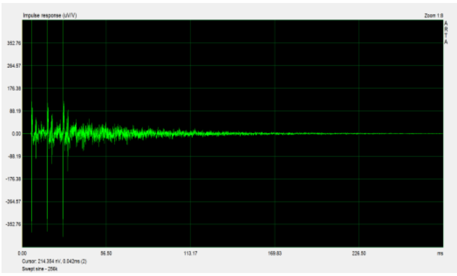

Fig. 18

Analysis

The MLS method seems the hardest method when the measurements have to be performed in a casual non soundproofed room due to its strong defense to all kinds of noise (impulse or background). If we look at Fig.13, 14, 15 we can find that the three measurements are almost identical without big differences. Also the tail of the impulse response compared to the other two methods is very short which shows the protection of any others ambient noises. However, its major drawback is the laggard calibration that has to be done to receive optimal results and the second drawback is in the appearance of distortion peaks due to the inherent non linearity of the measurement system.

That's why if we want to extricate the distortion peaks we can use periodic noise method which avoids the appearance of the distortion peaks. Anyway, the remaining non-linear artifacts can possibly be overlay with the de-convolved "linear" impulse response. The presence of a residue of the excitation signal in the de-convolved impulse response is a result of such superposition problem. This residue can be completely eliminated with a precise calibration of the measurement microphone which we done with pulsar calibrator. However, the main disadvantage in this method comes from its timbre and the high value of the output signal level (see the big tail Fig.10, 11, and 12) needed to mask out the ambient noise. This makes it unusable in occupied rooms.

At last the perfect and complete rejection of the harmonic distortions prior to the "linear" impulse response and the excellent signal-to-noise ratio of the Swept-Sine method make it the best impulse response measurement technique in an non occupied and quiet room. Moreover, unlike the preceding methods, it does not insist a complicated calibration in order to receive good results (no compromise between the signal-to-noise ratio and the superposition of nonlinear artifacts in the room impulse response). Anyway, as for the periodic noise method, the Swept-Sine technique is not recommended for measurements in occupied rooms.

T30 - Reverberation time

The reverberation time – T30 is collected from the measurements of above impulse responses and plotted separately, but why T30 and not T60? In many books is written that the reverberation time is defined as a time interval required for the sound energy to decay 60 dB after the excitation signal has stopped. This is because in ARTA the T30 is defined according to the ISO 3382 and the ISO defines that the T30 is the reverberation time determined from the average slope of the energy decay curve obtained from part of the decay curve between -5dB and -35dB.

5.10. Periodic noise speech spectrum – sequence length 16k

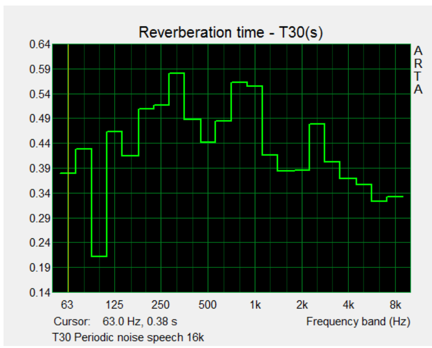

Fig. 19

5.11. Periodic noise speech spectrum – sequence length 64k

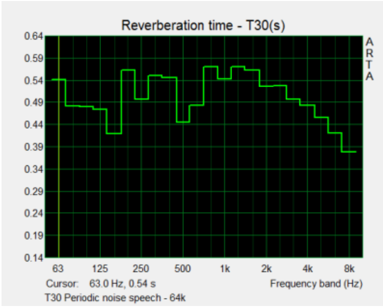

Fig. 20

5.12. Periodic noise speech spectrum – sequence length 256k

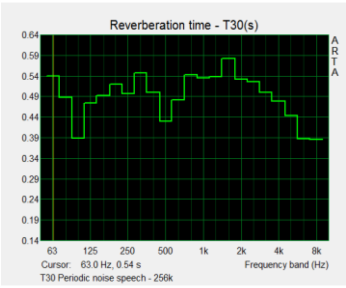

Fig. 21

5.13. MLS – sequence length 16k

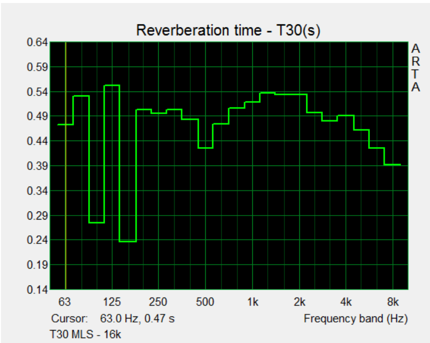

Fig. 22

5.14. MLS – sequence length 64k

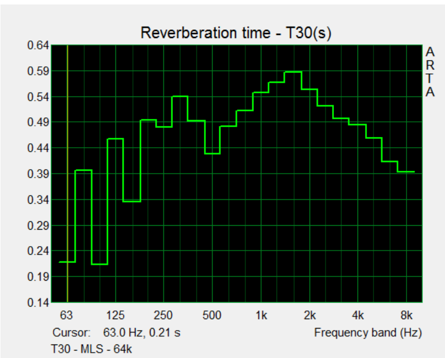

Fig. 23

5.15. MLS – sequence length 262k

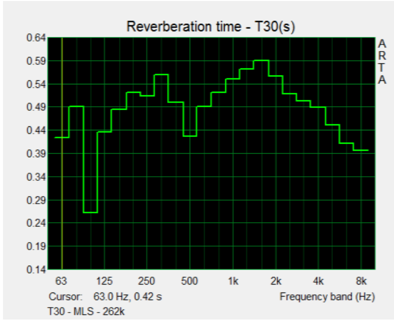

Fig. 24

5.16. Swept-Sine – sequence length 16k

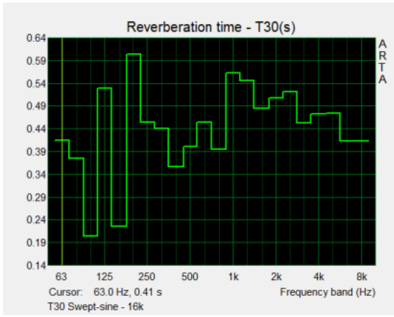

Fig. 25

5.17. Swept-Sine – sequence length 64k

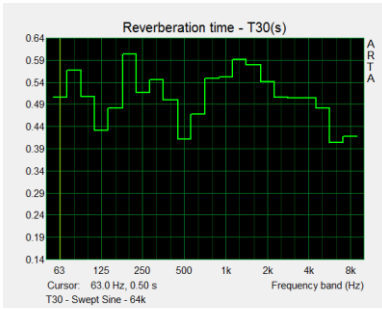

Fig. 26

5.18. Swept-Sine – sequence length 256k

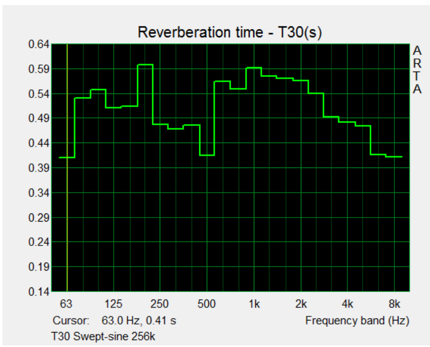

Fig. 27

5.19. T30 comparison - sequence length 16k

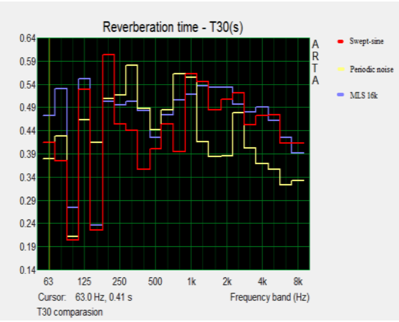

Fig. 28

Analysis

On Fig.19 to Fig.27 are shown test results from T30 extracted from impulse responses. As you can see the T30 from different responses has different shape that's why we plotted all together group by the sequence length. On Fig.28 we see the T30 measured with 16k and it's obvious that the graphs are identical but there are some differences. We can conclude that above 1 kHz the Swept-sine and MLS are similar and the behavior of the curve is due to ray distribution of the high frequency.

Below 1 kHz to around Schroeder frequency we see that MLS and Periodic noise.

It's obvious that the shape of the filter derived from simultaneous masking is expanded compared to this one extracted from forward masking.

Acknowledgment

This paper was supported by Technical University – Sofia inner program to research projects under 161ZF0003-07: "Methods and tools for the study of audio signals".

References

[1] Zwicker E, Fastl H, Psychoacoustics, Springer-Verlag, Berlin, Germany, 1990.

[2] Gelfand, S. A. (2004) Hearing- An Introduction to Psychological and Physiological Acoustics 4th Ed. New York, Marcel Dekker.

[3] Moore, B. C. J. (2004) An Introduction to the Psychology of Hearing, 5th Ed. London, Elsevier Academic PressK. Elissa, "Title of paper if known," unpublished.

[4] Moore, B. C. J. (1986) Frequency Selectivity in Hearing, London, Academic Press.

[5] Moore, B. C. J. (1995) Perceptual Consequences of Cochlear Damage, Oxford, Oxford University Press

[6] Moore, B. C. J. (1998) Cochlear Hearing Loss, London, Whurr Publishers Ltd

[7] Chin-Tuan Tan (2005), Estimates of auditory filter shape using simultaneous and forward notched-noise masking, School of Information Science, Japan

[8] Baker S, Baker RJ. (2006). Auditory filter nonliearity across frequency using simultaneous notched-noise masking. J. Acoust. Soc. Am. 119, 454-462.

[9] Mayer, A. M. 1894. Researches in acoustics. Philosophical Magazine 37, 259-288

[10] Carlos Jurado, David Robledano (2007), Auditory filters at low frequencies: ERB and filter shape, Aalborg University.

METHOD FOR SECURITY ENHANCEMENT OF AUDIO INFORMATION IN COMMUNICATION MULTIMEDIA SYSTEMS AND NETWORKS APPLYING ENCRYPTION ALGORITHM WITH PUBLIC KEY

S. Pleshkova-Bekiarska, D. Kinanev

Department of Telecommunications,
Technical University - Sofia, Kliment Ohridski 8, Sofia

snegpl@tu-sofia.bg

Abstract

In this article it will be analyzed the characteristics of the RSA algorithms for generation of public and private keys used by the cryptosystems in order to ensure the confidentiality, authenticity and integrity of the audio information exchanged between different communication points. For that purpose it will be used the resources provided by the Java JDK 1.8.0_71 programming language with which practically will be shown the advantages and disadvantages of this algorithm.

Keywords: *public, private, key, encryption, java, audio*

1. INTRODUCTION

The security of the information [1] in modern days is extremely important in different aspects, governmental information, business documents, physical security, etc. This is multidisciplinary area of study and professional activities which are concerned with the development and implementation of security mechanisms based on the four principle of the information security: Confidentiality, Integrity, Availability, Non-repudiation.

Confidentiality is the property, that information is not made available or disclosed to unauthorized individuals.

Data integrity means maintaining and assuring the accuracy and completeness of data over its entire life-cycle. This means that data cannot be modified in an unauthorized or undetected manner.

For any information system to serve its purpose, the information must be available when it is needed. This means that the computing systems used to store and process the information, the security controls used to protect it, and the communication channels used to access it must be functioning correctly.

In law, non-repudiation implies one's intention to fulfill their obligations to a contract. It also implies that one party of a transaction cannot deny having received a transaction nor can the other party deny having sent a transaction. It is important to note that while technology such as cryptographic systems can assist in non-repudiation efforts, the concept is at its core a legal concept transcending the realm of technology.

In general the algorithms used for encryption of information are symmetric [2] and asymmetric [3]. Symmetric algorithms are algorithms for cryptography that use the same cryptographic keys for both encryption and decryption. Examples are AES, DES, Blowfish. The main disadvantage of this type of encryption algorithms is the same key is used from the both parties which provides low security of the encrypted information.

In asymmetric algorithms the cryptographic keys are paired and encryption performed with one key, called public, can be decrypted only by the other member, called private key of the pair. Examples are RSA, DSA, Diffie–Hellman. As most common used is the RSA algorithm which unlike the other similar algorithms, it provides all the four key principles of the information security.

Considering the fact that the RSA algorithm is most commonly used, the subject of this article will be developing method to analyze what would be the effect of applying the RSA algorithm in the encryption of audio information and respectively analyzing what would be the resulted key parameters which are important in the implementing such feature in communication multimedia system.

2. BRIEF OVERVIEW OF METHODS OF ENCRYPTION WITH PUBLIC KEY

The RSA algorithm [4] has been invented by Ron Rivest, Adi Shamir, and Leonard Adleman in 1978. It implements a public-key cryptosystem, as well as digital signatures. In RSA, encryption keys are public, while the decryption keys are kept in secret. The RSA algorithm involves four steps: key generation, key distribution, encryption and decryption.

By default the RSA algorithm uses PKCS#1 standard [6] which defines the mathematical definitions and properties that RSA public and private keys must have.

The standard defines several basic primitives. The primitive operations provide the fundamental instructions for turning the raw mathematical formulas into computable algorithms.

- I2OSP, OS2IP: conversion between the potentially large nonnegative integers encountered in the mathematical formulas and their computer data representation as a sequence of bytes (an octet string).
- RSAEP, RSADP: basic encryption and decryption algorithms.
- RSASP1, RSAVP1: algorithms for producing and verifying signatures.

By default in PKCS#1 it is used RSAES-PKCS1-v1_5 scheme for encryption and decryption. RSAES-PKCS1-v1_5 combines RSAEP and RSADP primitives and can operate on messages of length up to k-11 octets (k is the octet length of the RSA modulus), preventing the attacks on low-exponent RSA which is the reason why the block size is kept small. These attacks works when similar messages are encrypted with the same RSA public key. When the block size of information is too large, it is possible to be recovered the key parameters of the private key.

The Digital Signature Algorithm (DSA) is a Federal Information Processing Standard for digital signatures. It was proposed by the National Institute of Standards and Technology (NIST) in August 1991 [5]. Key generation has two phases. The first phase is a choice of algorithm parameters which may be shared between different users of the system, while the second phase computes public and private keys for a single user.

3. DEVELOPMENT OF PRACTICAL ANALYZE METHOD OF RSA ENCRYPTION ALGORITHM APPLIED FOR SECURITY OF AUDIO INFORMATION

The following diagram illustrates the analyze method of the RSA algorithm used for encryption of audio file with .mp3 extension.

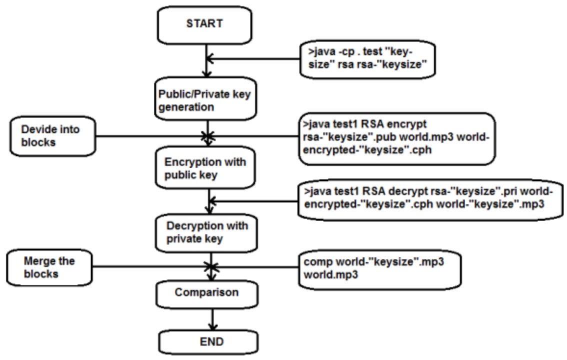

Fig. 1. Workflow diagram

With the command >java -cp . test "key-size" rsa rsa-"keysize" it is triggered the generation of the key pair as it is pointed what to be the key size, what is the used algorithm and what will be the name of the files where the public and the private keys will be stored.

With the command >java test1 RSA encrypt rsa-"keysize".pub world.mp3 world-encrypted-"keysize".cph the program will encrypt file "world.mp3" with RSA algorithm and publik key "rsa-keysize.pub". If the file is longer than 53 bytes then the program will divide the file into blocks, each 53 bytes long, it will encrypt the blocks and then will produces the encrypted file "world-encrypted-keysize.cph".

In order to decrypt the produces file it is used the command >java test1 RSA decrypt rsa-"keysize".pri world-encrypted-"keysize".cph world-"keysize.mp3", where the program is pointed to use "rsa keysize.pri" to decrypt file "world-encrypted-keysize.cph" and produce a result file called "world-keysize.mp3".

At the next step the program will compare whether the original file "world.mp3" matches the produces decrypted file "world-keysize.mp3".

Public/Private key generation

- Choose two distinct prime numbers p and q.

For security purposes, the integers p and q should be chosen at random, and should be similar in magnitude but 'differ in length by a few digits to make factoring harder. Prime integers can be efficiently found using a primality test.

- Compute

$$n = p * q, \quad (1)$$

where n is used as the modulus for both the public and private keys. Its length, usually expressed in bits, is the key length.

- Compute

$$\varphi(n) = \varphi(p)\varphi(q) = (p-1)(q-1) = n-(p+q-1), \quad (2)$$

where φ is Euler's totient function. This value is kept private.

- Choose an integer e such that

$$1 < e < \varphi(n) \text{ and } \gcd(e, \varphi(n)) = 1, \quad (3)$$

where e and φ(n) are coprime.

- Determine d as

$$d \equiv e - 1(\operatorname{mod} \varphi(n)), \quad (4)$$

where d is the modular multiplicative inverse of e (modulo φ(n))

This is more clearly stated as: solve for d given

$$d * e \equiv 1(\operatorname{mod} \varphi(n)), \quad (5)$$

e having a short bit-length and small Hamming weight results in more efficient encryption – most commonly 216 + 1 = 65,537. However, much smaller values of e (such as 3) have been shown to be less secure in some settings.

e is released as the public key exponent.

d is kept as the private key exponent.

The public key consists of the modulus n and the public (or encryption) exponent e. The private key consists of the modulus n and the private (or decryption) exponent d, which must be kept secret. p, q, and φ(n) must also be kept secret because they can be used to calculate d.

Encryption with public key

The following function is used in order to produce the encrypted information:

$$c \equiv m^e \operatorname{mod} n, \quad (6)$$

where c is the resulted encrypted information, e is the public key, m is the messaged.

Decryption with private key. Result file world-"key".mp3

$$c^d \equiv (m^e)^d \equiv m \operatorname{mod} n, \quad (7)$$

where is the exponent of the private key.

Comparison between resulted and original file – At this steps the decrypted file world-"key".mp3 will be compared with the original file.

4. EXPERIMENTAL RESULTS FROM TESTING ENCRYPTION ALGORITHM WITH THE PUBLIC KEY FOR SECURITY OF AUDIO INFORMATION

The tests has been completed on computer with the following parameters:

Processor: Intel(R) Core(TM) i5-4300U CPU @ 1.90 Ghz 2.50Ghz; Installed memory (RAM): 8 GB; System type: 64-bit; Operating System: Windows 7

Java library: JDK 1.8.0_71

Generating of public and private keys.

The question about what should be the key length is very important considering the high security these keys needs to provide.

The main assumption which reflects directly on the choice of key length is the so called factoring of the private key. In general this is the revers process of the key generation in which from the known parameters and known mathematical operations is trying to determine the secret kept parameters involved in the key generation. This method is commonly used from the hackers in order to found out the private key and compromise the information security.

In this test will be generated keys which are 512, 1024, 2048 and 4096 bits long. For that purpose it will be used the predefined functions and classes provided from Java and the source code in the Attachment 1. The public key will be stored in file with X.509 encoded format and name "rsa-size.pub". The private key will be saved in file with PKCS#8 encoded format with name "rsa-size.pri".

Encryption of a test file using the generated public key.

As a start of this test file "test.mp3" with size 3.34 MB will be used. The program returns an error "Data must not be longer than 53 bytes". This is because the RSA algorithm uses PKCS1 padding schema, which can only encrypt 53 bytes at a time (This is the size of one block of data) if your key size is 64 bytes (512 bits). It`s visible that for the different size of the key, this amount changes. For key 1024 bits (128bytes) long, it is 117 bytes, for 2048 bits (256 bytes) it is 245 bytes, for 4096 bits (512 bytes) it is 501 bytes.

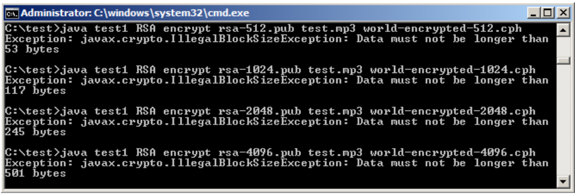

Fig. 2. Encryption of a large test file with the public key

For the purpose of this analyze an audio file called "world.mp3" with size 53 bytes will be used.

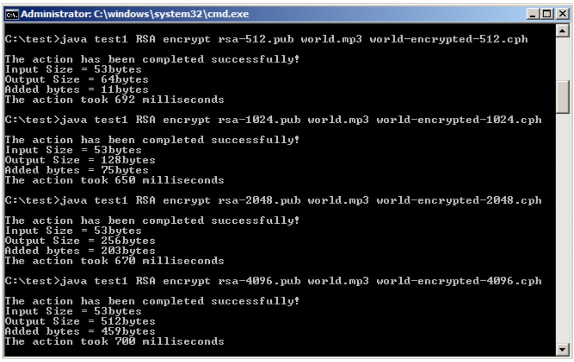

Fig. 3. Encryption of a test file which is 53 bytes long

From the test it could be seen that with 512 bit (64 bytes) key length, the encrypted file is 64 bytes, 1024 bits (128 bytes), it is 128 bytes, 2048 bits (256 bytes), it is 256 bytes, 4096 bits (512 bytes), it is 512 bytes.

Decryption of the test file using the generated private key.

In order the encrypted files to be decrypted, the corresponding private key needs to be used.

The same program will be used for the decryption of the files, but with the following command:

>java test1 RSA decrypt rsa-512.pri world-encrypted-512.cph world-512.mp3

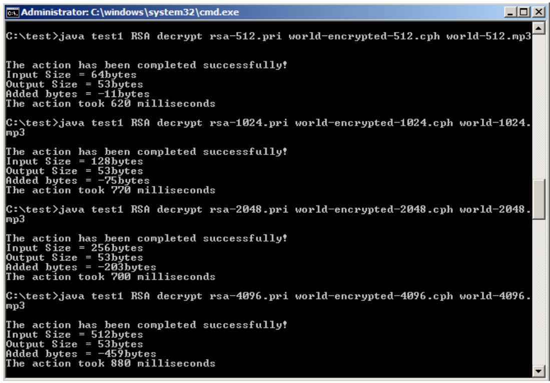

Fig. 4. Decryption of the encrypted file with the private key.

The decrypted files and original file will be compared whether they match:

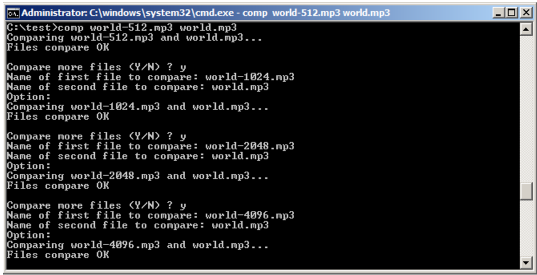

Fig. 5. Comparison between the decrypted and original files

After the check the program returns positive comparison.

5. CONCLUSION

From the tests it could be seen that the RSA algorithm can encrypt only one block information at a time which is 53 bytes long. This is because by default RSA using PKCS#1 padding scheme. So if there is a need to encrypt larger files it should be developed additional feature which will divide the file into 53 bytes long packages because by default the RSA algorithm doesn`t include such a possibility.

From the carried out tests it is visible that by the RSA algorithm when one block information is encrypted, the produced encrypted file is long as the used public key.

For the estimated times of the operations it could be concluded that

$$T_{ENC} = T_c \; , \tag{8}$$

where T_c is the time for which it will be calculated expression (6).

$$T_{DEC} = T_{C^d}, \quad (9)$$

where T_{C^d} is the time for which it will be calculated expression (7).

Usually the time for decryption T_{C^d} is greater than the time for encryption T_c which also can be seen from the measured times.

During the tests the average measured times is 700 milliseconds.

As future development of this analyze method, the test could be carried out on a device which has smaller processor or memory, like mobile device or minicomputer where the time of encryption and decryption could be isolated and more precisely and objectively analyzed.

Also as development of the method, it could be proposed approach to be avoided the RSA limitation of the block size of information which could be encrypted at a time as well as functions in the program code which could divide the larger files into smaller packages.

Acknowlegment

This paper was supported by Technical University – Sofia inner program to research projects under 161ZF0003-07: "Methods and tools for the study of audio signals".

References

[1] "NIST Special Publication 800-27 Rev A". csrc.nist.gov.

[2] Pelzl & Paar (2010). Understanding Cryptography. Berlin: Springer-Verlag. p. 30

[3] Stallings, William (1999-01-01). Cryptography and Network Security: Principles and Practice. Prentice Hall. p. 165. ISBN 9780138690175.

[4] Rivest, R.; Shamir, A.; Adleman, L. (February 1978). "A Method for Obtaining Digital Signatures and Public-Key Cryptosystems". Communications of the ACM 21 (2): 120–126. doi:10.1145/359340.359342.

[5] "FIPS PUB 186]: Digital Signature Standard (DSS), 1994-05-19". csrc.nist.gov.

[6] PKCS#1 v2.2: RSA Cryptography standard, RSA Laboratories, October 27, 2012.

AUTHOR INDEX